DESIGN AND DEVELOPMENT OF MECHANICAL TESTING SYSTEMS FOR

APPLICATIONS IN BONE BIOMECHANICS EVALUATION: BONE DAMAGE REPAIR

AND CLASSIFICATION

A Thesis

by

JIWAN HAN

Submitted to the Graduate and Professional School of
Texas A&M University
in partial fulfillment of the requirements for the degree of

MASTER OF SCIENCE

Chair of Committee,	Michael R. Moreno
Committee Members,	Andrew B. Robbins
	Akhilesh K. Gaharwar
Head of Department,	Guillmero Aguilar

May 2022

Major Subject: Mechanical Engineering

ABSTRACT

Mechanical testing is essential for determining and understanding material characteristics. When engineers develop a product based on their material knowledge, they can analyze the validity and reliability of the final product and, as a result, assure its safety. The mechanical testing methodologies have become vital for a better understanding of biomaterials such as biocompatible metals, ceramics, polymers, and even living cells and tissue due to the emerging importance of mechanical characterization in the biomechanics area. They may be found in machined components, coatings, fibers, and foams used in biomedical equipment and products such as hip joint replacements, bone plates and bolts, and stents. Given the significance of biomechanical testing, the present study will focus on the three distinct aspects of biomechanical testing systems for physically assessing and characterizing biomaterials. To begin, an innovative control system is enhanced to manage complicated motion requirements. The second phase will include the design and construction of a biomechanical push-out test apparatus for evaluating novel medical devices. Finally, a system and process for evaluating bone-to-bone impact damage are being developed.

DEDICATION

     This work is dedicated to my wife, Kijin Seong, and my daughter, Sophie Sunwoo Han. Sunwoo has taught me to appreciate and experience the awe-inspiring nature of life. Sunwoo's birth gave new meaning to every piece of work I contributed. Though she is too young to comprehend what I have devoted my life to, I believe there will come a time when I can tell Sunwoo that the inspiration she provided has motivated me to devote my life to research in order to help those who are in need. Additionally, none of my academic and personal accomplishments over the last several years would have been possible without Kijin's spiritual and material support. Furthermore, Kijin has been the greatest wife and mother, allowing me to live in the moment, which provides me with peace and comfort during this trying time in my life. I am appreciative to her for her unwavering efforts as the best wife and mother in establishing and nurturing a family.

ACKNOWLEDGEMENTS

I'd like to express my heartfelt gratitude to my graduate advisors, Dr. Michael R. Moreno and Dr. Andrew B. Robbins, for their consideration, effort, and time spent helping me in achieving my goals and completing my master's degree program. I recall the day I knocked on the Biomechanical Environments Laboratories' door to start my journey. I was literally alone on this American continent at the time, thousands of miles from home, with no research skills and limited language proficiency. Dr. Moreno and Dr. Robbins' consideration literally changed the course of my life as a researcher, and all the presence I am currently experiencing is a result of their decision.

CONTRIBUTORS AND FUNDING SOURCES

Contributors

This work was supervised by a thesis committee consisting of Professor Michael R. Moreno (chair) of the J. Mike Walker'66 Department of Mechanical Engineering and Dr. Andrew B. Robbins of the Department of Multidisciplinary Engineering, and Dr. Akhilesh K. Gaharwar of the Department of Biomedical Engineering.

The method and fixtures for push-out testing in Chapter III were developed in collaboration with Zachary T. Lawson of the Department of Biomedical Engineering. This achievement was published in Lawson, Z. T., Han, J., Saunders, W. B., Grunlan, M. A., Moreno, M. R., & Robbins, A. B. (2021). Methodology for Performing Biomechanical Push-Out Tests for Evaluating the Osseointegration of Calvarial Defect Repair in Small Animal Models. MethodsX, 101541. and in Pfau, M. R., Beltran, F. O., Woodard, L. N., Dobson, L. K., Gasson, S. B., Robbins, A., Lawson, Z.T., ... & Grunlan, M. A. (2021). Evaluation of a Self-Fitting, Shape Memory Polymer Scaffold in a Rabbit Calvarial Defect Model. Acta Biomaterialia.

The projectile impact testing materials for Chapter IV were provided by Ray Riley of the Department of Animal Science.

All other aspects of the thesis were performed and finished independently by the student.

Funding Sources

NOMENCLATURE

BMEL   Biomechanical Environments Laboratories

BMSC   Bone marrow-derived mesenchymal stem cell

cRIO   Compact Reconfigurable Input/Output Module (cRIO),

DoF   Degrees of Freedom

FIFO   First-in-First-out buffer

K.E.   Kinetic Energy

NI   National Instrument

RTOS   Real-time Operating System

SMP   Shape memory polymer

VI   Virtual Instrument

TABLE OF CONTENTS

LIST OF FIGURES

LIST OF TABLES

CHAPTER I

INTRODUCTION

Biomechanics is a field of study that uses the principles of mechanics to understand the biological systems of humans and animals. In general, biomechanics employs statics, kinematics, dynamics, fluid mechanics, and mechanics of materials to study the characteristics and functions of the biological systems—musculoskeletal, nervous, cardiovascular, digestive, respiratory, and circulatory. Biomechanical studies offer crucial insight into sports performance, orthopedics, medical device development, and surgical treatment optimization.

As for orthopedic biomechanics, it aims to develop orthopedic devices and therapeutic strategies based on the understanding of individual body parts that constitute the musculoskeletal system. Herein, the body parts and biomaterials include hard tissue (e.g., bone), soft tissue (e.g., muscles, ligaments, tendons, and bone marrow), and joints. It is evident from the studies that the mechanical characterization of biomaterial is essential to determine various mechanical properties. Specifically, by applying various degrees of stresses onto biomaterials, we can understand how the materials will react to the applied forces. Eventually, the results can provide guidance when designing and developing products while preserving the expected specifications of materials. Commonly, mechanical testing seeks to obtain information on material properties by employing tensile, impact, hardness, fracture toughness, creep, and fatigue testing. In biomechanics, however, there is a clear differentiation from the conventional mechanical testing area—the body parts of the musculoskeletal system present unique mechanical, biochemical, and biological conditions. For example, the spine experiences four specific loading conditions: axial

compression, rotation, and bending. Considering the wide range of variations in conditions and complex geometric configurations of body parts, it is necessary to thoroughly investigate the mechanical characteristics of body parts by replicating their conditions into experiments. Thus far, it can be seen that a great demand has been laid on designing and developing a custom mechanical testing apparatus to fulfill the needs. However, regarding the research methods, there is a significant limitation to the custom test apparatus developments regarding the absence of testing apparatus standards. Standardization of test methods takes a vital role in guiding experimentalists to prevent innate errors by the falsely designed testing system. To resolve the deficiency and establish standards about mechanical testing apparatus, a comprehensive evaluation and review of developed test apparatus will need to be undertaken.

1.1. Background and Challenge

1.1.1. Background

1.1.1.1. Structure and components of bone

Bone is the hard tissue that makes up and supports the body as a frame. Combined with soft tissue (muscle and ligament) and joints, the musculoskeletal system allows unique and complex mechanisms of four physiological motions, such as bending, rotation, flexion, and extension. In terms of structure, bone comprises compact tissue, cancellous tissue, and subchondral tissue. Compact bone tissue is the hardest tissue in bone structure, covering the outer layer of bones called the cortex. It is a closely packed and solid bone with a few small canals, or osteonic canals, surrounded by lamellae containing bone cells (e.g., osteocytes).

16

Cancellous bone also called spongy bone because of its porous characteristics, consists of interconnected bars and plates called trabeculae with soft tissues, or bone marrow, containing blood vessels. Lastly, subchondral tissue is bone tissue located underneath calcified cartilage in a joint providing firm support. The subchondral bone plays a vital role in producing the locomotion of joints by alleviating forces from joint motions.[1]
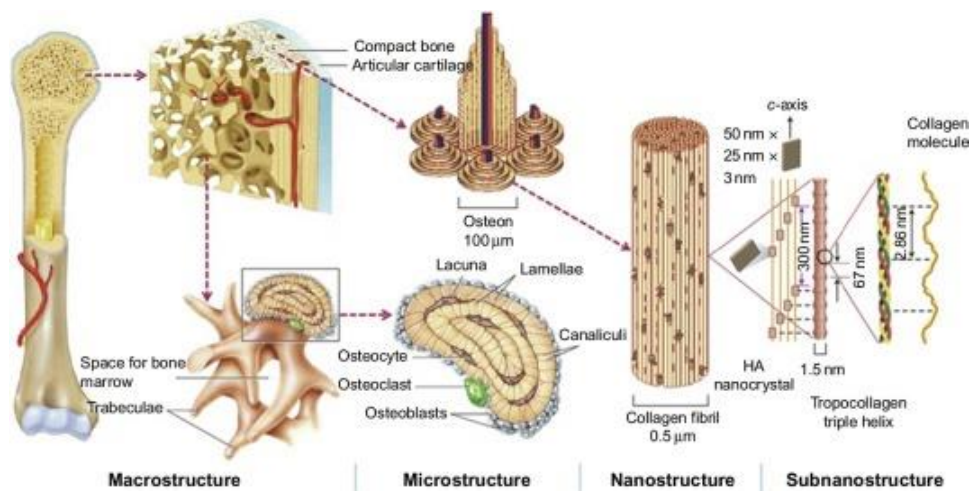
Figure 1. The hierarchical structure of bone from nano to macro scales. [2]

In normal cases, bone injuries, including bone defects and fractures, occur when significant forces are applied to the bone. Also, there is a case of bone fracture by diseases that weaken bones, such as osteoporosis. In understanding these external and internal adverse conditions of bones, it will be essential to explore the causes of injuries and the way of their repairments.

1.1.1.2. *Bone defect and fracture*

In broad terms, the bone defect can be defined as a lack of bone tissue where it should exist. Several factors are known to be associated with bone defect generation. Notable causes of the bone defect occurrence are infection (osteomyelitis), tumor removal, and trauma.[3] In the case of bone fracture, it is well known that fatigue, health conditions affecting bone density (e.g., osteoporosis), and physical trauma cause broken bones. The causes of these bone disorders can be classified into congenital and acquired diseases. Moreover, a person's age negatively impacts bone density, increasing the risk of bone breaks.

1.1.1.3. *Repairment of bone damage*

Regenerative methods (e.g., use of autologous or allogeneic graft) are the main options used to promote osteogenesis in the region of bone loss and repair the bone defect. Bone autograft differs from the allograft method in terms of safety by utilizing a patient's tissue. Otherwise, allografting risks disease transmission from a donor and requires a longer rehabilitation timeline to incorporate the tissue into the patient's body. Though there are advantages and disadvantages to using either autograft or allograft bone tissues, it has been proved that both are exceedingly safe.[4] Concerning regenerative treatments, some limitations need to be acknowledged. The treatments are limited by donor site morbidity, graft degradation after surgery, bone site availability, and difficulties processing harvested bone tissues. Nonetheless, tissue engineering offers insight into developing alternatives to treat bone defects, with novel scaffolds having several noteworthy specifications, such as being self-fitting,

bioactive, and biodegradable.[5] Future studies on the mechanical characterization are therefore required to confirm and validate the novel medical devices and secure their efficacy.

In the case of bone fracture repair, three primary treatment options are widely accepted: casting, internal fixation, and external fixation of broken bones. Both internal and external fixation are associated with surgery to repair the fracture.

Figure 2. Internal fixation for fractures[6]
(a) wires, (b) plates, (c) rods, (d) screws, (e) pins
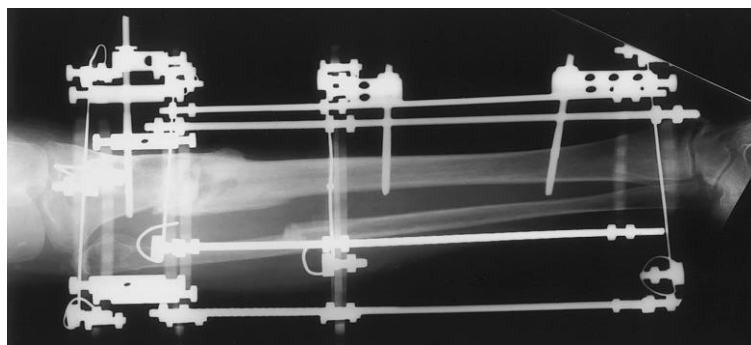
Figure 3. External fixation for fractures[6]

In terms of materials, biocompatible metals (e.g., titanium and cobalt-chromium alloy), ceramics (e.g., alumina and bioglass), and polymers are used to design and develop orthopedic devices (e.g., rods, screws, or plates). The frames are frequently used to support and hold the fractured bones in the correct position. With the load distributions and fixation, blood clot and bone tissue, or callus, are formed around the broken bones to heal injuries.[7] To better understand how the skeletal system works under unique conditions, there have been demands for the mechanical characterization of materials. One reason material characterization has important implications is that it allows engineers to quantify whether a particular material is suitable for a specific application and to ensure the reliability of the production process.

1.1.2. Research background and challenges of projects

The objective of this thesis proposal is to investigate bone biomechanics in terms of bone defect repair and bone fracture analysis by covering two distinct projects. Firstly, a project regarding cranial bone defect repair device evaluation was conducted by developing and using a custom push-out test apparatus. Secondly, bone fracture patterns formed from an impact on a skeletal bone target will be analyzed to study and understand the bone tissue fracture biomechanics.

1.1.2.1. Project 1: Evaluation of calvarial bone defect repair device

1.1.2.1.1. Background of research

It has been known that confined cranial defects result from trauma, congenital deformities, craniotomy, and tumor removal.[8] Cranioplasty is the most common surgical repair

of cranial bone defects. There are various options of cranioplasties, such as cultured bone autografts from one part of the patient's body, decellularized bone allografts, or custom contoured graft made from biocompatible materials (e.g., titanium, natural polymers, gelatin methacryloyl (GelMA), collagen, polyethylene glycol (PEG), and bone cement). In general, cancellous bone autografts harvested from the patient's iliac crest are considered the gold standard for healing cranial bone defects.[9] However, the limitation is laid on contouring and shaping the rigid harvested bones to induce osseointegration and osteogenesis between the applied autografts and adjacent bone tissues. To promote effective cranial bone healing, there have been needs for self-fitting devices shaping themselves into the defects' irregular geometry. To meet this demand, Dr. Melissa Grunlan and her research team have developed and reported an innovative, self-fitting Shape Memory Polymer (SMP) scaffold promoting cranial bone defect healing.[10] The SMP can self-fit into the arbitrarily shaped defects and is biodegradable, bioactive, and osteoinductive.

Figure 4. Implanting "self-fitting" SMP scaffolds[11]

<u>1.1.2.1.2.</u> <u>Challenge</u>

Concerning performing push-out mechanical testing for the small animal model, many researchers face the following challenges: 1) clamping a tiny calvarial bone with bilateral defects, 2) mitigating bending moment while clamping samples, 3) precise alignment between the push-out apparatus and the region of interest, 4) securing the experimenter's sight on the clamped sample and push-out rod in action, and 5) prompt sample fixation to reduce dehydration.

<u>1.1.2.2.</u> Project 2: Biomechanical evaluation of osseous projectile impacts on skeletal bone

<u>1.1.2.2.1.</u> <u>Research background</u>

A single male mastodon (Mammut americanum) was excavated at the Manis site in Washington in 1977 by the Washington State University research group. The rib bone was analyzed using radiocarbon dating, and was dated back to about 13,800 years ago; however, the first human presence is theorized to have begun in North America only 13,000 years ago. Furthermore, computed tomography (CT) images revealed that a foreign osseous object was embedded in the rib and shaped artificially to a point.[12] The foreign object penetrated 2.15 cm into the rib, and its tip broke after entering the approximately 2 mm thick cortical bone of the rib. To add, evidence of bone regeneration was not found around the point, indicating that the mastodon died soon after the projectile's impact.
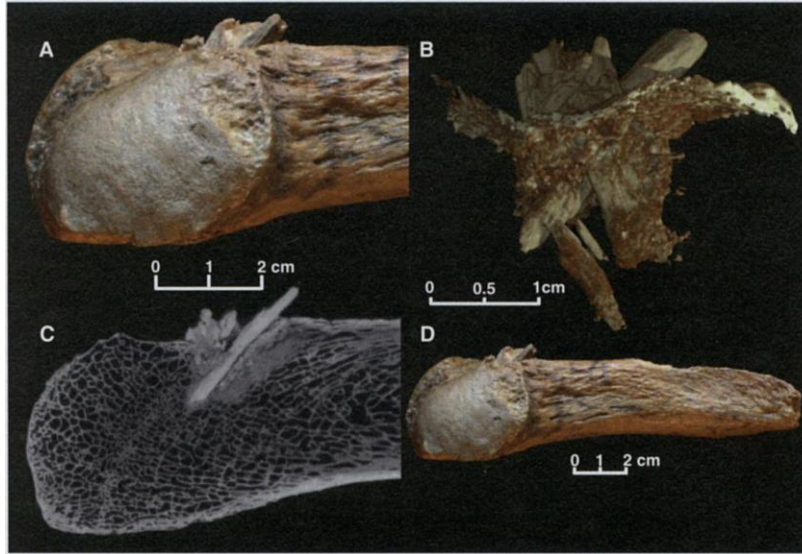
Figure 5. Mastodon rib with the embedded bone projectile point[12]

1.1.2.2.2. Challenge

Without direct evidence of hominins using osseous projectiles for hunting mastodon in pre-Clovis times, there are difficulties in figuring out the appearance of projectiles in the archaeological records. Also, a standardized, widely accepted experimental method has not been presented to validate the assumption that osseous projectiles accelerated to human throwing velocities replicate the fracture patterns observed in the Manis Mastodon rib model. Until this research, the gold standard method to perform osseous projectile impact tests on skeletal bone targets has involved humans pitching irregularly accelerated spears or darts to randomly fixed targets. Solving the uncertainty and proving the assumptions requires standardized testing methods development to ensure safe and reliable results acquisition, with well-controlled testing conditions reducing errors.

1.2. Specific Aims

1.2.1. Specific Aim 1: Extend the capabilities of the existing motion controller of the existing

mechanical testing system to meet user needs better.

The existing control system software architecture will be improved to extend the capabilities of processing user input motion parameters. This will enable the system to handle user-defined motion input parameters having a larger number of motion sets than the size of the motion parameters storing array and the first-in-first-out (FIFO) buffer. A function generator will then be created to generate quadratic motion profiles to connect user-defined parameters employing spline interpolation. This will secure user convenience for producing smooth curves based on user input parameters with less computational effort.

1.2.1.1. Extension of the processing capability of motion input parameter

A system software architecture will be designed and developed to process an arbitrarily large number of motion input parameters loaded from user-defined motion set points regardless of the finite capacity of the system array size and the FIFO buffer size.

This portion of Specific Aim 1 will be considered complete when a new motion profile generator for the RTS system is not limited by a finite array size for processing motions and can have an arbitrarily large number of motions utilized in a motion profile, to be demonstrated by performing several motions that are larger than the size of the current FIFO buffer.

1.2.1.2. Development of a spline motion profile generator

A motion profile generator will be developed to generate setpoints based on quadratic equations. This function will connect two consecutive user set points with smooth interpolated curves, ensuring numerical stability and reasonably high accuracy with comparatively less computational effort. This will also provide convenience for users desiring motion profile curve fittings based on a few user input parameters.

This portion of Specific Aim 1 will be considered met when the new motion profile generator will be capable of performing spline motions, as demonstrated by performing a spline-controlled motion profile.

1.2.1.3. Development of User Interface VI

The existing user interface will be improved and extended in accordance with the new motion profile generator and system software architecture. This will be capable of storing and metering user input parameters and assigning demanding motions to the FIFO buffer until the whole set of input motions is finished.

This portion of Specific Aim 1 will be considered complete when the new function generator illustrates an example user interface capable of metering and assigning motions to the FIFO buffer.

1.2.2. Specific Aim 2: Develop a test apparatus for performing push-out tests on rodent bilateral calvarial defect repairs.

Push-out testing system design needs and limitations will be identified from existing research to meet the experimental requirements. A novel test apparatus will then be designed and built to perform push-out testing on rodent bilateral calvarial defect repairs. The test results will be evaluated to compare the novel therapeutic treatment to a gold standard treatment.

This aim will be considered complete when a push-out test apparatus is developed and successfully employed to compare a novel therapy to a gold standard treatment.

1.2.3. Specific Aim 3: Evaluate the biomechanics of osseous projectile impacts on skeletal bone.

A test apparatus will protect the experimenter from bone-on-bone impact testing, and the dispersed fragments will be designed and developed. This equipment will ensure the experimenter gets a clear vision of a flying projectile and its target. Impact tests will then be executed, employing the developed apparatus to reproduce the osseous projectile on the osseous target.

1.2.3.1. Extend the existing projectile apparatus to enable safe testing of bone-on-bone impact at human throwing velocities while preserving the visibility of the projectile and impact site.

This will be considered complete when an apparatus has been built and tested to 1) hold specimens (both osseous and osseous in tissue simulant) in place at a 45-degree angle and 2) safely contain the products of bone-on-bone impact and protect the operator from fragments.

1.2.3.2. Replicate the dynamics of bone-on-bone projectile impact from a human-accelerated

projectile and compare the results to the Manis mastodon specimen.

This aim will be considered complete when at least nine specimens have been tested at various combinations of kinetic energy and momentum, and the failure patterns are compared to those of the Manis mastodon.

CHAPTER II

MOTION CONTROLLER IMPROVEMENT OF PRE-EXISTING MECHANICAL TESTING

SYSTEM TO BETTER FULFIL USER DEMANDS

2.1. Introduction

Universal Testing Machines (UTMs), also known as materials testing machines or materials test frames, have been used to conduct mechanical tests (e.g., tension, compression, or bending) on materials since the 1800s. [13] Mechanical testing can be performed to identify the properties of a material independent of its geometry or when specific geometrical criteria are employed. With the advent of biomechanical engineering, there has been an increased requirement to determine characteristics of biomaterials such as biocompatible polymers and tissue. This is because material characterization lays the groundwork for understanding the material's mechanical properties and the possibility of adverse mechanical effects during operation. Comprehensive material characterization of biomaterials can offer sufficient information to establish a mechanical property assessment. Additionally, it aids in material consistency across a range of engineering applications.[14]

Precise testing and data collection from applied samples have been enabled by the development and deployment of microcontrollers for active control of mechanical testing devices. Universal testing machine manufacturers, such as INSTRON and MTS, have built their own framework and control software that is designed for the system. It is often considered that the manufacturers' systems are robust and reliable. However, the difficulty is that it is not cost-efficient when it comes to meeting the requirements of soft, hard, and connective tissue testing conditions. Tissues (e.g., bone, muscle, ligament, and joint) are exposed to a unique environment

based on their function. For example, the cervical vertebrae have an estimated range of motion of 80° to 90° of flexion, 70° of extension, 20° to 45° of lateral flexion, and up to 90° of rotation to both sides.[15]
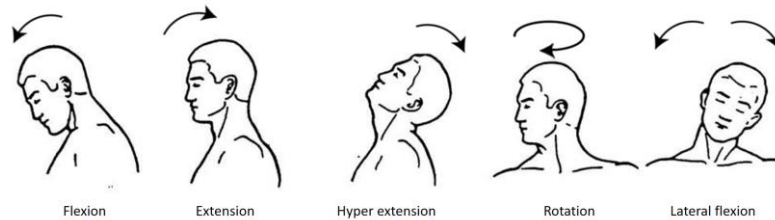
Figure 6 - The graphic illustrates the cervical vertebra's conceivable movements: flexion-extension, hyperextension, axial rotation, and lateral flexion [16]

To reproduce the unique environment and perform tests on complicated body components (e.g., cervical vertebrae), either expensive specialized accessories provided by the testing machine manufacturer or the construction of custom testing equipment compatible with and limited to commercial frames is required. As a result of these considerations, a Biomechanical Environments Laboratories (BMEL) alumnus created the Reconfigurable Testing System (RTS). This testing machine can adapt to changing test settings by reconfiguring its frames to match the tissue's specific functional features. Along with the framework, a control system and user interface were developed using National Instruments' (NI) LabView to operate a system comprised of a Compact Reconfigurable Input/Output Module (cRIO), a linear actuator, and an LVDT. Given the information provided about the creation of the RTS, this thesis will

investigate the control system's structure and will evaluate and improve the system's software architecture.

Figure 7 - The RTS in uniaxial mode with a linear actuator attached to the framework

2.2. Original RTS machine's system architecture and limitations

2.2.1. General summary of the RTS's framework and control system

To recap the physical configuration of the RTS, aluminum extrusion frames custom ordered from '80/20 Inc.' are utilized to create the framework for the Reconfigurable Testing

System (RTS). A linear actuator (ECT09-B53S03PB-2510) is installed on the constructed structure and is driven by a Kollmorgen AKD-PO1206-NBEC-0000 servo motor driver.

Figure 8- ECT09-B53 Linear Actuator

Figure 9 - Kollmorgen AKD-PO1206-NBEC-0000 servo motor driver

With regards to the physical equipment, another distinguishing feature of RTS is its use of National Instruments' (NI) Compact Reconfigurable Input/Output Module (cRIO) and

LabVIEW to control the linear actuator. The cRIO system combines a real-time professor, reconfigurable FPGA, Ethernet expansion chassis, and modular National Instruments C Series I/O to provide industrial-grade high-performance control and monitoring through sensors and conditioned Input/Output modules. To complement the performance of the cRIO hardware, LabVIEW software developed by NI allows developers to program both the processor and user-programmable FPGA using a single, easy graphical software platform that can be enhanced and extended as user requirements evolve.

Figure 10 - cRIO 9064 having four-slot chassis, reprinted from National Instruments

2.2.2. System Architecture of Existing RTS machine

A Biomechanical Environments Laboratories (BMEL) alumnus, Aaron C. Stone, originally developed the programed control system code using LabView 2016. The control system code is composed of multiple layers that interact with one another through data packages that include generated and obtained data such as motion input parameters, desired setpoints, and sensor readouts.
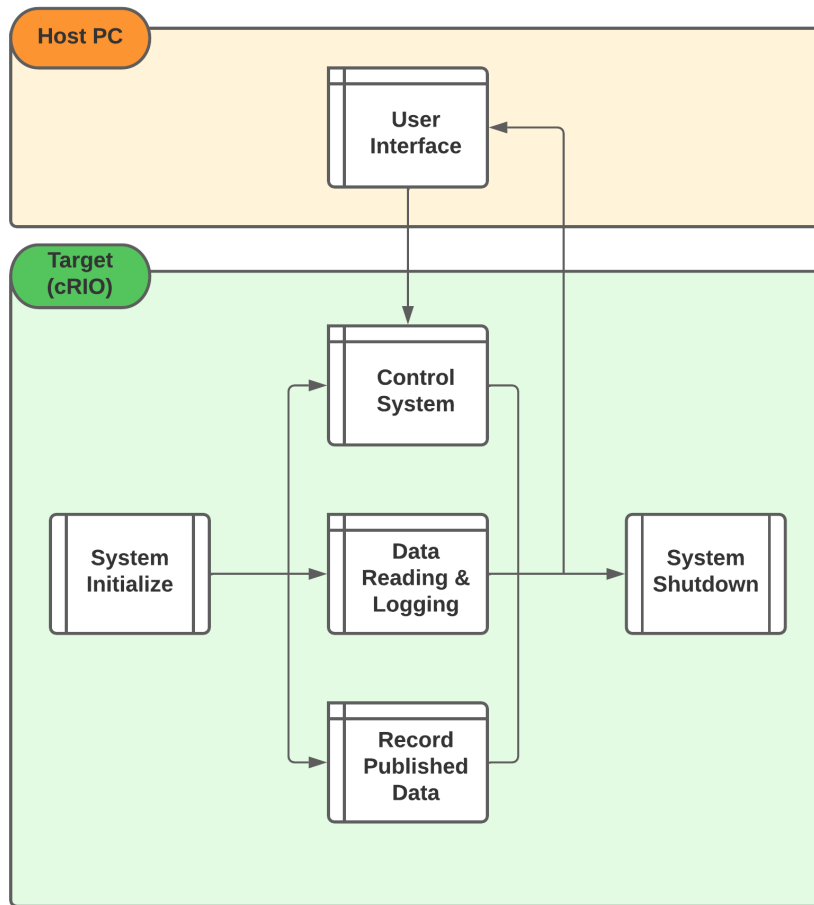
Figure 11 - RTS System Architecture at a Glance

As seen in the figure above, two groups of interfaces are developed. They operate on distinct platforms, called 'Host PC' and 'cRIO.' Specifically, 'User Interface' runs on the 'Host PC' to display system status, input parameter information, and position and load sensor readouts.
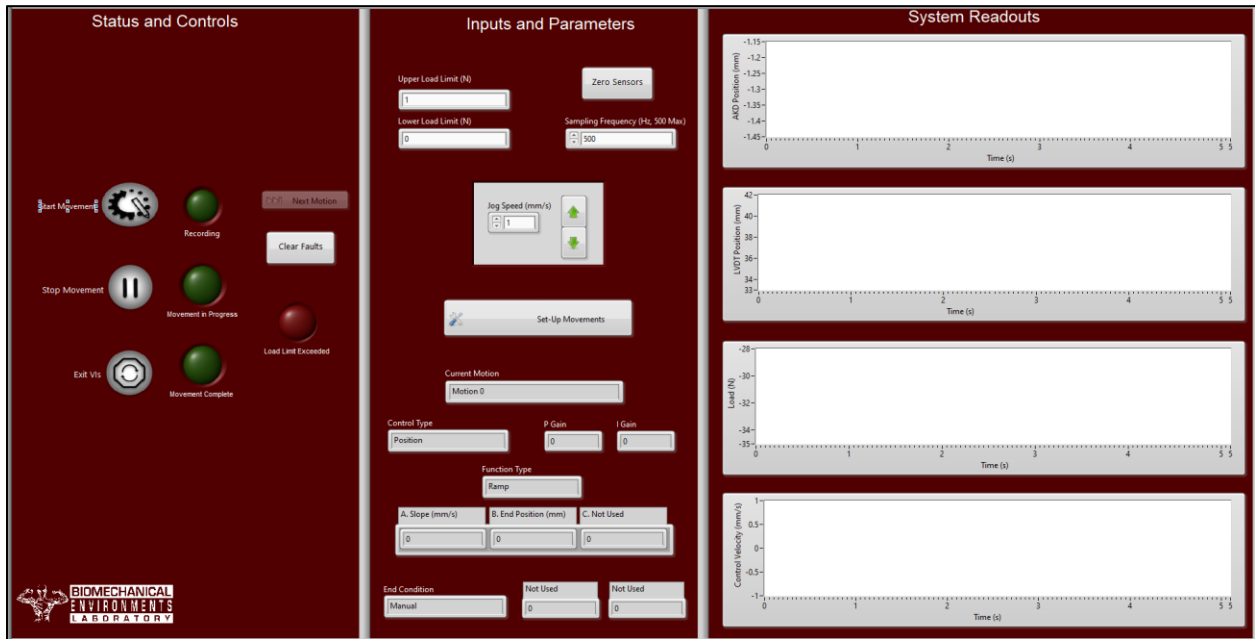
Figure 12 – RTS 'User Interface' front panel; system status (left column), parameters information (middle column), and sensor readouts (right column)

The motion parameters input panel in the 'Set Movement' VI enables users to provide the 'State machine' VI parameters in the cRIO control system loop. The transmitted inputs will be used by the 'Function Generator' integrated into the 'State machine VI' to identify the next desired position or load set point based on the current position or load readouts. The position or load setpoint is utilized to calculate the velocity set point using the 'PI controller' VI, then passed to the linear actuator's AKD motor driver for control.
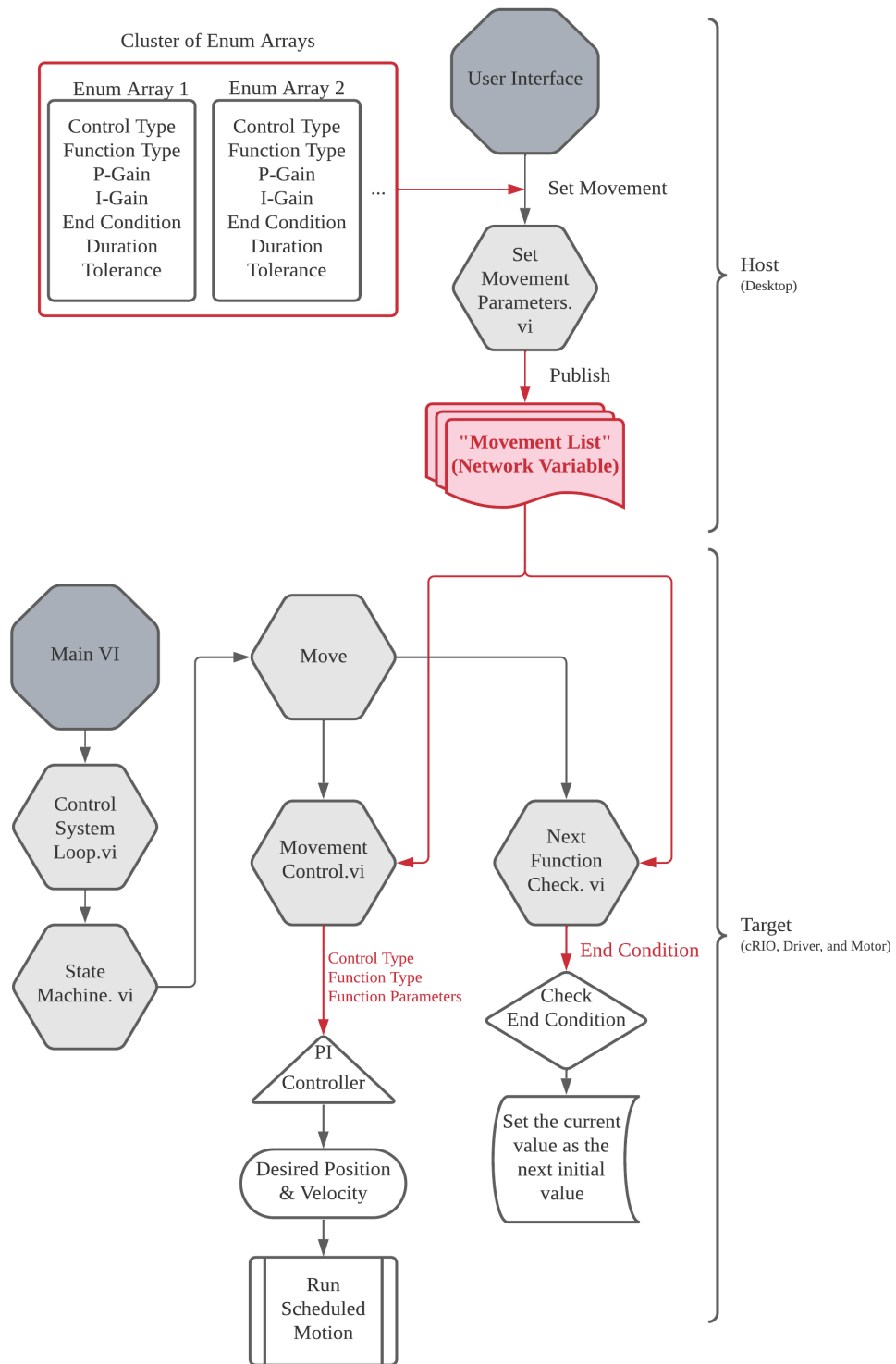
Figure 13 - System architecture in terms of motion input array pathway

A distinguishing feature of the original 'Set Movement' VI is the organization of eleven clustered user motion input parameters, which include 1) Control type, 2) Function type, 3) Parameter A, 4) Parameter B, 5) Parameter C, 6) Parameter D (values specified by the function type), 7) P-gain, 8) I-gain, 9) End Condition, 10) Duration, and 11) Tolerance. Each line in the array comprises a clustered collection of parameter values. Suppose the motion to which the parameters belong is not identified. In that case, it is possible for parameters to get mixed up and erroneous inputs to be provided when they are not needed. To avoid this issue, it is beneficial to arrange parameters into clusters and stack them into an array in order to deal with specific information at a particular moment. The advantage of combining clusters of input parameters into an array is that it simplifies consumer-side, or cRIO, operation.
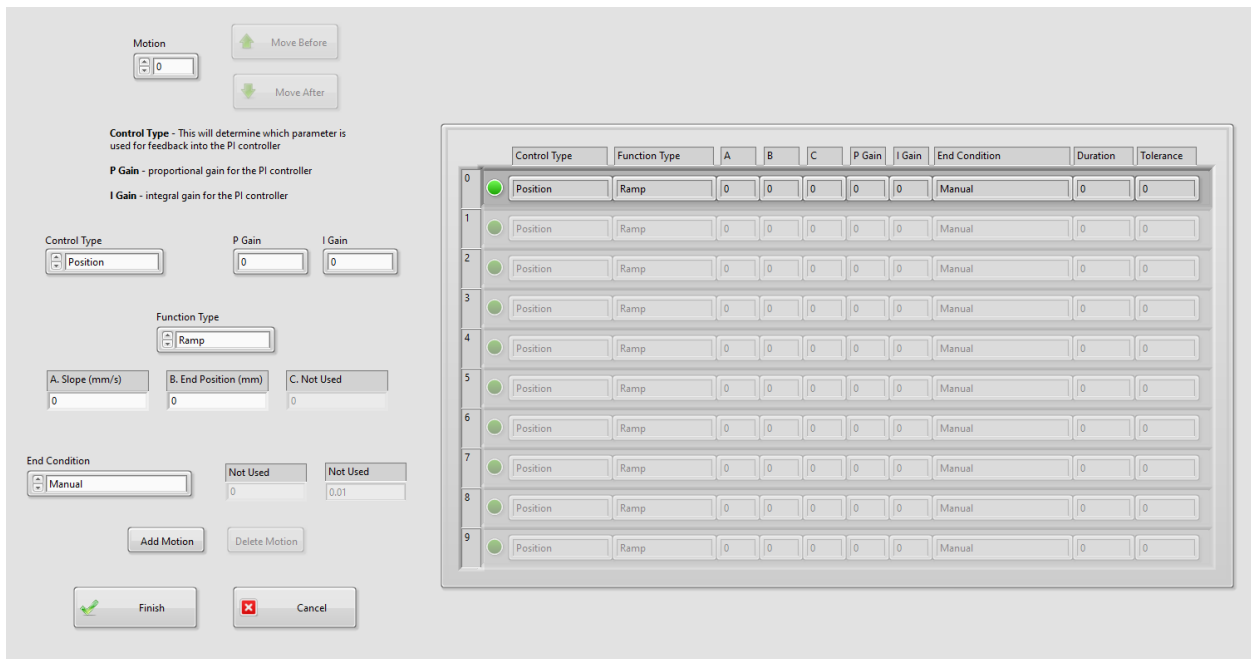
Figure 14 - 'Set Movement' VI front panel allowing users to specify movement parameters

	Control Type	Function Type	A	B	C	P Gain	I Gain	End Condition	Duration	Tolerance
0	Position	Ramp	0	0	0	0	0	Manual	0	0
1	Position	Ramp	0	0	0	0	0	Manual	0	0
2	Position	Ramp	0	0	0	0	0	Manual	0	0
3	Position	Ramp	0	0	0	0	0	Manual	0	0
4	Position	Ramp	0	0	0	0	0	Manual	0	0
5	Position	Ramp	0	0	0	0	0	Manual	0	0
6	Position	Ramp	0	0	0	0	0	Manual	0	0
7	Position	Ramp	0	0	0	0	0	Manual	0	0
8	Position	Ramp	0	0	0	0	0	Manual	0	0
9	Position	Ramp	0	0	0	0	0	Manual	0	0

Figure 15 - Array of eleven clustered motion input parameters (original RTS)

2.2.3. Limitation of the Current Architecture

Among the strengths and distinguishing characteristics, the precision testing machine's performance restrictions must be maintained. To begin, restricting the array size for storing motion input parameters at the 'Set movement parameter' VI in the 'User interface' to ten inhibits users from generating complicated motions within the time allotted. Second, limiting function types to the ramp, sinusoidal, and creep forces users to create only rudimentary motion profiles. Finally, without respect for the critical time constraints associated with processing data deemed to meet Real-time Operating System (RTOS) qualification, the desired set points are determined by accumulating residual errors.[17]

2.3. System Improvement Strategy and Method

2.3.1. Enhancements to the process of storing and transferring motion input parameters

On the 'User interface' side, the restricted number of arrays available to receive and store motion input parameters has posed a substantial barrier to users designing complex movements for advanced mechanical testing. For example, to conduct fatigue and wear tests on specimens, a machine must be capable of scheduling repeated movements for an extended period of time. While the sinusoidal function of the current system was created with this capacity in mind, it is evident that the sinusoidal waveform is insufficient due to its inability to manipulate displacement or loading rates.
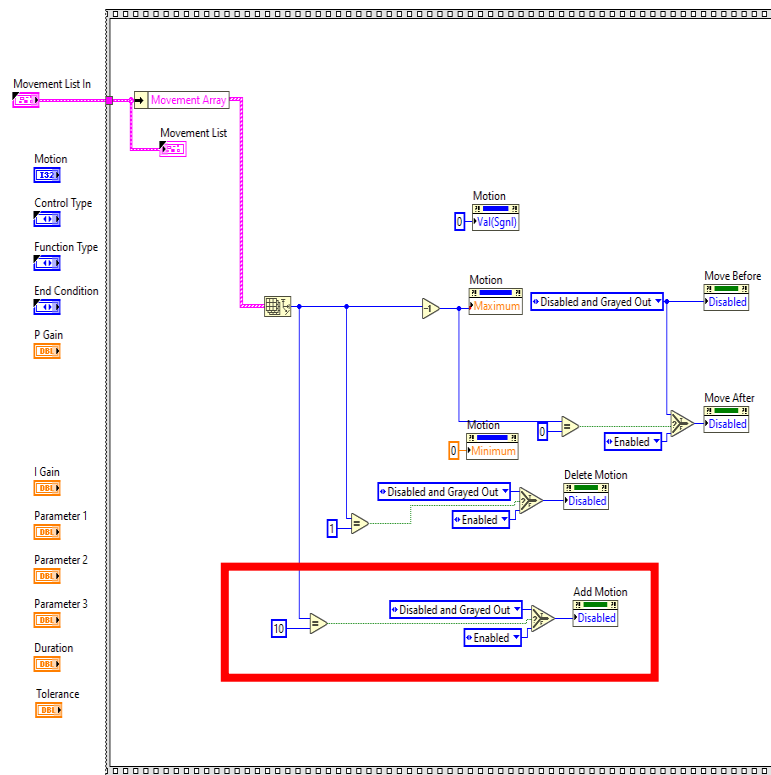
Figure 16 - Array size boundary condition in 'Set movement parameter' VI of 'User interface'

As seen in Figure 16, a boundary condition limiting the size of the array was set to ten (10) and is deleted to increase the array capacity storing the motion input parameters. By eliminating the requirement, the system is able to hold an 'infinite' number of movements, with the array being automatically filled based on the user's requested number of motions. However, an issue has arisen with the uncertainty of the overall number of motions. Since the 'Set movement' VI's array has a maximum size of 10 sets of parameters, there was no need to consider limiting the quantity of data delivered to the target (cRIO) with restricted memory resources. Due to the absence of array size boundary restrictions after the code modification, it is necessary to publish movements from the Host PC to the target one motion at a time to reduce the memory burden on the target (cRIO). A special kind of buffer called a 'First-in-First-out (FIFO)' is used to address this problem. The FIFO is a data buffer processing technique that prioritizes the oldest (first) item, or "head" of the queue, for processing, as seen in figure 17.[18]
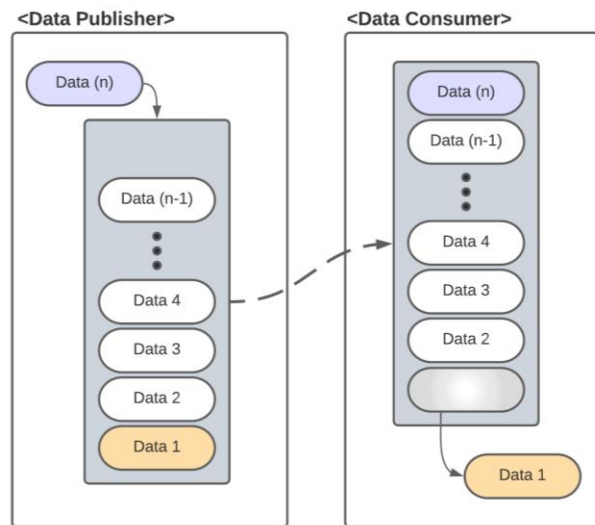
Figure 17 - First-in-First-out (FIFO) buffer data flow

Using this buffer functionality, the original network published shared variable is replaced with a FIFO activated network published shared variable. A new VI named 'Publish Movements to FIFO' is developed to transmit motions to the target through the buffer, as seen in Figure 18.
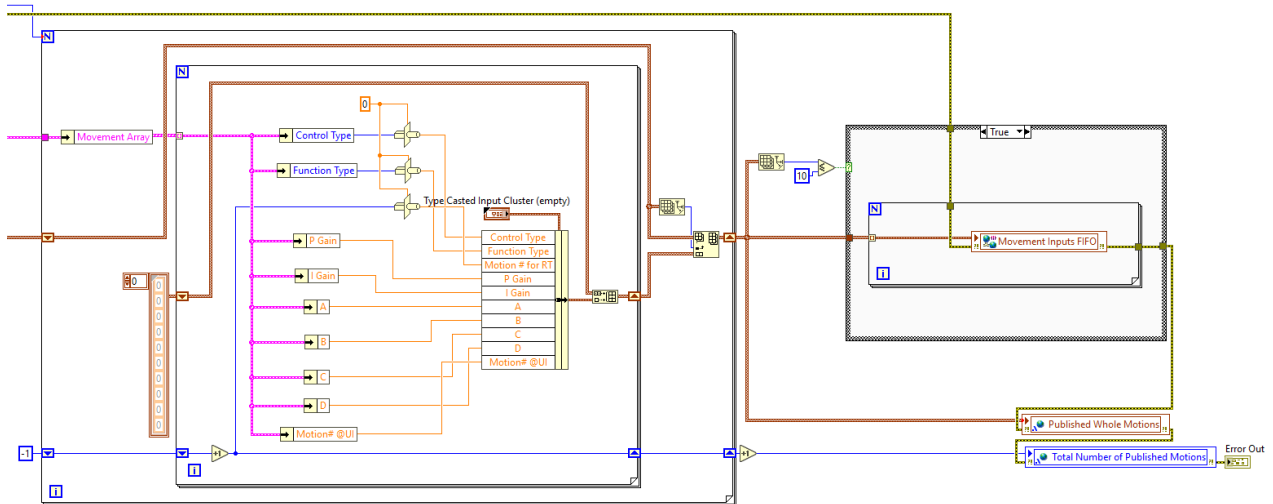
Figure 18 - 'Publish Motions to FIFO' VI

Thus, by removing constraints on the number of publishable movement parameters and introducing a FIFO buffer, the system can now respond to user demands for complicated motion planning to execute previously unachievable mechanical testing, such as fatigue and wear tests.

The RTS's initial function generator was developed to generate desired values using an NI LabView feature called 'Formula Node,' allowing users to construct functional nodes using C-syntax structured programming language. The 'Formula Node' has the advantage of allowing the user to execute complex mathematical operations on an intuitive block diagram, which is especially useful for equations with many variables.[19]

To underscore the original control system's weakness, the RTS has inherent potential errors that can jeopardize the mechanical testing system's reliability: (1) Separation of system stopping logic from the function generator, (2) Lack of processing time restrictions. The mechanical testing system necessitates a precise motion control system that maintains a precisely specified time limitation that is wholly understood and constrained rather than just retained within a given time range within tolerance. All motion set points generation processes must adhere to specific guidelines. "Real-time Operating System (RTOS)," which is an essential feature that high-end precision control systems should have, is the operating system that meets these kinds of requirements. A new function generator processing motion data with severely defined time limits for the entire published motions are considered while upgrading RTS.

As seen in figures 20, 21, and 22, the original function generator uses the 'Initial Value; IV (position or load readout),' 'Function parameters,' and 't (duration of currently running motion)' to generate the 'Desired Value; Val' as an outcome. The problem is that the time the original function generator operates on is the duration of the 'Currently running motion,' not the time defined in the user interface. Specifically, the time is not a variable that the user can utilize

as a constraint to force the function generator to cease when the motion reaches the user-specified time. This is a concern because if the user-defined end condition (for example, stopping the actuator when it reaches a particular range of tolerance) is not fulfilled within the expected end time, the function generator will continuously create the desired value, causing the actuator to travel indefinitely.
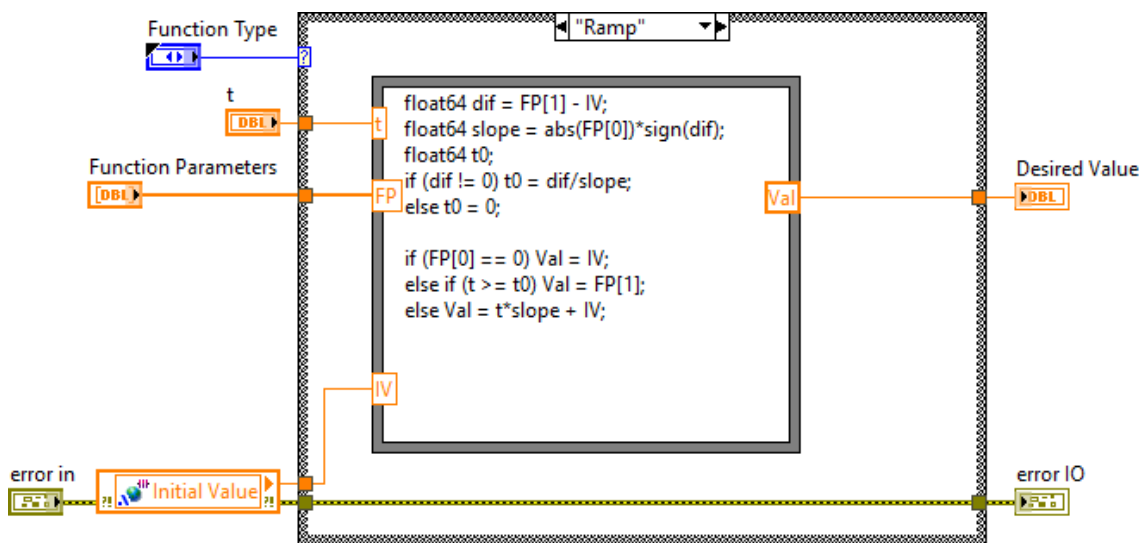
Figure 19 - Original function generator of RTS ('Ramp function' mode)
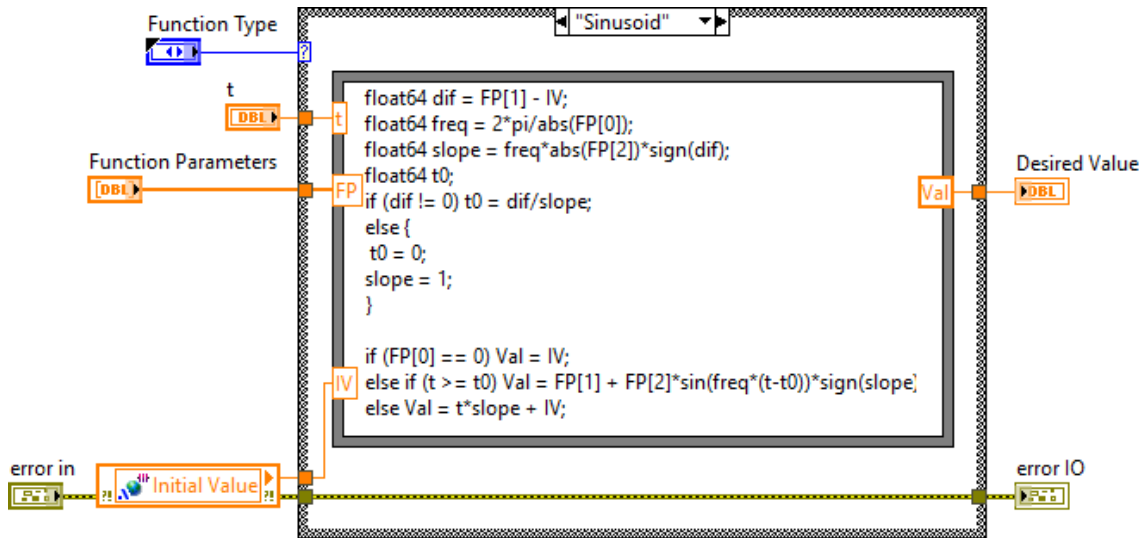
Figure 20 - Original function generator of RTS ('Sinusoidal waveform' mode)
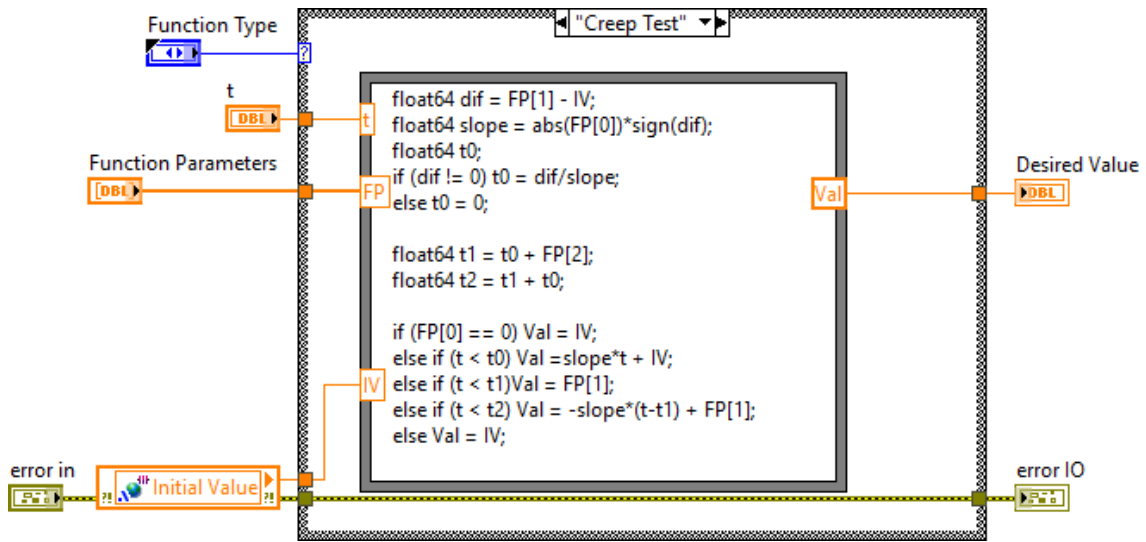
Figure 21 - Original function generator of RTS ('Creep test' mode)

For instance, in Figure 19, the 'Formula Node' with 'Ramp' function employs the following equation at the end line of the programed code to acquire the next set point.

$$Val = t * slope + IV$$

The thing is that the variable 't' is defined by calculation out of the function generator:

$$t = ' \text{current time}' - '\text{starting time of current motion}'$$

In the equation, the 'starting time of current motion' is reset to 'current time' to make $t = 0$ when there is a switch to the subsequent motion. To decide when to reset the 'starting time of current motion' to 'current time,' the original RTS control system employs a separate VI named 'End Conditions.'

For more information, the VI was developed to prevent the function generator from delivering the next set point to the PI controller if certain end conditions are met. And the following conditions are proposed to users to select in the user interface: (1) Manual mode (Go to the next motion if the user manually presses the "Next Motion" button in the user interface), (2) Reached Final Value mode (Go to the next motion if the measured value is within user input "Tolerance"), and (3) Time After Final Value (Go to the next motion if user input "Duration" seconds have passed since the measured value was within user input "Tolerance").
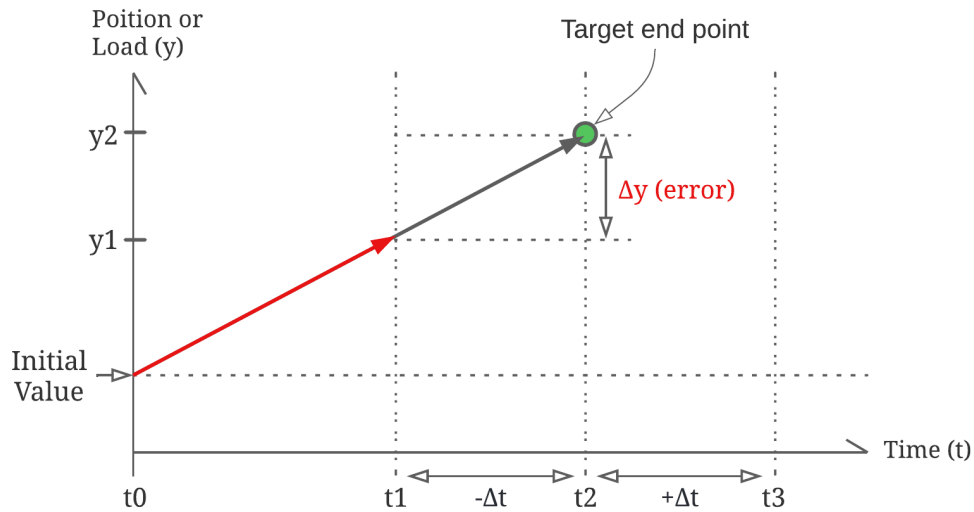
Figure 22 - Time vs. Position or Load graph

Given the stated conditions, the 'End Condition' VI provides accuracy issues with the testing equipment. For instance, when the 'End condition (2) - Reached Final Value' is used, the system determines whether to halt the currently running motion when the measured value obtained from the sensor readout approaches the end point ($y_1 < y < y_2$) within the user-specified tolerance (Δy), as illustrated in Figure 22. Due to the tolerance, the system may terminate the function generator and go to the next motion earlier ($t = t_1$) than the time required to complete the ramp function ($t = t_2$). It finally results in the actuator being halted at y_1 rather than y_2, keeping the actuator's position or load error (Δy). While the time and targeted value errors ($\Delta t \ and \ \Delta y$) seem small, they become substantial when accumulated across a large number of moves and a long period of time, such as 500 movements over 48 hours.

46
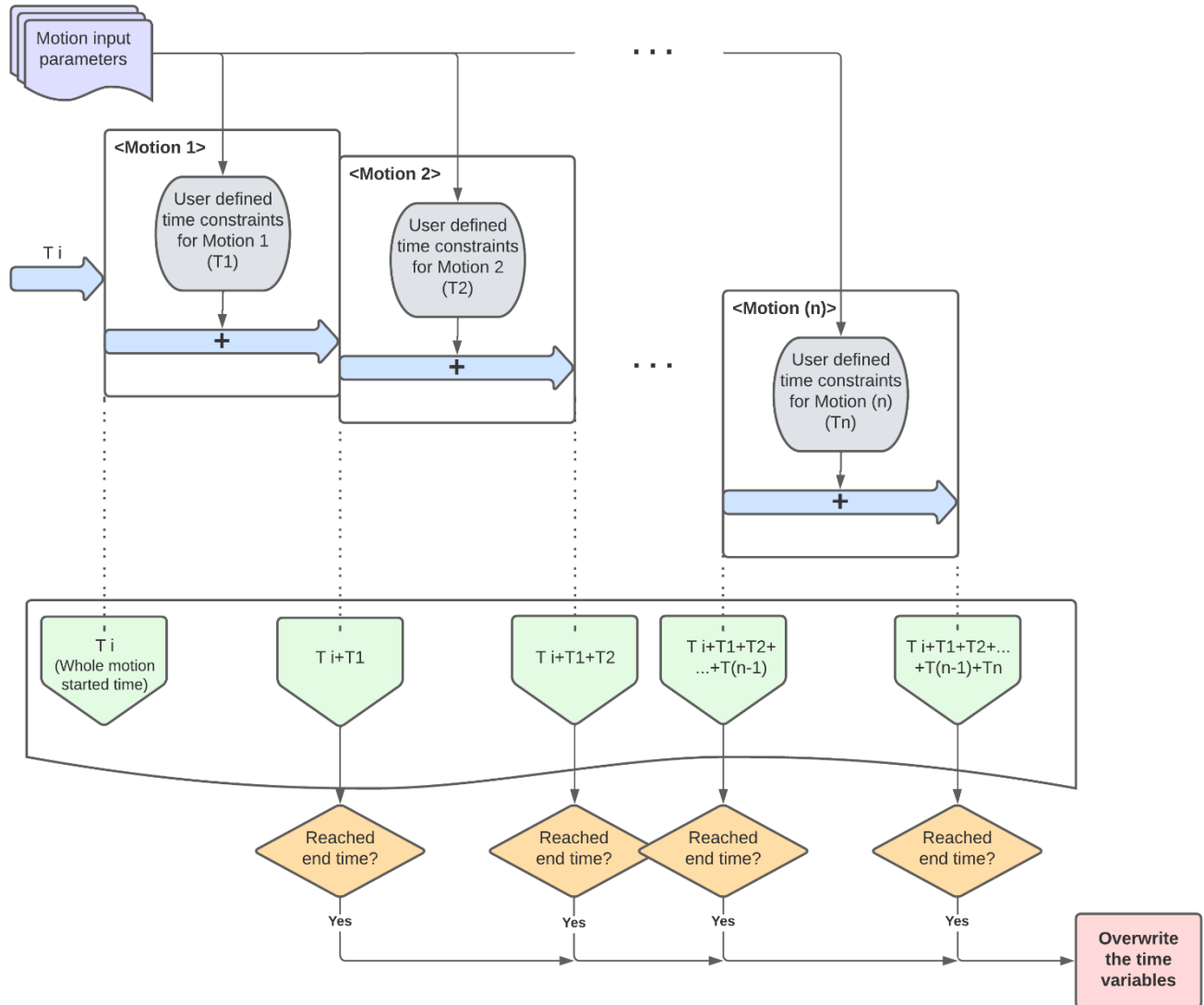
Figure 23 - Data flow of time variable in the new RTS control loop

To avoid these possible problems, the RTS's control loop system design is adjusted to add motion ending time, allowing the control system to determine when to terminate the presently running motion and begin the next. As seen in Figure 23, the new RTS control loop can determine when the present motion should be stopped. To be precise, as seen in Figure 24, the

new function generator uses the same input variables as the original function generator (e.g., Function type, Control type, Parameter A, B, C, D). Additionally, a group of new variables is introduced into the new function generator (e.g., t (system real-time), ti (motion starting time of current motion)). The new variables are used to store the system's current time, which can be compared to the calculated completion time of the presently executing motion.
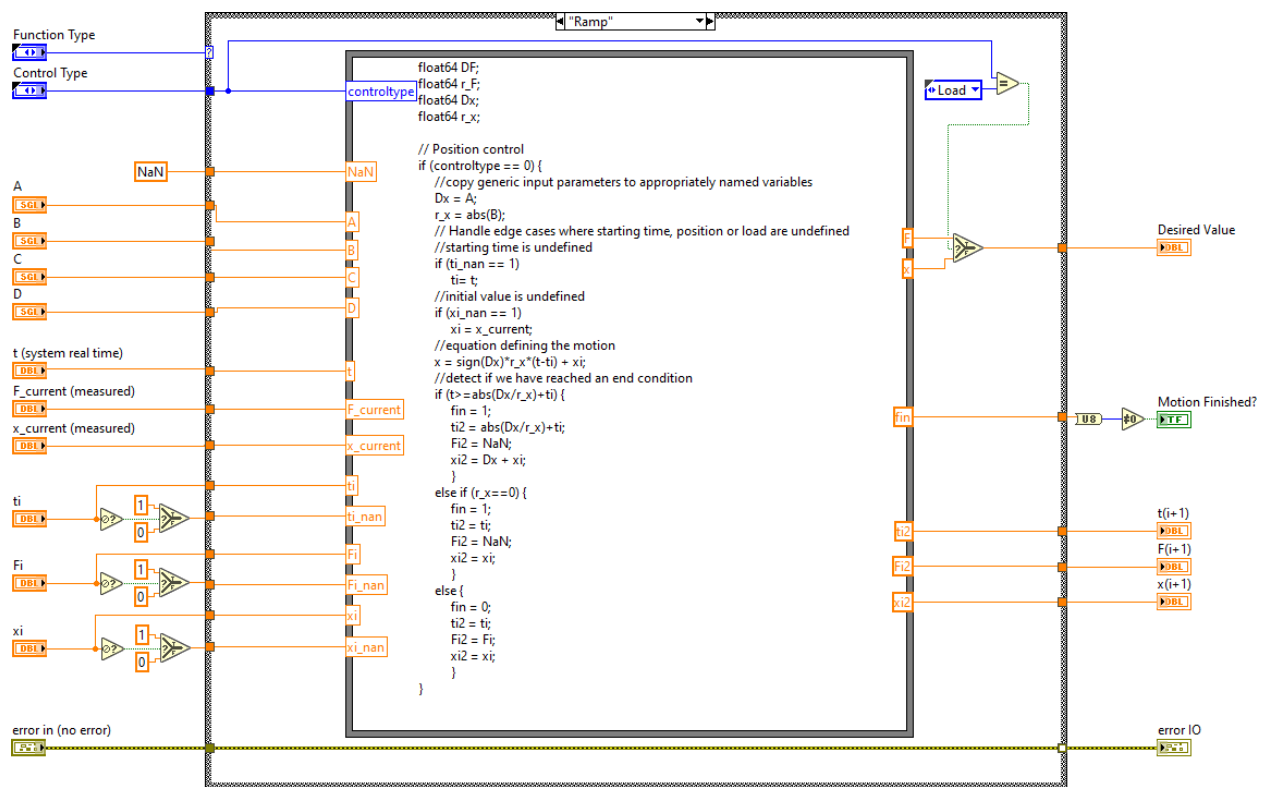
Figure 24 - The new function generator (diagram with inputs and outputs)

To clarify, the new function generator's 'Formula Node,' as seen in Figure 25, has an end condition:

$$\text{if } (t > abs(Dx/r\_x) + ti)$$

, utilizing the user input parameters ('Dx' and 'r_x') to calculate current motion finishing time, which is a significant distinction from the original function generator's separate 'End Condition' VI. The criteria's purpose is to determine if the system has reached the end of the presently running motion and go to the next one by providing the value '1' to the output variable designated 'fin' on the right side wall of the 'Formula Node.'

```
                float64 DF;
                float64 r_F;
controltype     float64 Dx;
                float64 r_x;

                // Position control
                if (controltype == 0) {
NaN                 //copy generic input parameters to appropriately named variables
                    Dx = A;
A                   r_x = abs(B);
                    // Handle edge cases where starting time, position or load are undefined
B                   //starting time is undefined
                    if (ti_nan == 1)
C                       ti= t;
                    //initial value is undefined
D                   if (xi_nan == 1)
                        xi = x_current;
                    //equation defining the motion
                    x = sign(Dx)*r_x*(t-ti) + xi;
t                   //detect if we have reached an end condition
                    if (t>=abs(Dx/r_x)+ti) {
F_current               fin = 1;
                        ti2 = abs(Dx/r_x)+ti;
                        Fi2 = NaN;
x_current               xi2 = Dx + xi;
                    }
ti                  else if (r_x==0) {
                        fin = 1;
ti_nan                  ti2 = ti;
                        Fi2 = NaN;
Fi                      xi2 = xi;
                    }
Fi_nan              else {
                        fin = 0;
xi                      ti2 = ti;
                        Fi2 = Fi;
xi_nan                  xi2 = xi;
                    }
                }
```

Figure 25 - Formula Node of the new function generator ('Ramp' mode – Position control)

By including user-specified processing time limitations into the function generator, the RTS machine can accurately perform planned movements within a critically determined completion time, hence meeting the criteria of a Real-time Operating System (RTOS).

In addition to the Real-time operational conditions, several different mechanical testing projects at BMEL have shown the need to develop a curve, or mathematical function, that fits the user-supplied data points the best to generate motion profiles. This approach, termed "Curve fitting," may be used in conjunction with interpolation, which needs a precise fit to the data. A broader statement regarding curve fitting is that it will exactly match any constraint specified by the user, such as points, angles, or a curvature. Angle and curvature constraints are often applied to curves' terminals and are referred to as end conditions. A set of unique cubic polynomials is fitted between each user-defined data point, with the restriction that the resulting curve is continuous and seems smooth. Among the available curve fitting techniques, a cubic spline is selected for the RTS function generator due to its advantages in terms of smooth interpolated curves, numerical stability, and calculation ease.[20] In comparison, the spline approach based on a first-order polynomial has drawbacks such as a sudden change in slope at the node, or data point. Additionally, the spline based on a second-order polynomial cannot have continuous second-order derivatives at the nodal points, which is required for a smooth slope changing rate.
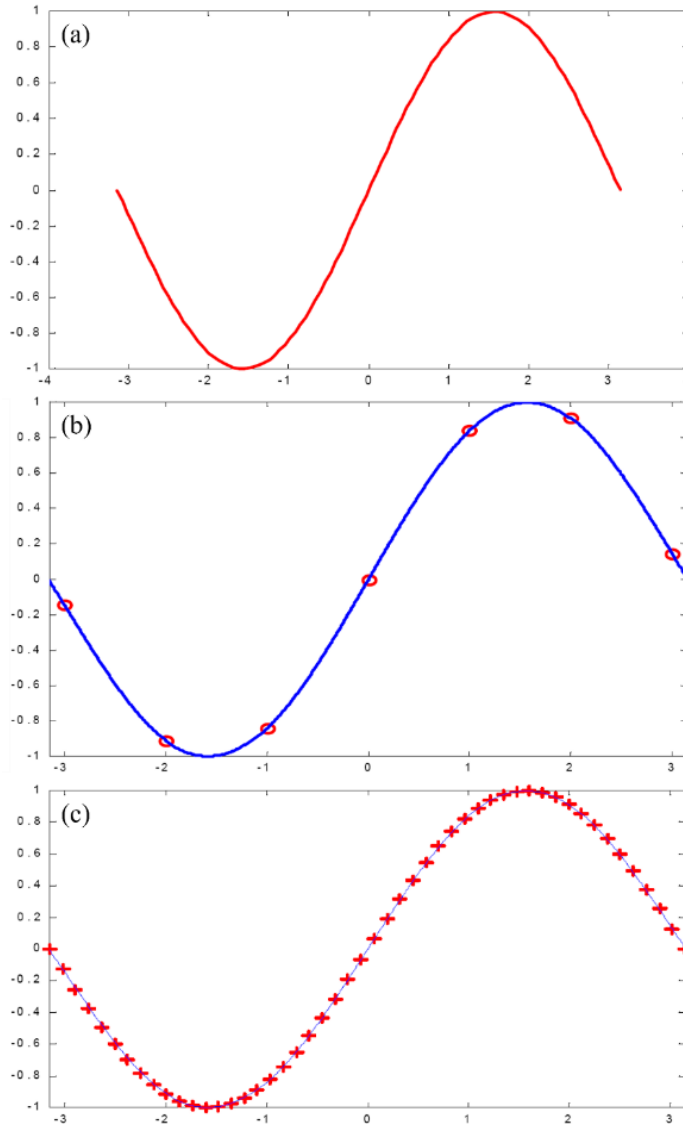
Figure 26 - (a) The plot of y = sin(x), (b) Spline through seven points on a sine curve, (c) Superimposition of a spline curve on a sine function [20]

To apply the cubic spline for the new function generator, it is necessary to understand how to derive the cubic spline equation of each segment. First, the piecewise function of the third-degree polynomial form is needed to fit into the given node. Let us assume $f_i(x) = a_i +$

$b_i(x - x_i) + c_i(x - x_i)^2 + d_i(x - x_i)^3$ and we have (n) number of node points (e.g.,

$(x_1, f_1(x_1)), (x_2, f_2(x_2)), (x_3, f_3(x_3)), \cdots, (x_{n-1}, f_{n-1}(x_{n-1})), (x_n, f_n(x_n))$). To acquire the n

number of piecewise functions of $f_i(x)$ in each segment between two consecutive nodes, we

need four coefficients a_i, b_i, c_i, d_i for each function which means that totally 4n (= (4

coefficients) times (n equations), equations are required. The spline functions will need to meet

the following four conditions to derive the coefficients.

(1) All the piecewise function $f_i(x)$ should interpolate all data points.

(2) $f_i(x)$ should be continuous on every node

(3) The first derivative of $f_i(x)$ should be continuous on every node

(4) The second derivative of $f_i(x)$ should be continuous on every node

- Condition (1): All the piecewise function $f_i(x)$ should interpolate all data points.

  By inputting (a_i, f_i), where $i = (1,2,3, \cdots, n)$, into the equation

  $$f_i(x) = a_i + b_i(x - x_i) + c_i(x - x_i)^2 + d_i(x - x_i)^3$$

  it becomes $a_i = f_i$. So, we acquired all the a_i $(i = 1,2,3, \cdots, n)$ coefficients.

  Thus, the equation will be:

  Eq①: $f_i(x) = f_i + b_i(x - x_i) + c_i(x - x_i)^2 + d_i(x - x_i)^3$

- Condition (2): $f_i(x)$ should be continuous on every node

  To meet the condition, $f_i(x_{i+1})$ should have the same value with $f_{i+1}(x_{i+1})$ at the x_{i+1} node

  as a_{i+1}. Given this, we can derive the equation:

Eq②: $f_i + b_i(x_{i+1} - x_i) + c_i(x_{i+1} - x_i)^2 + d_i(x_{i+1} - x_i)^3 = f_{i+1}$

, where $i = (1,2,3,\cdots,n)$

- Condition (3): The first derivative of $f_i(x)$ should be continuous on every node

  To meet the third condition, as similar to the second condition, $f_i'(x_{i+1})$ should have the same value with $f'_{i+1}(x_{i+1})$ at the x_{i+1} node. Given this, we can derive the equation:

  Eq③: $b_i + 2c_i(x_{i+1} - x_i) + 3d_i(x_{i+1} - x_i)^2 = b_{i+1}$

  since $f'_{i+1}(x_{i+1}) = b_{i+1}$, where $i = (1,2,3,\cdots,n)$

- Condition (4): The second derivative of $f_i(x)$ should be continuous on every node

  To meet the last condition, as similar to the second and third conditions, $f_i''(x_{i+1})$ should have the same value with $f''_{i+1}(x_{i+1})$ at the x_{i+1} node. Given this, we can derive the equation:

  Eq④: $2c_i + 6d_i(x_{i+1} - x_i) = 2c_{i+1}$

  since $f''_{i+1}(x_{i+1}) = 2c_{i+1}$, where $i = (1,2,3,\cdots,n)$

- From the Eq④, we can acquire $d_i = \frac{c_{i+1} - c_i}{3(x_{i+1} - x_i)}$ (=Eq⑤)

- By inserting the Eq⑤ into Eq②, $b_i = \frac{f_{i+1} - f_i}{(x_{i+1} - x_i)} - \frac{(x_{i+1} - x_i)}{3}(2c_i + c_{i+1})$ (=Eq⑥)

- From the Eq⑥, we can also acquire $b_{i-1} = \frac{f_i - f_{i-1}}{(x_i - x_{i-1})} - \frac{(x_i - x_{i-1})}{3}(2c_{i-1} + c_i)$ (=Eq⑦)

- By inserting the Eq⑤ into Eq③, $b_i = b_{i-1} + (x_i - x_{i-1})(c_{i-1} + c_i)$ (=Eq⑧)

54

- Given that being described, by inserting the Eq⑥, ⑦ into Eq⑧ and rearranging the equation, we will have:

$$h_{i-1}c_{i-1} + 2((x_i-x_{i-1}) + (x_{i+1}-x_i))c_i + h_ic_{i+1} = 3\frac{f_{i+1}-f_i}{x_{i+1}-x_i} - 3\frac{f_i-f_{i-1}}{x_i-x_{i-1}} \quad (=\text{Eq}⑨)$$

- At the very first node, we know the value of the second derivative as $f''_1(x_1) = s_1 = 2c_1 + 6d_1(x_1 - x_1) \rightarrow \therefore c_1 = s_1/2$

- At the very last node, we know the value of the second derivative as $f''_{n-1}(x_n) = s_{n-1} = 2c_{n-1} + 6d_{n-1}(x_n - x_{n-1}) \rightarrow \therefore c_{n-1} = (s_{n-1} - 6d_{n-1}(x_n - x_{n-1}))/2$

- Thus, by summarizing the derived equation into linear algebra form,

$$[A][B] = [C], \text{ where A, B, C is as follows.}$$

$$A = \begin{bmatrix} 2(x_2-x_1) & (x_2-x_1) & \ddots & \ddots & & \ddots & & \ddots \\ (x_2-x_1) & 2((x_2-x_1) + (x_3-x_2)) & \ddots & \ddots & & \ddots & & \ddots \\ \ddots & \ddots & \ddots & \ddots & & \ddots & & \ddots \\ \ddots & \ddots & \ddots & \ddots & & \ddots & & \ddots \\ \ddots & \ddots & \ddots & \ddots & (x_{n-1}-x_{n-2}) & 2((x_{n-1}-x_{n-2}) + (x_n-x_{n-1})) & (x_n-x_{n-1}) \\ \ddots & \ddots & \ddots & \ddots & & (x_n-x_{n-1}) & 2(x_n-x_{n-1}) \end{bmatrix}$$

$$B = \begin{bmatrix} c_1 \\ c_2 \\ \ddots \\ \ddots \\ c_{n-1} \\ c_n \end{bmatrix}$$

$$C = \begin{bmatrix} 3(\dfrac{f_2 - f_1}{x_2 - x_1} - f'_1) \\ 3(\dfrac{f_3 - f_2}{x_3 - x_2} - \dfrac{f_2 - f_1}{x_2 - x_1}) \\ \ddots \\ \ddots \\ 3(\dfrac{f_n - f_{n-1}}{x_n - x_{n-1}} - \dfrac{f_{n-1} - f_{n-2}}{x_{n-1} - x_{n-2}}) \\ 3(f'_n - \dfrac{f_n - f_{n-1}}{x_n - x_{n-1}}) \end{bmatrix}$$

- By calculating the linear algebra to find [B], as shown below,

$$[B] = [A]^{-1}[C]$$

- By applying the derived c_i ($i = 1,2,3, \cdots, n$) to Eq⑤, ⑥, we can acquire b_i and d_i ($i = 1,2,3, \cdots, n$) accordingly.

- As a result, by utilizing the derived coefficients a_i, b_i, c_i and d_i ($i = 1,2,3, \cdots, n$), we finally obtain $f_i(x) = a_i + b_i(x - x_i) + c_i(x - x_i)^2 + d_i(x - x_i)^3$ for each segment in interval $[x_1, x_n]$.

- Based on this general equation, in our case, the A, B, and C matrices are as follows.

$$AB = \begin{bmatrix} 2(x_2 - x_1) & (x_2 - x_1) \\ (x_2 - x_1) & 2(x_2 - x_1) \end{bmatrix} \begin{bmatrix} c_1 \\ c_2 \end{bmatrix}$$

$$C = \begin{bmatrix} 3(\dfrac{f_2 - f_1}{x_2 - x_1} - f'_1) \\ 3(f'_2 - \dfrac{f_2 - f_1}{x_2 - x_1}) \end{bmatrix}$$

- By solving the linear algebra and using Eq⑤, ⑥, the coefficient for the equation:

$$f_i(x) = a_i + b_i(x - x_i) + c_i(x - x_i)^2 + d_i(x - x_i)^3 \text{ are as follows.}$$

$$a = f_1(x_1)$$

$$b = f'_1(x_1)$$

$$c = \frac{\left(-f'_2(x_2) - 2f'_1(x_1) + 3(f_2(x_2) - f_1(x_1))/(x_2 - x_1)\right)}{(x_2 - x_1)}$$

$$d = \frac{f'_1(x_1) + f'_2(x_2)}{(x_2 - x_1)^2} - \frac{2(f_2(x_2) - f_1(x_1))}{(x_2 - x_1)^3}$$

Given the established cubic spline equation, we developed the new function generator's 'Cubic Spline' mode using LabView's 'Formula Node' and C-syntax structured programming language. As a result of this accomplishment, the RTS can conduct spline movements in response to the user's request for a smooth curve fitted to user-defined set points, as seen in figure 24.

```
                float64 DF;
                float64 Dx;
controltype     float64 Dt = abs(B);
                float64 slope1 = C;
                float64 slope2 = D;

                float64 a;
NaN             float64 b;
                float64 c;
                float64 d;

                //  Position control
A               if (controltype ==0) {
                    //copy generic input parameters to appropriately named variables
B                   Dx = A;                                                              F
                    // Acquire cubic polynomial coefficients
C                   a = (slope1+slope2)*(Dt**(-2)) - 2*(Dx)*(Dt**(-3));                   x
                    b = (-slope2 - 2*slope1 + 3*(Dx)*(Dt**(-1)))/(Dt);
D                   c = slope1;
                    // Handle edge cases where starting time, position or load are undefined
                    //starting time is undefined
                    if (ti_nan == 1)
                        ti= t;
                    if (xi_nan == 1)
                        xi = x_current;
                    //equation defining the motion
t                   d = xi;
                    x = a*((t-ti)**3) + b*((t-ti)**2) + c*(t-ti) + d;
F_current           //detect if we have reached an end condition                        fin
                    if (t>=Dt+ti) {
                        fin = 1;
x_current               ti2 = Dt+ti;
                        Fi2 = NaN;                                                       ti2
ti                      xi2 = Dx + xi;
                        }                                                                Fi2
ti_nan              else {
                        fin = 0;                                                         xi2
                        ti2 = ti;
Fi                      Fi2 = Fi;
                        xi2 = xi;
Fi_nan                  }
xi                  }

xi_nan
```

Figure 27 - 'Cubic Spline' mode of the new function generator

2.3.3. User interface development in accordance with the new function generator

As a result of the system architecture being modified to accommodate the new function generator, adjusting the user interface to fit the new system contexts became required. Along with functional compliance, the user interface will have enhanced user-friendly features that will

allow users to quickly upload a large number of movements at once and edit the uploaded motions directly within the user interface.

To begin, as seen in Figure 15, the initial user interface demands that movements be composed using nine parameters and conditions.

(1) Control type: Position / Load

(2) Function type: Ramp / Sinusoidal / Creep

(3) Parameter A

(4) Parameter B

(5) Parameter C

(6) P Gain

(7) I Gain

(8) Duration

(9) Tolerance

In the case of Parameters A, B, and C, the parameters are determined by the function's type, as indicated in the following table.

Function type	Parameter A	Parameter B	Parameter C
Ramp	Slope (mm/s)	End Position (mm)	Not used
Sinusoidal	Period (s)	Mean (mm)	Amplitude (mm)
Creep Test	Slope (mm/s)	Hold Point (mm)	Hold Time (s)

Table 1 - Parameters determined by function types (original RTS system, position control mode)

Compared to the previous function generator, the new function generator needs improved motion

parameters to attain better motion composition capabilities, as seen in Figure 28.

        (1) Control Type

        (2) Function Type

        (3) Parameter A

        (4) Parameter B

        (5) Parameter C

        (6) Parameter D

        (7) P Gain

        (8) I Gain

Motion Parameters

Motion#		Control Type	Function Type	A	B	C	D	P Gain	I Gain
0	●	Position	Indefinite Hold	0	0	0	0	5	0.01
0	●	Position	Ramp	0	0	0	0	0	0
0	●	Position	Ramp	0	0	0	0	0	0
0	●	Position	Ramp	0	0	0	0	0	0
0	●	Position	Ramp	0	0	0	0	0	0
0	●	Position	Ramp	0	0	0	0	0	0
0	●	Position	Ramp	0	0	0	0	0	0
0	●	Position	Ramp	0	0	0	0	0	0
0	●	Position	Ramp	0	0	0	0	0	0
0	●	Position	Ramp	0	0	0	0	0	0
0	●	Position	Ramp	0	0	0	0	0	0
0	●	Position	Ramp	0	0	0	0	0	0
0	●	Position	Ramp	0	0	0	0	0	0
0	●	Position	Ramp	0	0	0	0	0	0
0	●	Position	Ramp	0	0	0	0	0	0

Figure 28 - Motion parameter storing array (compliant with the new function generator)

Similar to the previous motion parameter setting, the values for Parameter A, B, C, and D are decided by the function type, as indicated in the following table.

Function type	Parameter A	Parameter B	Parameter C	Parameter D
Ramp	Difference (mm, relative)	Slope (mm/s)	Not used	Not used
Sinusoidal	Amplitude (mm)	Frequency (Hz)	Phase (degrees)	Cycle (#)
Triangular	Rising Slope (mm/s)	Falling Slope (mm/s)	Period (s)	Cycle (#)
Cubic Spline	Difference (mm, relative)	Duration (s)	Start Slope (mm/s)	End Slope (mm/s)
Indefinite Hold	Target Load (N, absolute)	Tolerance (N)	Not used	Not used

Table 2 - Parameters determined by function types (the new RTS system, position control mode)

Compared to the previous motion parameter set, a differentiating aspect is a rise in the number of demanding parameters from three to four, indicating that extra parameters were required to construct advanced movements. The function types are described in-depth, ranging from three (Ramp, Sinusoidal, and Creep) to five (Ramp, Sinusoidal, Triangular, Cubic Spline, and Indefinite Hold). To be more detailed with the Sinusoidal waveform function, the new function generator gained the ability to alter the 'Phase change' parameter to meet better the user's needs for commencing velocity control.

Furthermore, the mechanism for uploading and storing motion parameters may well be addressed. Due to the removal of capacity constraints on storing movements in an array, there is

an increased necessity for convenience when building motion profiles to manage a high number of motions. To facilitate the handling of motion profile parameters, an external txt format file uploading mechanism was suggested. The apparent advantage of this technique is that the user may create the motion profile on any computer that does not include LabView software. Additionally, all that the user requires is to duplicate motion profile templates to fill the number of demanding motions necessary to construct a significant number of movements.

As seen in Figure 29, a text file containing motion parameters is intended to be compatible with uploading motion profiles to RTS's user interface. The sequence of the parameters corresponds to the user interface's array of motion input parameters, as seen in Figure 28. The data must have the following elements in the order specified to enter the motions.

(1) Motion number: Integer and zero (must start with zero)

(2) Control type: Position / Load

(3) Function type: Ramp / Sinusoidal Wave / Triangular Wave / Cubic Spline Curve / Indefinite Hold

(4) Parameter A

(5) Parameter B

(6) Parameter C

(7) Parameter D

(8) P Gain

(9) I Gain

(* The detailed information regarding the Parameter A, B, C, and D is as Table 2.)

```
Test_12.21.21.txt - Notepad
File  Edit  Format  View  Help
0        Position        Ramp    10      1       0       0       5       0.01
1        Position        Sinusoidal Wave 10      0.2     0       2       5       0.01
2        Position        Cubic Spline Curve      -10     10      0       0       5       0.01
3        Position        Triangular Wave 2       3       5       2       5       0.01
4        Position        Cubic Spline Curve      10      10      0       0       5       0.01
5        Position        Ramp    5       1       0       0       5       0.01
6        Position        Sinusoidal Wave 5       0.2     0       2       5       0.01
7        Position        Cubic Spline Curve      -5      10      0       0       5       0.01
8        Position        Triangular Wave 2       3       10      2       5       0.01
9        Position        Cubic Spline Curve      5       5       0       0       5       0.01
10       Position        Ramp    -10     1       0       0       5       0.01
11       Position        Sinusoidal Wave 10      0.1     0       2       5       0.01
12       Position        Cubic Spline Curve      10      10      0       0       5       0.01
13       Position        Triangular Wave 3       2       5       2       5       0.01
14       Position        Cubic Spline Curve      -5      10      0       0       5       0.01
15       Position        Ramp    7       1       0       0       5       0.01
16       Position        Sinusoidal Wave 7       0.2     0       2       5       0.01
17       Position        Cubic Spline Curve      -7      10      0       0       5       0.01
18       Position        Triangular Wave 1       3       10      2       5       0.01
19       Position        Cubic Spline Curve      -7      5       0       0       5       0.01

Ln 20, Col 47      100%    Windows (CRLF)    UTF-8
```

Figure 29 - txt format file containing twenty motions' parameters

By uploading the motion parameters in a text file format, the user interface ('Set Movement Parameters' VI) is automatically filled with the motion parameters, as shown in Figures 30 and 31. Following this successful uploading and storing of user inputs via the LabView interface, editing motions, such as adding, deleting, changing values, and switching the order of motions, enables the user to revise and modify motion parameters directly in the user interface, without having to make changes to the txt file and upload the txt file again.

Figure 30 - Display appeared following the ' Upload Motion Profiles' button activation

Figure 31 - Uploaded motion profiles on the user interface

2.4. Conclusion

As a consequence of the RTS operating per the uploaded motion profile, Figure 32 depicts the successfully storing, transferring, and executing user-determined motion parameters in the Target (cRIO). Each parameter in the resulting 'tdms' format data file is identical to the txt file supplied to the RTS, as seen in Figure 29.

Figure 32 - Saved motion profiles information run in the RTS

Furthermore, Figure 33 presents the position readouts acquired in the millimeter unit by converting the electric voltage signal collected from the LVDT sensor installed to the RTS machine. As it is seen, the 20 motions that were user-designed using a txt file were well operated.
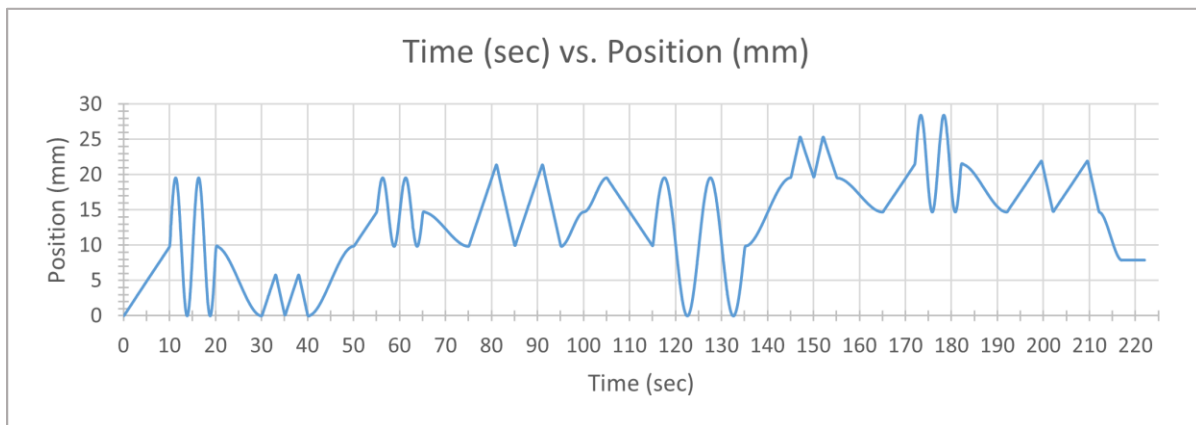
Figure 33 - Time (s) vs. Position (mm) graph

Given the result data, the following interpretations become available.

(1) The newly developed function generator for the RTS can utilize an arbitrarily large number of motions in a motion profile, despite the FIFO buffer size (= 10) being smaller than the user-published motion numbers (= 20). As a result, the RTS system's motion processing is not bound by a finite array size and FIFO buffer size.

(2) The new motion profile generator's 'Cubic Spline' function has been tested and proved to be error-free. This function effectively interpolates smooth curves between two

67

successive user-defined points. This accomplishment will likely benefit users who demand smooth motion profiles depending on a few user-supplied parameters.

(3) The enhanced RTS system gained the ability to upload, save, and edit user-defined motion parameters. Additionally, metering and assigning movements to a FIFO buffer with a finite size is validated based on the successful operation of handling a more significant number of user-specified motions than the FIFO buffer size.

2.5. Discussions of new features and capabilities

While capabilities have been expanded, drawbacks have been identified for future development. To begin, exporting the altered motion profiles from the user interface is required to be utilized for subsequent testing. Second, those unfamiliar with the user interface will have difficulty seeing how the motion profiles will happen. It is vital to keep simulated plots generated using user-defined parameters to understand the movements intuitively. It will be very beneficial to get insight into the actuator's sharp inflection point positioning to avoid a sudden jump. Finally, the LabView version used by the RTS machine is 2016, which is quite old. A difficulty in the early stages of developing the new control system was obtaining a license for LabView 2016. Additionally, since the oldest version of LabView for which NI provides significant updates is LabView 2018, it is necessary to rebuild the RTS control system code in the most recent version of LabView, such as 2021, for future RTS system improvements.

CHAPTER III

DEVELOPMENT OF PUSH-OUT TEST APPARATUS FOR RODENT BILATERAL

CALVARIAL DEFECT REPAIRS

3.1. Introduction

Defects in the calvarial bone may arise as a consequence of tumor excision, congenital abnormalities, or surgical burr holes. For therapeutic reasons, the gold standard is often the harvesting of cancellous autografts from several body areas of the same patient. They do, however, come with donor scarcity, donor site morbidity, and complicated grafting operations.[21] Alternative treatments such as allografts and bone cement are seldom employed since they are poor at promoting bone healing.[22] Another difficulty with autografts is the need to shape the hard tissue (e.g., bone) to suit the defect precisely.[23] A gap between the graft and the surrounding bone tissue impedes osseointegration and increases the chance of graft disintegration.[24] Tissue engineering has developed a viable therapeutic option for calvarial bone abnormalities taking these limits into account. A predefined scaffold with particular qualities is important to the success of the approach. To begin, the scaffold must maintain close contact with the adjacent bone tissue in order to facilitate osseointegration while avoiding brittle mechanical properties that might result in fracture. Additionally, the scaffold should be bioactive, which implies it should promote bone tissue integration. Finally, the scaffold must allow for the movement of nutrients.[25]

In 2014, Dr. Melissa Grunlan's research group at Texas A&M University and Dr. Mariah Hahn's research group in Rensselaer Polytechnic Institute proposed a Shape Memory Polymer

(SMP) scaffold meeting the qualifications, such as being capable of accurately self-fitting and bioactive.[26]

3.2. Research backgrounds

3.2.1. Self-fitting SMP scaffold

The self-fitting Shape Memory Polymer (SMP) scaffold is a thermoresponsive polymer that is shaped and fixed by heat. It is composed of PCL (Poly-ε-caprolactone) and PDMS or PSE, depending on the degradation rate adjustment level.[27] The SMP scaffold is constructed in such a way that it retains the linked pores required for cell integration. The unique characteristics of this SMP scaffold include its self-fitting ability and bioactivity for osseointegration and osteoinductivity, and also the functionality of a specific coating called 'polydopamine.' Polydopamine's thin layer (~ 40nm) is known to introduce hydrophilic qualities that stimulate cell attachment and proliferation.[28],[29] Additionally, the ability to tune the cell migration rate by varying the PDMS segment length means that the scaffold's pore size may be adjusted.[30] Mechanical properties of the non-sterilized SMP scaffold were determined utilizing compression tests on scaffold specimens (N=3, diameter=9mm x thickness=1mm) at room temperature using an Instron 5944. The compressive modulus (E) of the linear region ($\leq$ 10% strain) was determined to be 22.1 $\pm$ 4.2 MPa at a constant strain rate (1.5mm/min) up to 85 % strain. Additionally, the compressive strength (CS) was calculated to be 25.8 $\pm$ 2.0 MPa based on the stress at 85 % strain. [25]

70

3.2.2. Sample preparation

3.2.2.1. Fabrication of self-fitting SMP scaffolds

Scaffolds were created by following the instructions below using PCL-diacrylate (PCL-DA).[25]

(1) Prepare a fused salt template by combining and stirring 10.0 grams sieved salt with 7.5 weight percent DI water in a 20 mL glass vial, centrifuging (3220 x g, 15 minutes), and drying under vacuum (30 in. Hg, room temperature, overnight).

(2) Combine a PCL-DA solution (0.15 g/mL DCM) with a photoinitiator solution at a concentration of 15%. (10 wt percent DMAP in NVP).

(3) To enhance solution diffusion throughout the fused salt template, add the vortexed macromer solution (5mL) and centrifuge (1260 x g, 10 min).

(4) Cure the PCL-DA in the vial under UV-light (6 mW/cm^2, 365 nm, 5 min).

(5) Remove the cylindrical specimen from the vial and trim it.

(6) Remove the salt template by immersing the specimen in a 1:1 solution of water and ethanol for four days with daily solution changes.

(7) Allow the specimen to air dry for 12 hours at room temperature before proceeding with the annealing procedure (30 in. Hg., 85 degrees Celsius, 1 hour).

(8) Slicing and punching the cylindrical specimen into disks with a diameter of 9mm and a thickness of 1mm or 1.5 mm

71

3.2.2.2. Scaffold preparation for mechanical testing

The Institutional Animal Care and Use Committee (IACUC) at Texas A&M University (AUP 2016-0348) authorized the research in which sixty Fischer rats (male, 8 weeks old) were treated bilaterally for non-critical cranial bone defects with a diameter of 5 mm. Following that, the scaffolds were submerged for 30-60 seconds in warm saline water (55 degrees Celsius) before implantation. Because the SMPs are malleable, they could be gently pushed into the defects. By cooling to 55 degrees Celsius and reverting to its original geometries, the scaffold maintains intimate contact with the bone tissue, and the form is securely held inside the defect holes. The rats are euthanized four weeks after implantation to determine bone tissue migration and osteogenesis. To compare defects repaired using SMP scaffolds to defects treated with autograft, a biomechanical push-out test was conducted.

In terms of sample size, thirty rat calvarial bones with bilateral defects were mechanically characterized using the push-out technique. As a result, the total sample size for the push-out test became sixty (N= 60). As seen in the accompanying table, the samples are classified into one clinical gold standard group, and four unique groups based on the presence of two components (i.e., polydopamine coating and bone marrow-derived mesenchymal stem cells (BMSCs)) applied to the samples. The basic scaffold was constructed with a 75:25 wt% proportion of PCL and PLLA with a diameter of 5.5mm and a thickness of 1.5mm following the instructions stated in section 3.2.2.1.[31]

Sample group	Polydopamine coating	BMSCs	Sample number (N)	Note
Group 1 (control)	Autograft ('Bone flap')		12	Clinical gold standard
Group 2	uncoated	not applied	12	Scaffold (PCL/PLLA: 75/25 wt%)
Group 3	uncoated	applied	12	Scaffold (PCL/PLLA: 75/25 wt%)
Group 4	coated	not applied	12	Scaffold (PCL/PLLA: 75/25 wt%)
Group 5	coated	applied	12	Scaffold (PCL/PLLA: 75/25 wt%)

Table 3 - Sample groups classified based on the presence of bioactive coating and BMSCs

3.3. Test Method

Mechanical push-out tests for assessing the shear strength of the graft-bone interface induced by osteogenesis are regarded to confirm the unique SMP scaffolds'outstanding functionalities (i.e., bioactivity and osteoinductivity) in facilitating the healing of a cranial bone defect. This part will assess test equipment used to execute push-out tests, produce two kinds of prototypes, and develop the final test apparatus based on the findings from the previous devices.

3.3.1. Push-out test apparatus designed and utilized in other studies

P. Lohmann (2017)[32] released push-out test results evaluating bone regeneration induced by biomaterial implantation in 2017. To perform the mechanical testing, a metallic sample fixture, or jig, is constructed to keep the sample aligned with a 5 mm diameter indenter, as seen

73

in Figure 34. The author did not describe how he ensured that the bone defect hole and indenter were axially aligned. Given the uncertainty, two hypotheses may be advanced: (1) the indenter is centered in the defect site using visual inspection, or (2) an alignment supporting device is used to achieve accurate axial alignment.
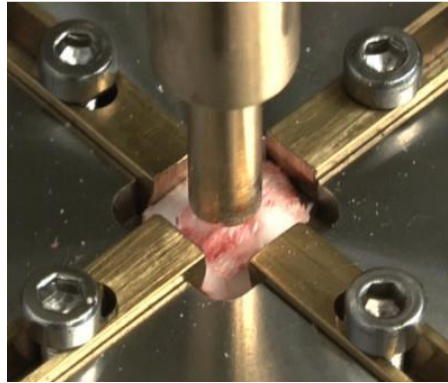
Figure 34- Mechanical push-out tests performed with a 5 mm diameter indenter[32]

By referring to 'Lohmann, P. et al. (2017)' [32], the following design aspects of the push-out test device can be considered.

(1) Two separate parts are needed: a sample fixture and an indenter with a diameter of the bone defect size

(2) Parts sliding along with slots are required to hold and support the sample in a definite position.

(3) A method to align the push-out rod to the bone defect is required to prevent sample damage by the indenter in action.

74

In addition, 'Kwon, J. et al. (2019)'[33] has reported a novel scaffold made of titanium (Ti) mesh and Gelfoam® to mitigate dislocation of the scaffolds radially and axially. To test the shear strength, the research team developed a custom push-out test fixture, as is seen in Figure 35.
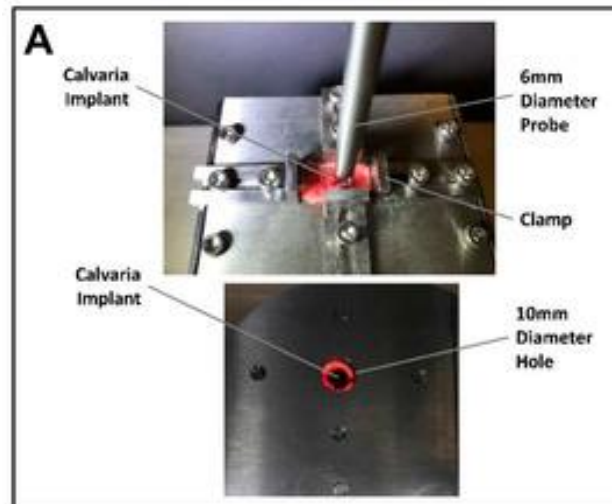
Figure 35 - Push-out test apparatus designed and used in 'Kwon, J. (2019)'[33]

Both the 'Lohmann, P., et al. (2017)' [32] and 'Kwon, J., et al. (2019)'[33] tests need the sample fixture, as does the push-out rod connected to the load frame. Additionally, the test equipment mentioned in 'Kwon, J., et al. (2019)'[33] does not provide instructions for positioning the rod in relation to the bone defect.

Across the two push-out test apparatus, the existence and size of the through-hole on the fixture, as well as the clearance between the diameter of the push-out rod and the diameter of the through-hole on the base, were verified. For instance, the 'Lohmann, P. et al. (2017)' research[32] failed to disclose the existence and size of a through-hole in the fixture base. As a result of this,

the author may overlook the necessity of the through-hole diameters and the clearance between the indenter rod and defect hole. In the instance of 'Kwon, J. et al. (2019)'[33], a through-hole with a diameter of 10 mm is present. Additionally, the indenter size is specified as 6mm, which yields a 2 mm clearance between the indenter and the fixture through the hole.

3.3.2. Design requirements derived from benchmarking of pre-existing test equipment

Following a review of the test equipment used in previous research, the following design criteria were identified to guide the development of the new test apparatus employed in this research.

    (1) Push-out test apparatus is composed of a sample fixture and an indenter (or push-out rod)

    (2) Sample fixture

        a. Material: Previous studies used metallic materials, most notably aluminum or steel, based on their hue.

        b. Sample holding components (i.e., clamps, handles, or narrow sliding jaws) are needed to secure samples in place.

        c. Base may need a through-hole to avoid interfering with the indenter's operation.

    (3) Indenter rod

        a. Material: Previous studies used metallic materials, most notably brass or steel, based on their hue.

b. Clearance between the diameter of the indenter and the diameter of the base through-hole needs to be considered.

(4) To execute accurate push-out tests without damaging samples, a method for aligning one component to another between fixture and indenter rod is required.

Along with the above-mentioned design criteria, this research includes one additional requirement: holding and testing samples with bilateral bone defects. The prior study used a test device to evaluate samples with a unilateral bone defect. As a result, isolating one of two defects on the same sample was not necessary. Concerns were raised regarding causing damage to one of two defects in the same sample while trying to fix the defect of interest for push-out testing. To address the possible issue, a different method of sample fixation must be investigated.

3.3.3. Prototypes

To validate the design criteria and assess a test equipment comparable to that used in the previous study, two prototypes are created based on the design requirements stated in section 3.3.2.

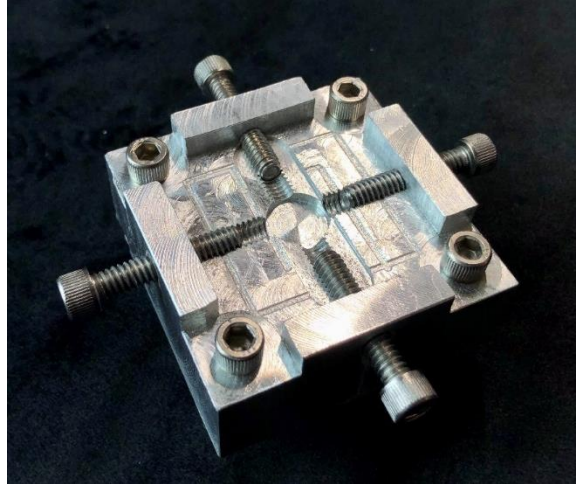**Figure 36 - The first attempt of prototyping (sample fixture)**

The first prototype (Figure 36) was created to assess the lateral compressive fixing technique for securing samples. The four two-inch-long 1/4-20 Hex Socket Cap Head bolts were used to imitate the function of sliding jaws seen in Figure 34. (Yellow-colored metallic components).
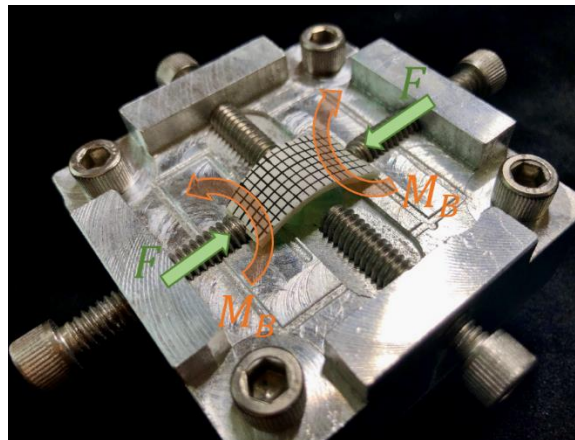
Figure 37 - Sample replica fixation practice

As it is seen in Figure 37, a 2 mm thick paper sheet installed on the fixture is bent by the compressive forces applied laterally. As a result of this practice, a concern regarding the bending moment applied to the actual samples when they are mounted has emerged. The bending moment induces sample deformation toward increasing curvature.
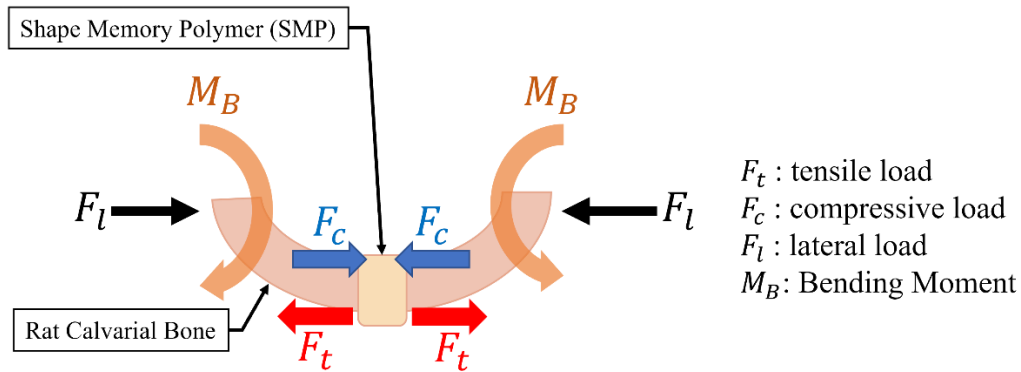
Figure 38 - Bending moment, tensile and compressive load produced by applied lateral load

The purpose of this research is to measure and analyze the shear strength of the osteogenic graft-bone contact. However, if a bending moment occurs, it generates tensile and compressive loads to the interfacial area. To be more precise, in Figure 38, the bottom portion of the SMP is subjected to tensile load, whereas the top portion is subjected to compressive load. Given the applied load conditions, the shear strength of the bottom part along the circumferential seam may differ from the shear strength of the top part of the SMP, as the bone tissues generated in the circumferential area of the bottom part are stretched, while the tissues around the top part of the SMP are compressed.

As a consequence of the practice of sample fixation with the first prototype, sample fixation methods using lateral compression load need either (1) a technique for applying appropriate load alone to fix the sample without imparting significant bending moment, or (2) a modification in the method the sample is fixed.
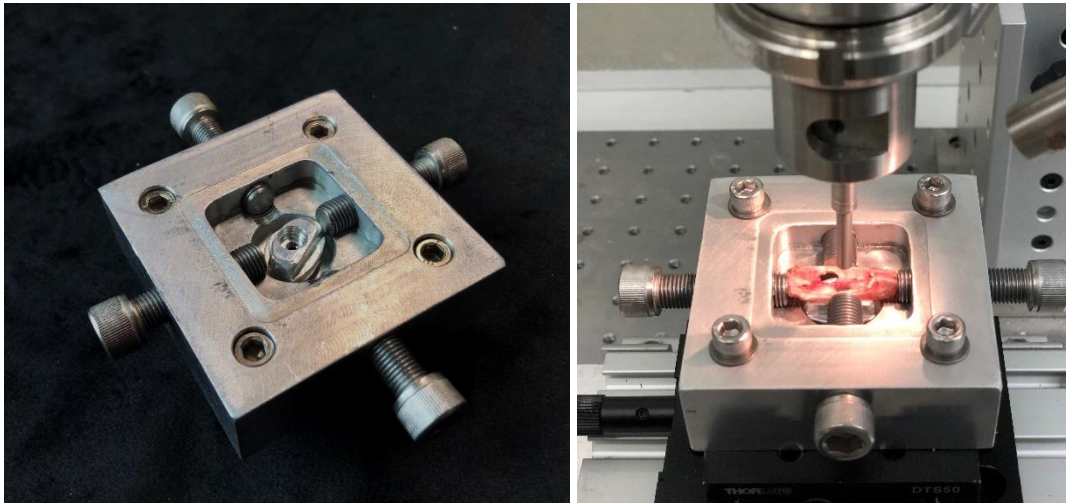
Figure 39 - The second prototype has a sample stand at the center

Following that, a second prototype is created to determine the feasibility of adding sample support to the lateral compressive typed sample fixture, as is seen in Figure 39. A small elliptical component having a blind hole with a 7 mm diameter is located at the center of the fixture base. The purpose of the component is to support the rat's calvarial bone not to bend significantly and be damaged by the compressive lateral load and bending moment. Figure 40 illustrates a schematic diagram of sample fixation using the second prototype fixture. The initial

idea was to turn the sample upside down and use the sample supporter to induce reaction forces (F_s) to cancel out the bending moment (M_B).
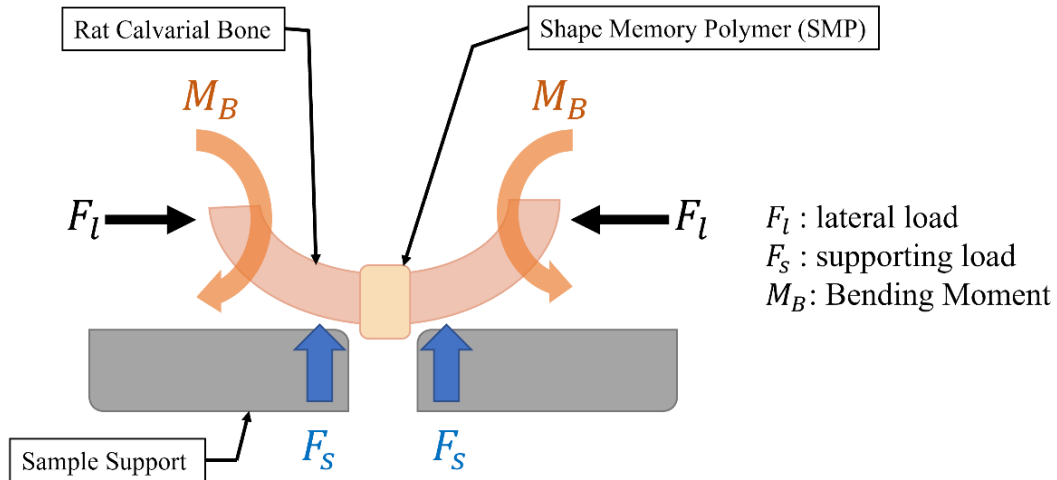
Figure 40 - Sample fixation with sample supports

Additionally, as seen in Figure 41, two separate types of support, denoted by the letters A and B, were developed. The type A support is suitable for unilaterally defected rat calvarial bone samples, while the type B support is suited for bilaterally defected samples. Despite these efforts, the practicality of the components did not significantly aid in the avoidance of undesired bending moment effects on samples. Due to the slippery nature of the tissue, the sample is forced away from the fixture at some point during the bending process.
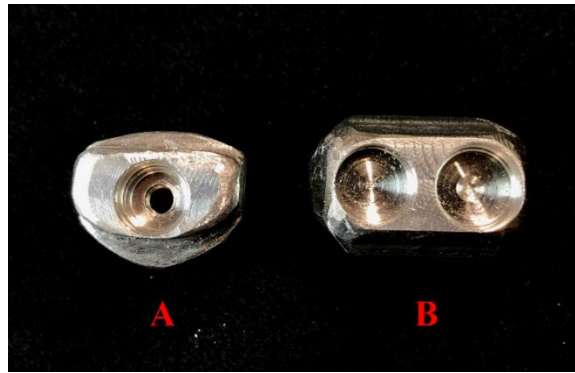
Figure 41 - Supports for samples with unilateral defect (left) and bilateral defect (right)

As a result of the two prototypes, the following design criteria for the final product need to be considered.

(1) Lateral compressive fixation results in a bending force, which may result in sample damage during the fixing process. Other than lateral compressive fixation, a sample fixing technique must be used.

(2) Considering bilateral defects, a new sample fixture shall be capable of damage-free sample fixation without causing harm to a defect other than the testing location.

(3) The new design needs to consider the clearance between the sample support hole's diameter and the defect diameter not to interrupt the push-out indenter.

(4) Ease of axial alignment between the indenter and the sample defect hole shall be considered not to damage the sample while push-out testing.
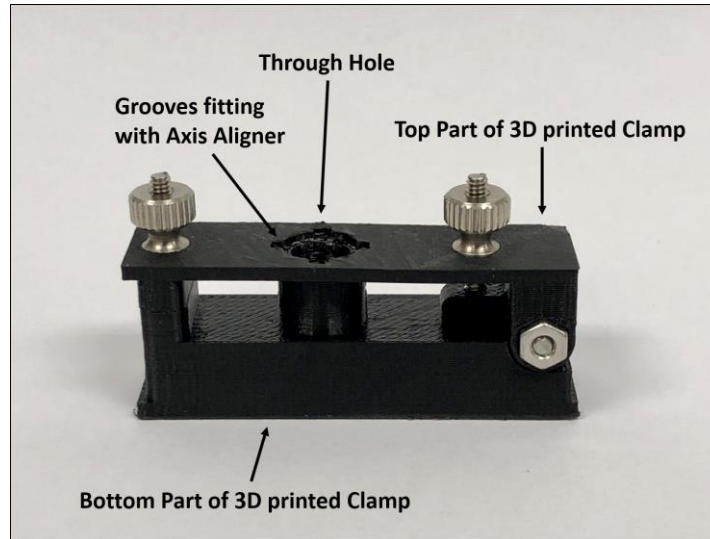
Figure 42 - Sample fixture (vertical clamp type, final design)

Using the developed design requirements as a guide, the final test apparatus, as shown in Figure 42, was designed to play a critical role in the push-out test by precisely fixing a rat calvarial bone specimen without damage while maintaining a specific clearance between the size of the defect and the size of the test apparatus surrounding the defect. Four major aspects are considered to underline the innovations included in the final design. (1) the vertical clamping approach; (2) the capacity to fix and test samples with bilateral defects; (3) the axial alignment of the sample, fixture, and test machine; and (4) the high accuracy with which the sample is positioned. The next sections will cover the primary design features in-depth, as seen in Figure 43.
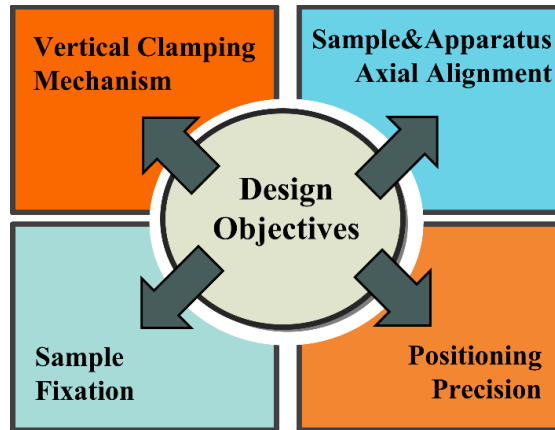
Figure 43 - Design criteria considered in designing final test apparatus

3.3.4.1. Vertical clamping mechanism for sample fixation

F_v : Vertical Load
M_B: Bending Moment
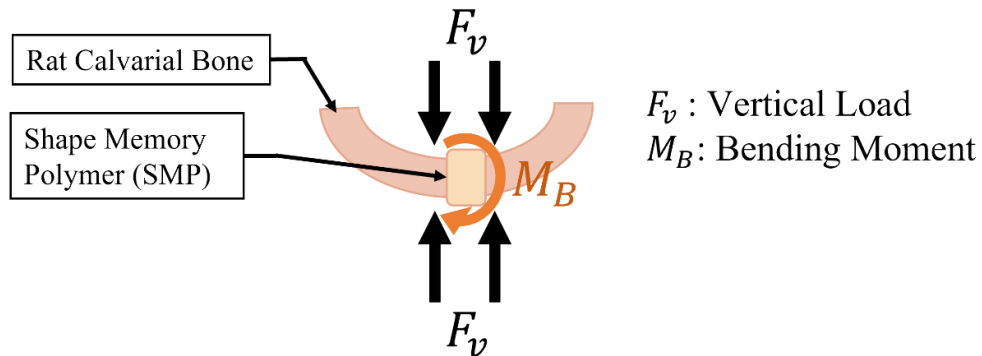
Figure 44 - Vertical clamping mechanism

To begin, in an account of the drawbacks associated with lateral compressive fixation, a new sample fixture was designed using a vertical clamping mechanism. The primary disadvantage of the lateral compressive fixation technique was the bending moment and sample

deformation caused by applied lateral loads, which might result in sample damage and incorrect strength measurements. When considering the bending moment, the length of the moment arm governs the magnitude of the bending moment when the applied forces are the same. This implies that the closer the contact point at which forces are applied, the less the resultant bending moment. For instance, in Figure 45, the bending moment (M_B) is dictated by the length of the moment arm (R_1, R_2) in each case. Assuming that the geometry of the sample is the same, the moment arm connecting the center of SMP to the lateral load (R_1) is often longer than the moment arm connecting the center of SMP to the vertical load (R_2). As a result, when the vertical clamping mechanism is used to secure the sample, there is a reduced likelihood of sample damage due to sample bending and distortion.
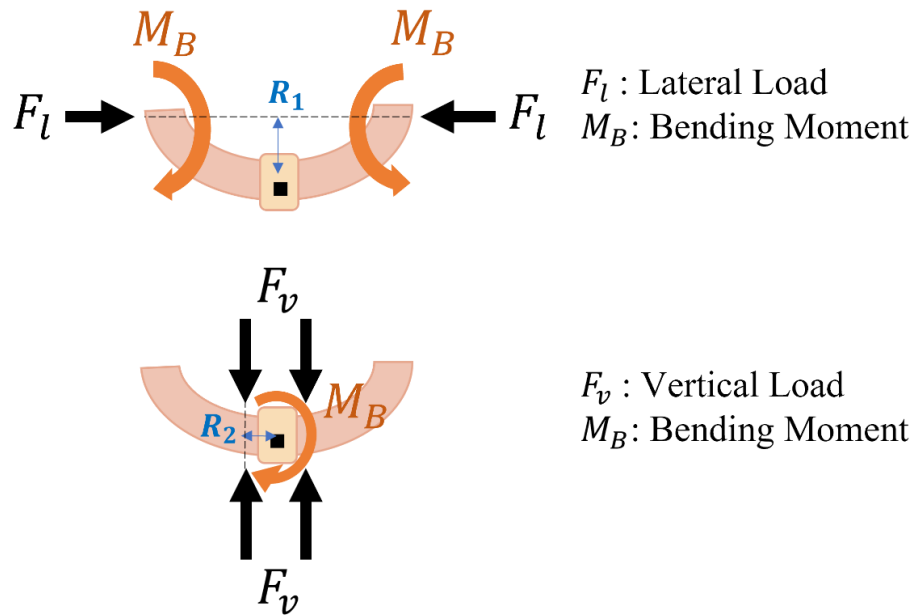
Figure 45 - Moment arms (R_1, R_2) and Bending Moment

Figure 46 - Six degrees of freedom and its decomposition

In addition to the sample preservation advantages of vertical clamping, the vertical clamping technique provides superior stability in sample fixation by restricting the motions of an object. In terms of 'Degrees of Freedom (DoF),' there are three rotating motions (pitch, yaw, and roll, which correspond to the x, y, and z axes, respectively) and three translational movements. (i.e., serge, sway, and heave axes).
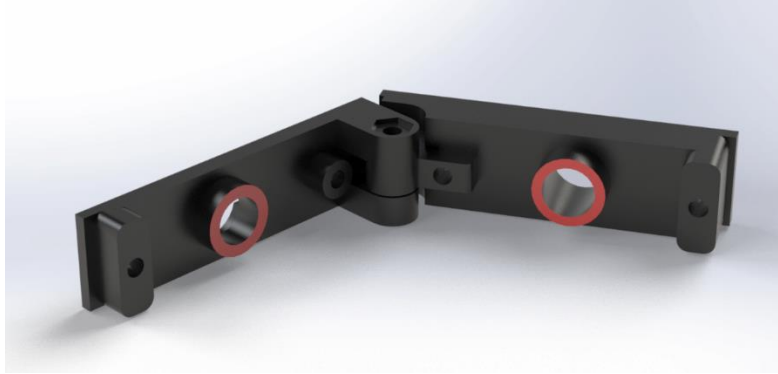
Figure 47 - Sample fixture (open status) having circular planar contact area (red)

Because the newly developed vertical clamp features a circular planar region that contacts the tissue to impart compressive load, it is possible to regulate motions along the x and y axes. The limited motions in Figure 46 are roll, pitch, serge, and sway. Additionally, the heave movement is also controlled since the fixture clamps the tissue's top and bottom surfaces. For these reasons, only yaw movement is permitted, and it is not anticipated to impact the operation of the push-out indenter working in the z-direction.
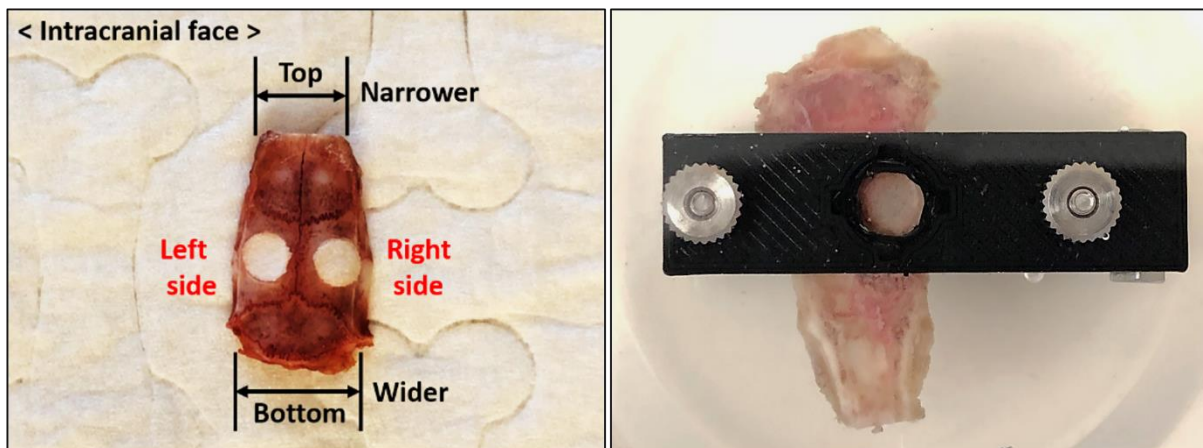
Figure 48 - Rat calvarial bone with bilateral defects (left) and clamped specimen (right)

As explained previously, the vertical clamping technique is quite effective at securing objects in place. Given the stability of the sample fixation, the primary benefit of the vertical clamp is 'isolation of the testing location.' As it is seen in Figure 48, by encircling the defect of interest with the cylinder body, the vertical clamp is capable of selectively isolating the test region. Push-out testing on tiny specimens such as rat calvarial bone with bilateral defects became simpler to execute as a result of this capability. Additionally, the isolation of the area of interest enables the preservation of the opposite side of defects that have not been tested.

3.3.4.3. Push-out Indenter and clearance

Figure 49 - Push-out indenter with 5 mm diameter (flat-bottomed)

A stainless-steel flat-bottomed push-out indenter with a diameter of 5 mm is produced to fit the size of the defect hole. In terms of diameter, one of the critical aspects to consider while

developing the specimen fixture was the clearance between the indenter diameter, the fixture through-hole, and the defect in the specimen. The diameter of the through-hole in the sample fixture was determined using the 'Dhert et al.' [34] approach. which specifies a minimum clearance of approximately 1.4~1.5 mm (including the tolerance induced by the 3D printer's filament size while printing) between the defect diameter and the through-hole to reduce the influence of the sample fixture on the interfacial stress distribution. [35]
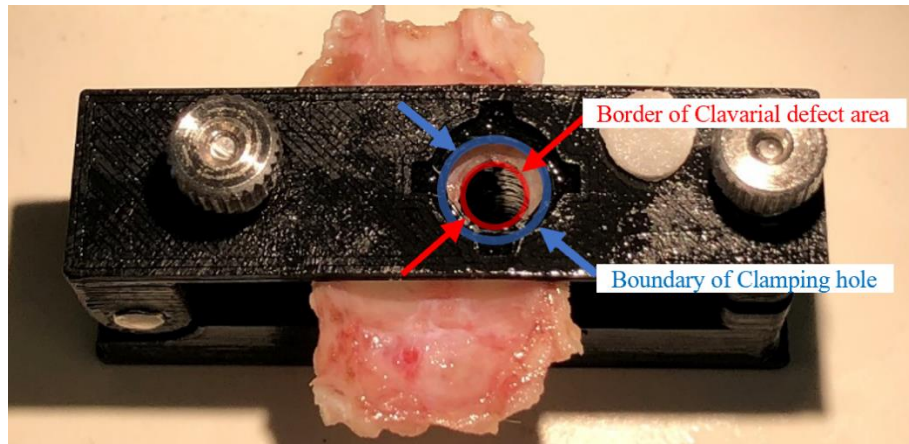
Figure 50 - By putting the spotlight through the hole, the defect's border (5 mm nominal diameter) is confirmed to be inside the boundary of the through-hole (6.4~6.5 mm).

3.3.4.4. System alignments

3.3.4.4.1. Alignment between sample and sample fixture

One characteristic that differentiates the new sample fixture from the preceding apparatus is that the fixture can be removed from the stage and put directly on the sample. To be more explicit, the test equipment utilized in earlier studies (i.e., 'Lohmann, P., et al. (2017)' [32] and

'Kwon, J., et al. (2019)'[33]) are installed to the platform, and the sample must be placed and aligned on the fixture. However, the fixture invented in this research is distinct from the platform, allowing the user to easily attach the fixture onto the sample and center the defect hole and through-hole of the fixture using their eyes.

3.3.4.4.2. Alignment between sample fixture and testing machine

Accurate alignment of the sample fixture, as well as the direction of the push-out indenter, was a difficult design aspect to accomplish. Previously published research did not specify the technique of alignment or accuracy. To achieve precise axial alignment between the fixture and indenter during operation, attaching a strong point lighting device, such as laser pointers, to the linear actuator was first contemplated. However, the issue was with the laser's focus performance. Cheap lasers scatter light quite widely, and it is impossible to tell if laser attached push-out indenter is adequately lined up with the fixture.

In addition to lighting devices, a mechanism was invented for matching a unique physical pattern between the fixture and a small device called a 'Position aligner,' as illustrated in Figure 15-(A), connected to the push-out rod.
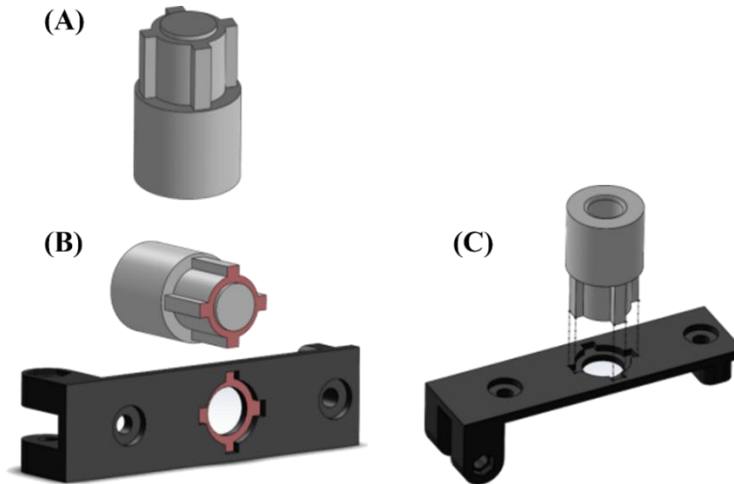
Figure 51 - (A) Position aligner, (B) Unique cruciate pattern, (C) Axial alignment using pattern

As seen in Figure 51-(B), the distinctive cruciate pattern (red-colored planes) is placed to the top surface of the sample fixture (black-colored component) and the body of the position aligner (gray-colored component). Figure 51 –(C) depicts how both sections cooperate to align themselves by matching their distinctive patterns.

To demonstrate the functioning in an actual testing situation, Figure 52 shows the sample fixture holding a rat calvarial bone and the position aligner connected to the push-out rod.
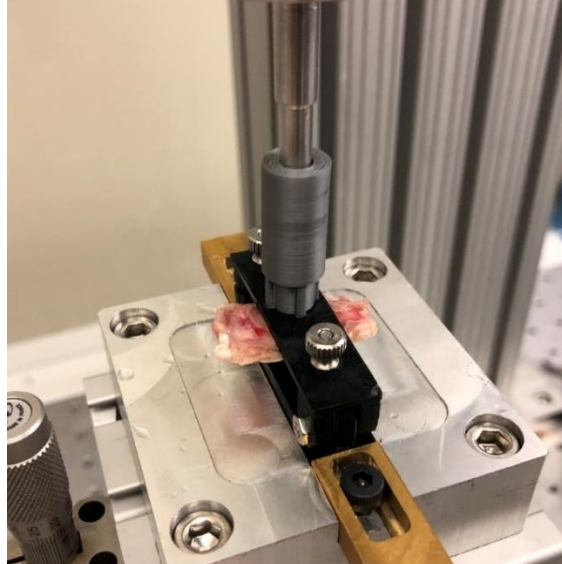
Figure 52 - Position aligner and sample fixture in operation

3.3.4.5. Precise positioning of sample fixture

A linear stage (XYZ Linear Stage ULTRAlign, 13mm Travel, Crossed-Roller, M4, M6, Newport) is used as part of the test equipment addition to the sample fixture, purposeful positioning of the entire test fixture to obtain exact axial alignment in XYZ directions. The micrometer (Vernier Micrometer, 13 mm Travel, Newport) that is combined with the linear stage is a defining characteristic of the stage, as seen in Figure 53. With a sensitivity of 1.0 μm, the micrometer allows the experimenter to place samples accurately.
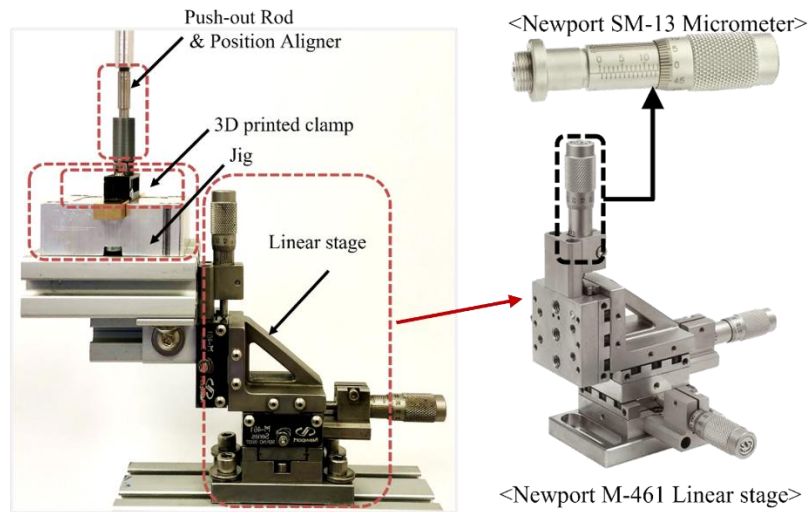
Figure 53 - XYZ linear stage and assembled micrometers (manufactured by Newport)

3.3.4.6. Summary
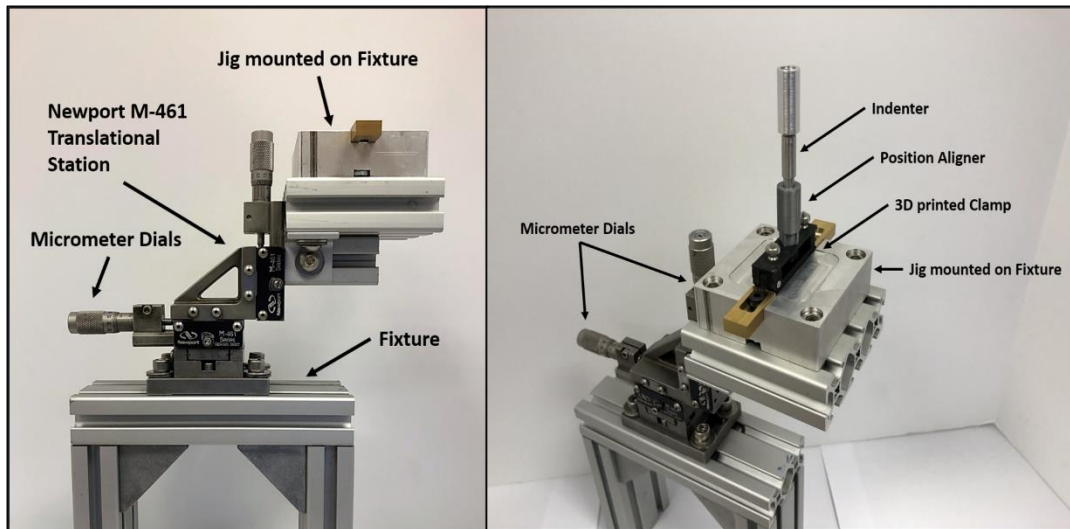
Figure 54 - Fully assembled push-out test apparatus

The design work herein includes reviews regarding the push-out test apparatus used in the other research, two types of prototypes made based on the design requirements extracted from the review, and the final design was invented through the lessons from the prototypes.

As it is seen in Figure 54, the test apparatus is composed of three major parts (1) Push-out indenter with position aligner, (2) Vertical sample clamp, and (3) High precision XYZ linear stage). By utilizing the advanced test apparatus, the push-out test will be executed to evaluate the performance of a novel self-fitting SMP scaffold compared to the clinical gold standard in the next section.
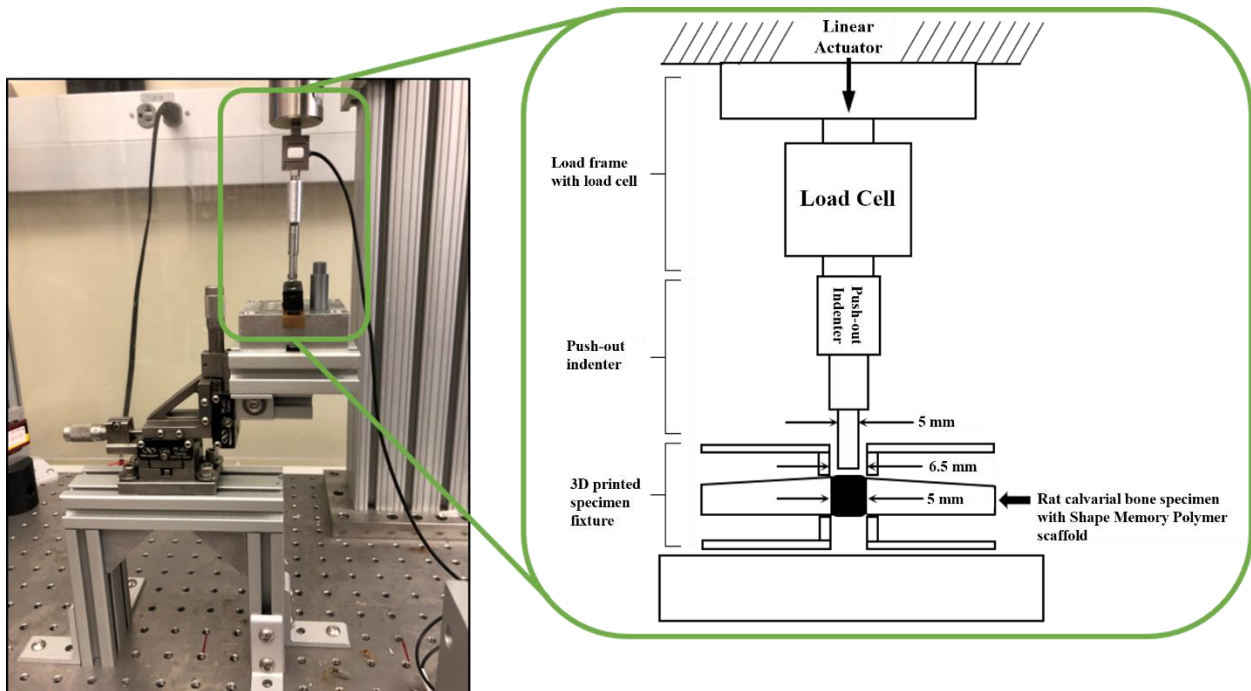
Figure 55 - Push-out test apparatus with testing machine (left) and schematic diagram of the full test apparatus in action

3.4. Test results

Given the push-out test results, average max load and standard deviation were acquired

from each group, as is seen in the following table and figure.

Test Group	Average Max Load (N)	Stdev (s)	Sample # (n)
Bone Flap (Autologous Graft)	111.061	50.270	11
SMP (Uncoated, No Cells)	174.969	57.201	12
SMP (Coated, No Cells)	171.410	40.638	12
SMP (Uncoated, with Cells)	171.111	58.167	12
SMP (Coated, with Cells)	146.380	43.269	12

Table 4 – Push-out test results
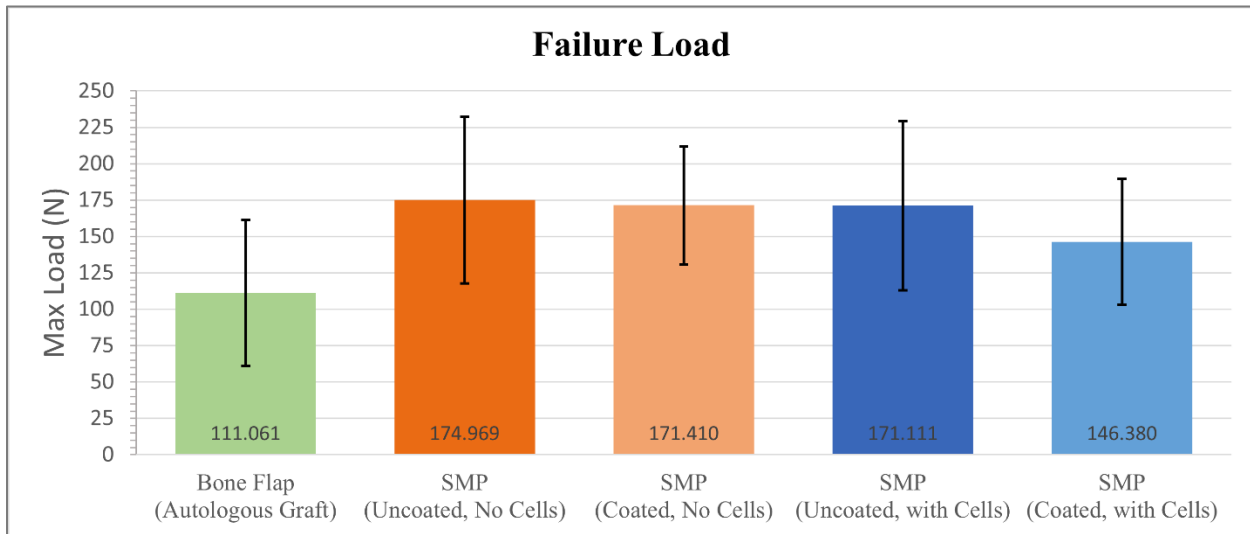
Figure 56 - Push-out test results in a bar plot

95

P-values were evaluated to determine if the null hypothesis is rejected for each group (i.e., A particular type of treated SMP has no significant difference from the clinical gold standard or Bone flap.). The 'Independent Two-sample t-test' was used since the test groups are independent, and one of them (bone-flap) has a different sample size (11). The steps below demonstrate how to compute the t-scores.

To estimate the overall standard deviation, the equation below is used.

$$S^2 = \frac{\left((n_A - 1)S_A^2 + (n_B - 1)S_B^2\right)}{n_A + n_B - 2}$$

Where, n_A is group A's sample number, n_B is group B's sample number, and S_A, S_B are the standard deviation of groups A and B, respectively.

Then, the following equestion to find the t-score is utilized.

$$t = \frac{m_A - m_B}{\sqrt{\frac{S^2}{n_A} + \frac{S^2}{n_B}}} = \frac{difference\ of\ group\ average}{standard\ error\ of\ difference}$$

As a result, the t-score for each case is as follows.

t-score	Uncoated, no cell	Coated, no cell	Uncoated, with cells	Coated, with cells
Bone Flap	-2.835	-3.179	-2.637	-1.811
Uncoated, no cell		0.181	0.168	1.423
Coated, no cell			0.015	1.493
Uncoated, with cells				1.218
Coated, with cells				

Table 5 - t-score results

Given the t-scores, the P-value is as follows.

P-value	Uncoated, no cell	Coated, no cell	Uncoated, with cells	Coated, with cells
Bone Flap	**0.016**	**0.008**	**0.023**	0.097
Uncoated, no cell		0.859	0.870	0.183
Coated, no cell			0.988	0.164
Uncoated, with cells				0.249
Coated, with cells				

Table 6 - P-values between each group

The group treated with bone flaps (the clinical gold standard) had the lowest average failure load. And the bone flap group was significantly lower than Uncoated+no cell group (p=0.016 < 0.05), Coated+no cell group (p=0.008 < 0.05), Uncoated+with cell group (p=0.023 < 0.05). Interestingly, there was no statistically significant difference between the bone flap and Coated+with cell groups.

3.5. Conclusion

Innovative push-out testing equipment for small animal models has been created for the purpose of assessing novel medical devices that aid in the recovery of calvarial defects. The following aspects set this innovative test device apart from those utilized in earlier investigations.

(1) Vertical clamping approach to reduce the bending moment around the circumferential region of the testing area

(2) Capability of conducting bilateral defects tests on small samples

(3) Accurate alignment technique minimizes sample damage caused by contact with the osteogenesis region during test operation.

To assess the design's efficacy, the novel self-fitting Shape Memory Polymers were studied (N=60) and found to have slightly better mechanical performances to the clinical gold standard (i.e., Autologous graft, Bone flap).

CHAPTER IV

EVALUATE THE BIOMECHANICS OF OSSEOUS PROJECTILE IMPACTS ON

SKELETAL BONE

4.1. Introduction

In 1977, a research team from Washington State University unearthed a single male

mastodon (*Mammut americanum*) from sediments at the Manis site in Washington by Carl

Gustafson.[36] The rib bone was radiocarbon dated and dated back to roughly 13,800 years ago;

nevertheless, the oldest human presence in North America is estimated to have begun around

13,000 years ago. In addition, computed tomography (CT) images revealed the existence of

foreign osseous objects embedded in the rib and artificially shaped to a point. entering the rib's

approximately 2 mm thick cortical bone, the foreign item penetrated the rib 2.15 cm and

fragmented.[37] Furthermore, no evidence of bone regrowth was found at the site, suggesting that

the mastodon died soon after the projectile struck.[12]

Furthermore, the Clovis stone projectile point is the only well-known ancient weapon

used to hunt megafauna in North America. These stone points, discovered in mammoth and

mastodon bones, were used between 13,050 and 12,750 calibrated years ago.[38][39] Stone

projectile points from before Clovis have been unearthed in North American locations, although

none of them have been linked to megafaunal bones.[39] In contrast, death or scavenging sites of

pre-Clovis megafauna have been discovered without accompanying projectile points. A bone

projectile point fragment discovered buried in a mastodon rib at the Manis site in Washington

state demonstrates that megafaunas (e.g., mastodon) were hunted with osseous points in the

Pacific Northwest 13,800 years ago, about 800 years before Clovis.

Dr. Moreno's research group, or BMEL, constructed an 'Air cannon' projectile impact test instrument to determine if the osseous point embedded in the Manis mastodon rib bone was created by human activity prior to the Clovis age. The procedures for designing and standardizing impact events will be presented in this paper. Furthermore, research questions that are described in the next section may be addressed with this equipment.

4.2. Research questions and objectives

According to one hypothesis, the Manis mastodon specimen was formed as a consequence of a human-accelerated projectile impacting the megafauna. Given this, the following research question can be developed.

- *Do osseous projectiles accelerated by human-generated kinetic energy and colliding with bone and/or bone simulants match the fracture and penetration patterns seen in the Manis mastodon rib model?*

To address the question, the following aspects are necessary to be developed and investigated.

(1) What types of projectile were used at the time of the impact?

(2) How many forces and velocity human can produce with projectiles that are similar to that of the Manis mastodon model having a particular range of mass?

(3) What types of target bone are similar to the mastodon rib bone?

(4) How to standardize the impact testing that is replicating human thrown projectile?

To expand on the preceding section, the projectile was most likely slowed by soft tissue before reaching a bone area with a thin cortical shell (2 mm) and penetrating around 2cm into the cancellous (trabecular) bone. The projectile tip lodged in the rib bone of the mastodon was not of the Clovis projectile type[40], and the type of point and gear employed are unknown.

Based on the given conditions, the objectives that we are trying to achieve are:

- Experimentally replicate the dynamic environment of osseous projectiles impacting mastodon skeletal anatomy.

- Assess the likelihood of the Manis mastodon specimen having been produced by human hunting activity

- Investigate the likelihood of the Manis mastodon specimen having been produced by alternative theories.

4.3. Experimental design

The following experimental design factors are examined while designing, constructing, and performing tests to simulate the dynamic environment of bony point projectiles during impact onto the osseous target.

(1) Conduct research to determine the dynamic criteria of a human-thrown projectile, which may be used to define a plan for replication on the experimental design.

(2) Develop test equipment capable of standardizing dynamic environments of projectiles accelerated to human throwing velocity.

(3) Produce projectiles that are equivalent to the geometric properties of the projectile tip contained in the Manis model or the form of well-known alternatives discovered in the period around the Manis model.

(4) Define target environmental conditions that are comparable to those seen in living megafauna (i.e., elephant and mastodon).

(5) Execute projectile impact test and investigate the effects and dynamic properties of bone/bone impact.

(6) Evaluate the test findings and compare them to the Manis mastodon model.

4.3.1. Measuring dynamic properties of projectile accelerated to human throwing speed

4.3.1.1. Atlatl hunting dart-throwing experiment

One of the uncertainties in replicating the impact event that occurred about 13,800 years ago is the absence of knowledge and direct evidence on the sort of weapon used to hunt the mastodon. The shattered projectile tip stuck in the mastodon rib fossil does not instruct the whole weapon system to select and use specific shaped points. As a result, it was assumed that "***pre-Clovis humans utilized a principal weapon system linked with the New World Clovis culture in North America during the Paleoindian period (12,000 – 10,000 BC)***." [41] Clovis points are narrow fluted projectile points created utilizing the bifacial percussion flaking process. They have been discovered in high concentrations but are only found in North America.[41][42]
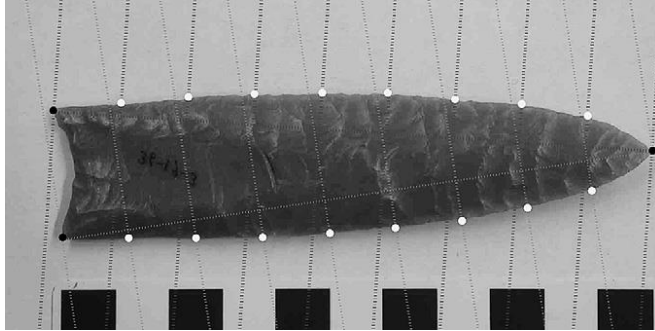
Figure 57 - Clovis point[41]

Given this, Dr. Michael Waters 'Center for the Study of the First Americans' research group and Dr. Michael Moreno's BMEL in Texas A&M University's Anthropology department made and threw atlatl hunting darts with Clovis tips, and measured the velocity of a human-thrown projectile, as shown in Figure 57.
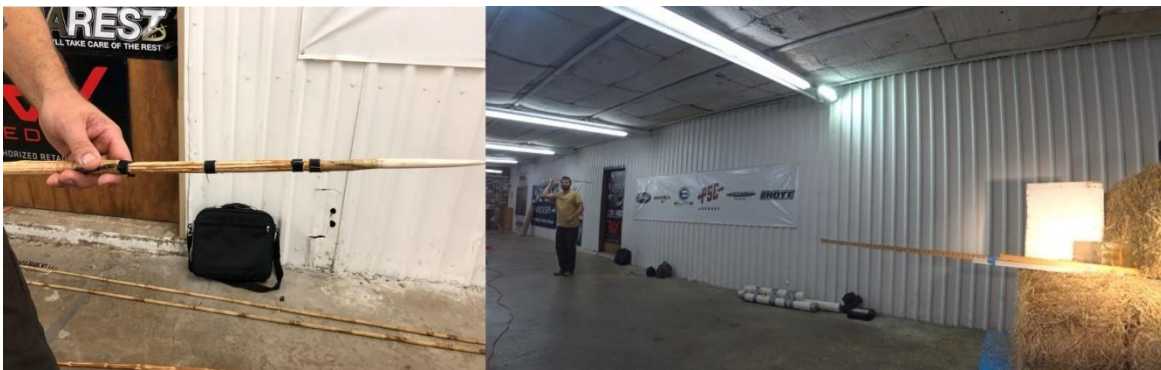
Figure 58 - Atlatl dart with the Clovis point (left), Throwing a dart at archery (right)

Three atlatl darts of varying weights were used in the atlatl velocity measurement study: 272g, 321g, and 393g. The kinetic energy and linear momentum are computed from the

measured velocity using the following equations, and the results are reported in Table 4 below. The next section contains a more extensive description of the method to assess projectile velocity.

(1) Kinetic Energy [K.E., joules] = ½ × mass × (velocity)^2

(2) Linear Momentum [p, kg m/s] = mass × velocity

Atlatl Mass	Category	Maximum	Minimum	Average	Std Dev (σ)
272 g	Velocity (m/s)	22.494	18.683	20.6	1.447
	Kinetic Energy (joules)	68.81	47.47	57.96	8.092
	Linear Momentum (kg m/s)	6.12	5.08	5.6	0.393
321g	Velocity (m/s)	22.791	17.258	20.203	1.309
	Kinetic Energy (joules)	83.37	47.8	66.64	8.350
	Linear Momentum (kg m/s)	7.32	5.54	6.53	0.420
393g	Velocity (m/s)	21.726	15.44	18.78	1.450
	Kinetic Energy (joules)	92.75	44.09	68.21	10.896
	Linear Momentum (kg m/s)	8.54	5.89	7.29	0.589
Overall	**Velocity (m/s)**	**22.791**	**15.44**	**19.861**	*
	Kinetic Energy (joules)	**92.75**	**44.09**	**64.27**	
	Linear Momentum (kg m/s)	**8.54**	**5.08**	**6.473**	

Table 7 - Velocity, Kinetic Energy, and Momentum data obtained from human thrown projectiles

4.3.1.2. Velocity measurement method (we invented)

To provide a better knowledge of measuring the projectile's velocity, the projectile's trajectory was captured using a 'Phantom Ultrahigh-speed camera v5.2'. Following that, each frame of video footage was extracted and saved as a JPEG file.

Figure 59 - Phantom Ultrahigh-speed camera v5.2

<JPEG file extraction>

<Phantom Camera Control (PCC) software>

Figure 60 - Image file extraction from Highspeed video footage

105

As shown in Figure 60, The displacement (annotated as 'l') between two consecutive frames ('shot A' and 'shot B') was determined using a series of continuous images and an opensource image processing program (or 'ImageJ') developed by the National Institutes of Health (NIH). Due to the fact that the frame rate is a user-defined camera parameter, the average velocity of the projectile between two successive images was computed by multiplying the obtained displacement by the frame rate. For example, if the camera was set as 2200 fps (frame per second) and the displacement between the consecutive images (i.e., l in Figure 60) is 2 cm, the average velocity over the two shots is 44 meter/second (= 0.02 m × 2200 frame/second).
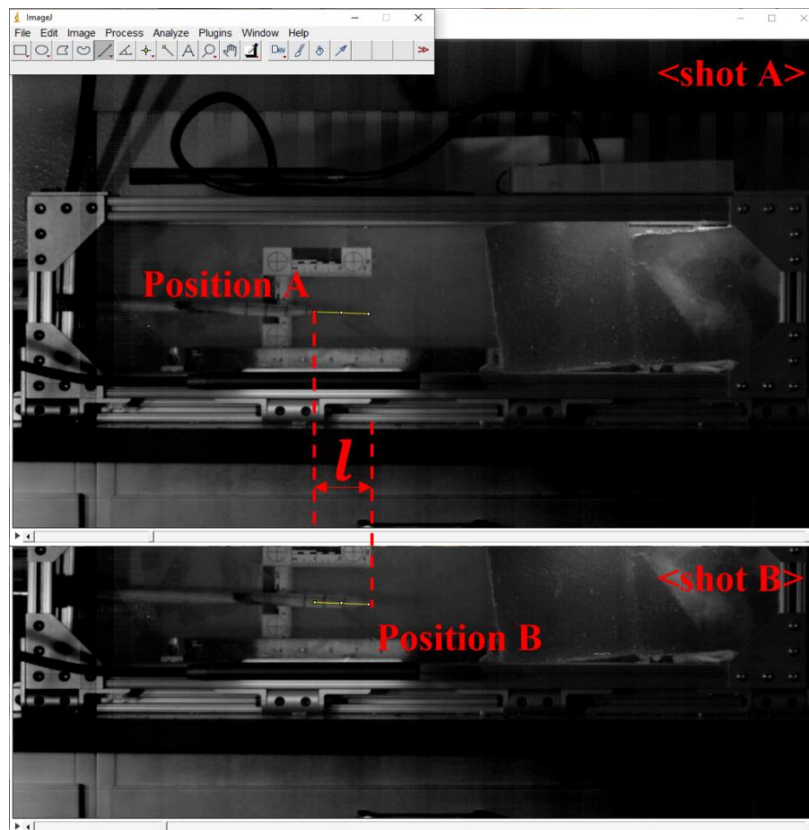
Figure 61 - Displacement measurement with ImageJ software
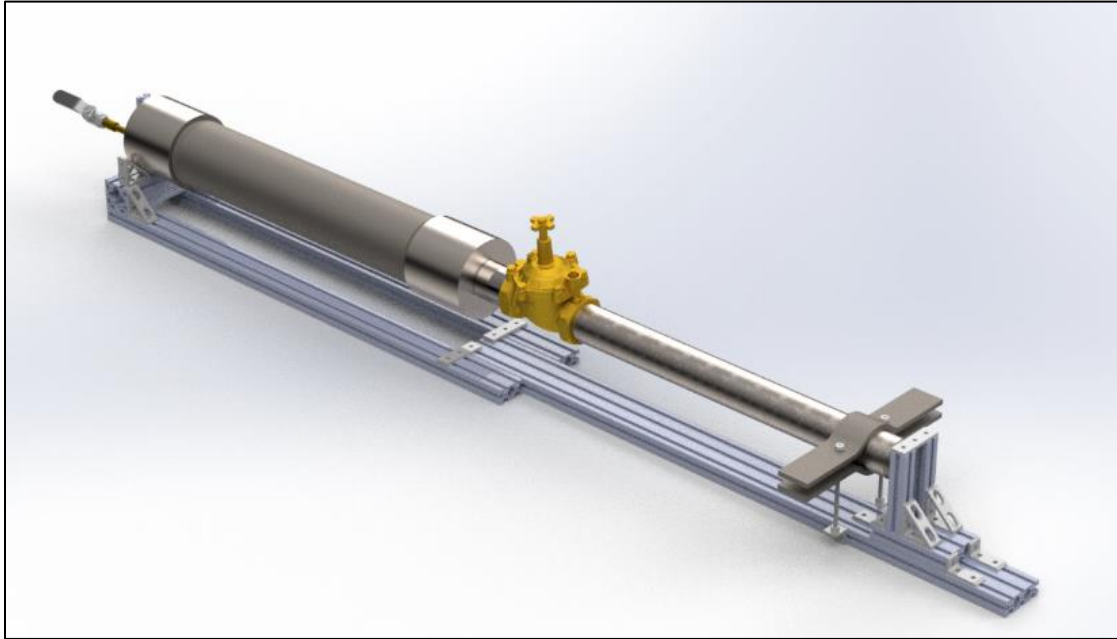
Figure 62 – Air cannon of the projectile impact test apparatus

Alumni of BMEL created the air cannon for the projectile impact test machine (Shannon Ingram, Zachary Lawson, and Andrew Robbins). The cannon's chamber holds compressed air and is prepared to release the pressure to the piston mounted in the barrel. The flow control valve (the gold-colored component in Figure 61) is equipped with a solenoid valve and a switch. When the chamber reaches the desired air pressure, the operator activates the switch, which opens the solenoid valve, driving the piston and imparting propelling forces to the projectile loaded on the air cannon.

107

Iterative design effort has been conducted to create a complex structure capable of (1) enclosing and securing the sample in situ and (2) protecting the experimenter from flying sample fragments caused by impact forces. All the following fixtures are a part of the whole projectile impact test apparatus and will be connected to the air cannon.
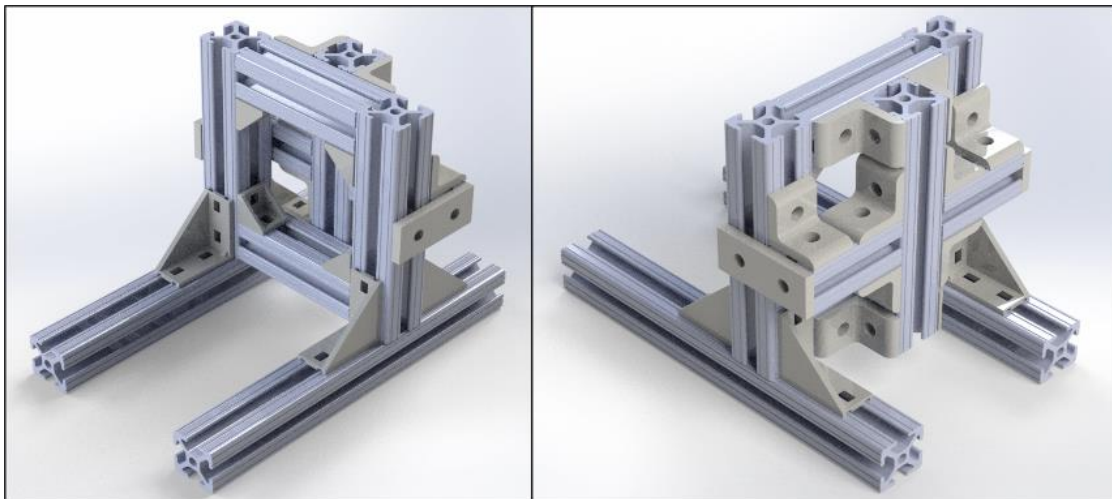
Figure 63 – The first attempt at designing sample fixture

To begin, a sample fixture, as shown in Figure 62, was built to secure the sample in place. To support and bear the impact forces delivered by the propelled projectile, the cruciate structure was joined to the rectangular aluminum extrusion frame. However, there was no provision for covering the mounted sample in order to screen out pieces during sample dispersion.
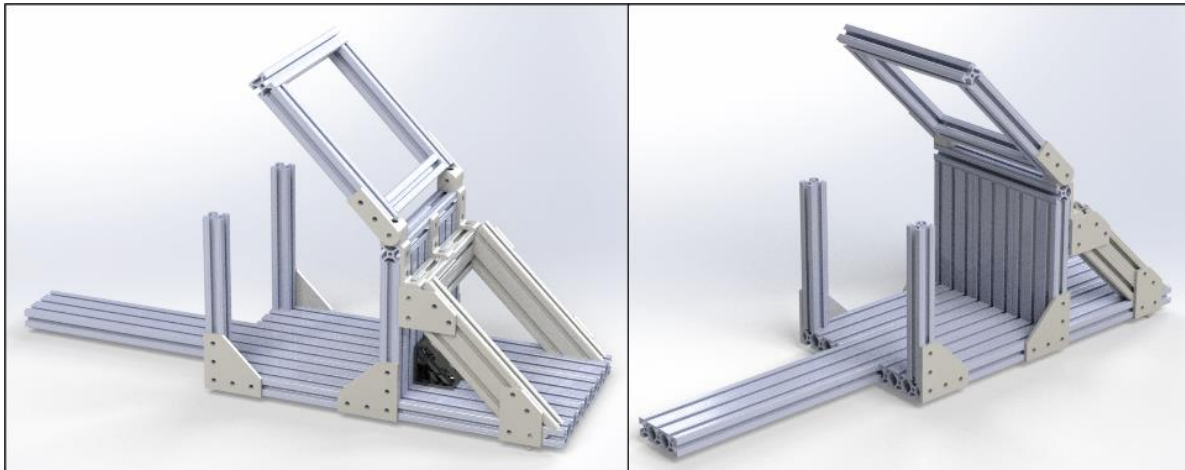
Figure 64 – The second attempt at designing sample fixture

As a result of the design feedback, as seen in Figure 63, a small chamber enclosing the space and capable of containing samples was created. A hinged door was suggested for ease of installation of samples on the fixture. Despite the advancement, the restricted space confronted the user's need for more capacity to accommodate future huge specimens.
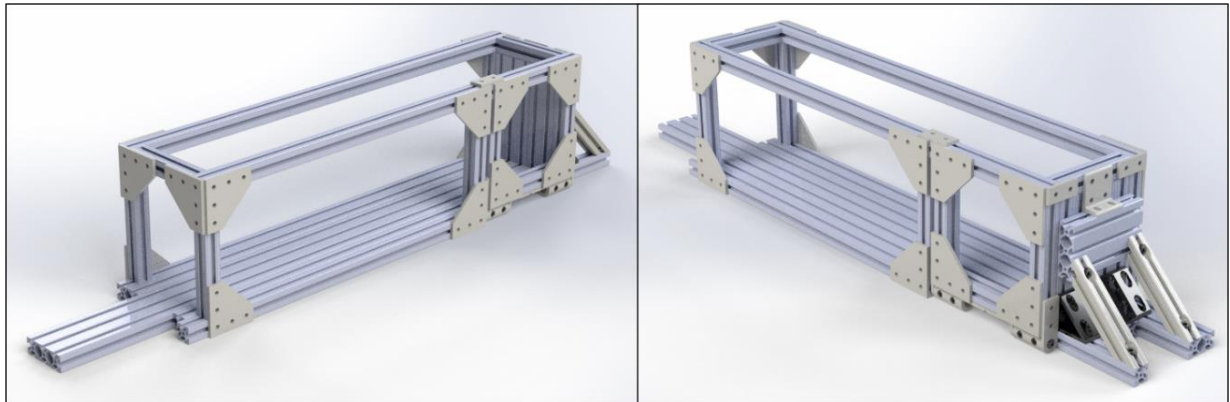
Figure 65 - The third attempt of sample fixture

The third design effort, out of four, was quite similar to the final design, except for the size of the hinged front door and the back support's competency. As seen in Figure 64, the space for sample fixation has been increased in comparison to the prior design.
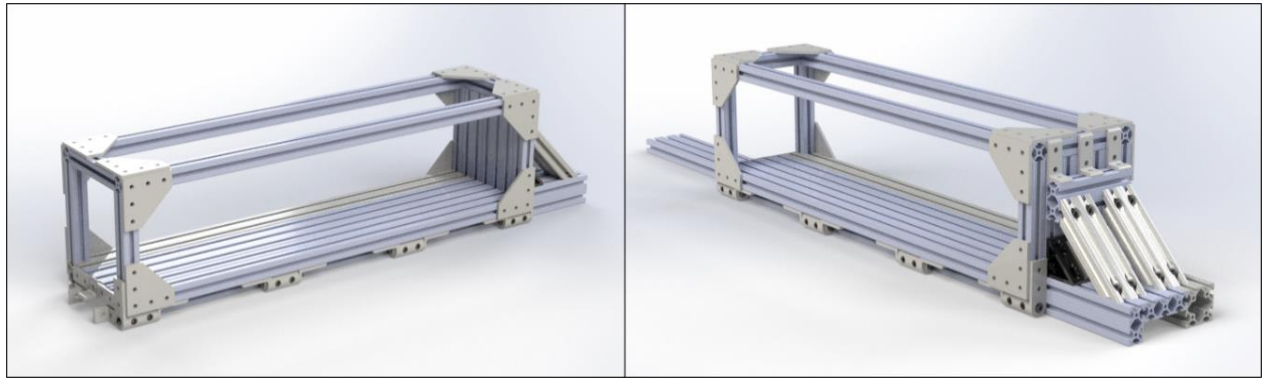
Figure 66 – The final design of 'Safety Cabinet' for the projectile impact test

Consequently, the final design, named the 'Safety Cabinet,' satisfied the design objectives for (1) sample fixation and (2) enhanced safety measures to safeguard the experimenter. The 'Safety Cabinet's distinguishing features include (1) the adaptability of the sample fixation method used with the aluminum extrusion platform, (2) the front hinged door that serves as both a sample fixation method and a means of isolating the test site protected by transparent polycarbonate windows, and (3) a sturdy back support capable of withstanding high impact forces from an accelerated projectile.

Figure 67 - Fully assembled projectile impact test apparatus

The whole appearance of the projectile impact test device is seen in Figure 66. A specially designed 'Safety Cabinet' is fitted to the air cannon to offer sample fixation and an additional layer of safety.

4.3.2.4. Correlation between projectile mass, air chamber pressure, and kinetic energy

Correlations between projectile mass, air chamber pressure, and kinetic energy were examined prior to conducting the actual projectile impact test. This is because by comprehending the correlations, we can determine the air chamber pressure required to create a certain velocity, kinetic energy, and linear momentum associated with the desired mass.

Three components comprise the connection we want (i.e., projectile mass, air chamber pressure, kinetic energy). As a result, multiple regression is required to estimate and predict the intended values of a variable. The data pool for multiple regression is constructed using four distinct mass values (129.0g, 161.0g, 211.0g, and 288.5g) and five distinct air chamber pressure values (10psi, 15psi, 20psi, 30psi, and 40psi). By following the velocity measurement procedure stated in section 4.3.1.2., the maximum velocity of the projectile was investigated for each case, and the computed velocity data were employed to derive the kinetic energy of the projectile. As seen in the image below, the following data points were acquired.
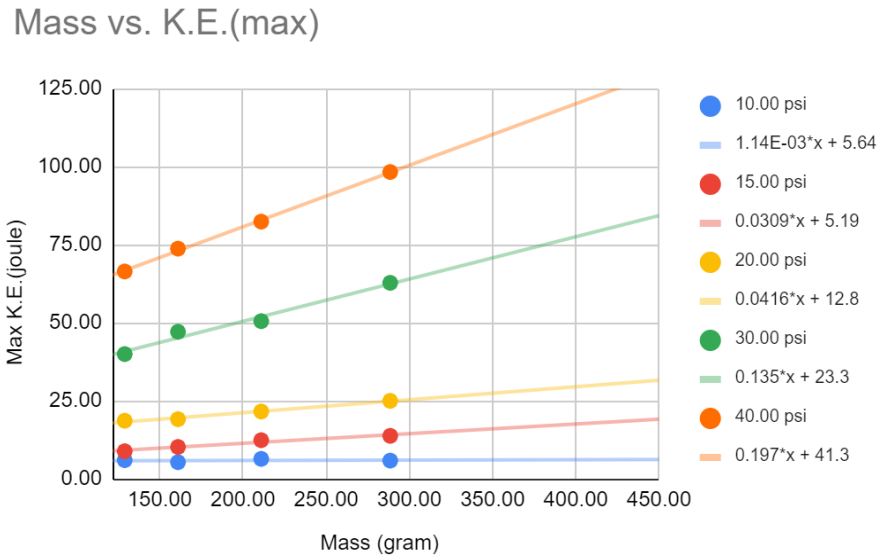
Figure 68 - Mass vs. Maximum K.E. with five different air chamber pressure

For further information, multiple regression is performed with the data sets using Python - 'Scikit-learn' library, which is one of the popular open-source data analysis libraries. At the actual testing date, the regression findings will be used to determine the required air chamber pressure to produce specific kinetic energy depending on the total projectile mass.

4.3.3. Sample preparation

4.3.3.1. Projectile

As it was briefly stated in section 4.3.1.1., the projectile points were shaped in Clovis point style by the assumption that "***pre-Clovis humans utilized a principal weapon system linked with the New World Clovis culture in North America during the Paleoindian period (12,000 – 10,000 BC)*** ." In addition to the style of projectile point, in terms of material, Bovine cortical bone was selected and utilized since the embedded point in the Manis mastodon model is

made of compact bone. Since the material of fragments of the point in the Manis mastodon model has been estimated as foreign mastodon compact bone[40], the best option should be using the mastodon's cortical bone. However, the species are extinguished already, and the descents of the megafauna, or elephant, are endangered species, so it is really limited to select the best options. Given this, the 'Cattle' was selected for the following reasons.

(1) A relatively large mammal that may acquire bone formations comparable to mastodon bone in order to support its considerable weight.

(2) One of the most prevalent species that is not endangered

(3) The same dietary needs of herbivores are identical to those of mastodon.[43]

The Animal Science department at Texas A&M University features a nationally recognized program in meat science. The school offers integrated education in the processing of meat animals. Using College Station, TX resources, a bovine tibia, and femur was obtained from the meat science department, as shown in Figure 68, and the shaft of the bones was cut into various pieces along with the longitudinal direction with the assistance of the local butcher business 'Readfield Meats & Deli'.

Figure 69 - Bovine tibia (left top) linked with the femur (right bottom), acquired from Meat science department in Texas A&M University

Using a band saw and belt sander, 'Zachary Newell' of the Anthropology department at Texas A&M University grinds the cut cortical bone of the shaft into the form of a Clovis point. Following that, the projectile points were hafted with pine poles in a manner similar to that utilized by the Paleoindians (i.e., resin-bonded and knotted with animal sinew product) by 'Zachary Newell and Nicholas Bentley' at the Anthropology department at Texas A&M University.

Figure 70 - Hafted bony projectile tip (Clovis point type)

The hafted projectiles have been kept in a plastic container in a dry, shaded place at room temperature. Additional projectile information, such as mass and length, will be detailed in the test parameter article in the section on test execution.

4.3.3.2. Target

As seen in Figure 70, the lengthy shaft of the fractured projectile tip extends from the outside to the inside of the mastodon rib bone. To determine the angle of incidence and penetration depth, an open-source program called 'ImageJ' was used. Due to the damaged region around the embedded point, it was difficult to determine the incidence angle and penetration depth accurately. Given the constraint, a straight line linking two points in an undamaged region was drawn, as was an extra straight line across the projectile shaft's center. The penetration depth and incidence angle were estimated using the two straight lines and the cross point, yielding 44.80 degrees and 19.43 millimeters, respectively.

117

In addition, the cortical bone thickness around the impact point was measured as 2 millimeters by using the method used to measure the penetration angle and depth.
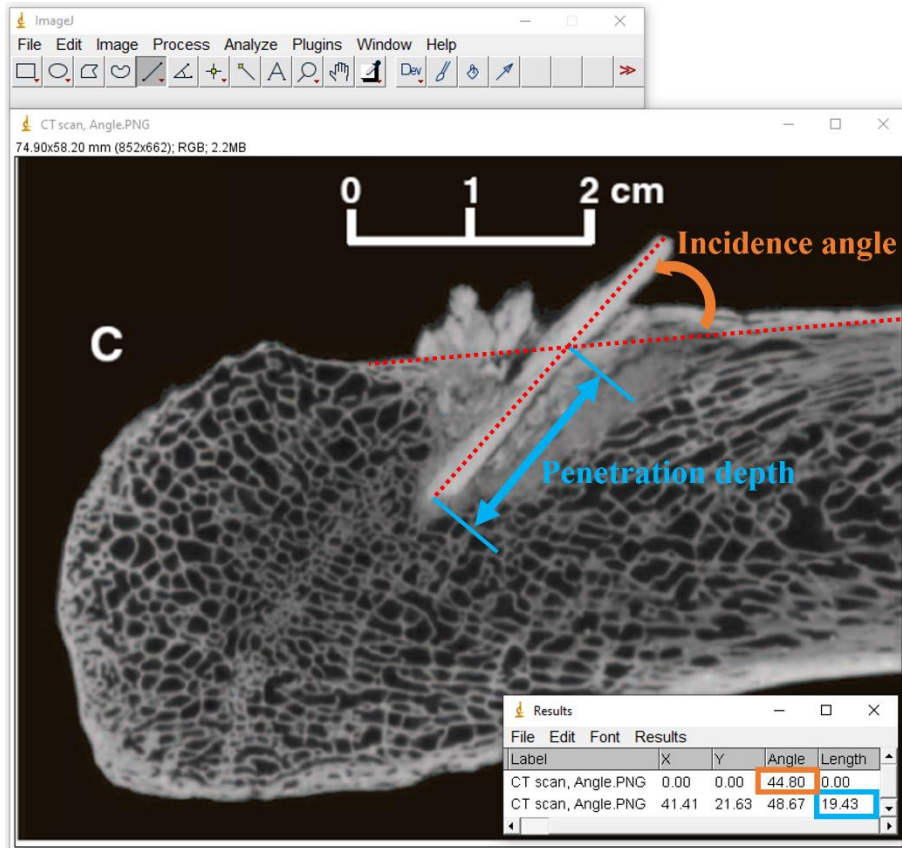
Figure 71 – CT scan image: Manis mastodon rib bone containing foreign bone projectile tip[40]

Based on the data collected, the following experimental design aspects for the target sample can be established.

(1) The angle of penetration of the projectile tip should be about 44.80 degrees.

(2) The presence and thickness of cortical bone or a simulant should be taken into account.

118

(3) At the study's end, the penetration depth should be assessed and compared to the depth estimated from the CT scan image.

4.3.3.2.1. Types of the target specimen

Initially, the target bone was thought to be the bovine rib bone. However, the small quantity of cancellous bone relative to the volume of rib bone and the thick cortical bone prompted us to identify a distinct bone part with a significant percentage of cancellous bone and a thin cortical bone. In light of our collaborator's availability (i.e., the Meach science department at Texas A&M University), the Bovine Humerus bone was chosen and procured for the purpose of preparing the target samples.

While constructing the target, the cortical bone thickness of bovine humerus bone remained approximately 8 mm, four times the thickness of the Manis mastodon model. As a result, we chose to remove the cortical bone and expose the cancellous bone surface that faces the projectile tip upon impact. This is because if a projectile tip fracture occurs without the presence of 2mm of cortical bone, there is a significant probability of obtaining the projectile fractures with the cortical bone.

4.3.3.2.2. 45 degrees angled target fixture

To install target bones with angles comparable to those of the Manis mastodon model, a 3D printed part capable of holding the sample was designed to be 45 degrees from the horizontal

119

surface and printed with PLLA using a 3D printer. The treated bovine humerus head was then

bolted to the 3D printed sample fixture, as seen in Figure 71.
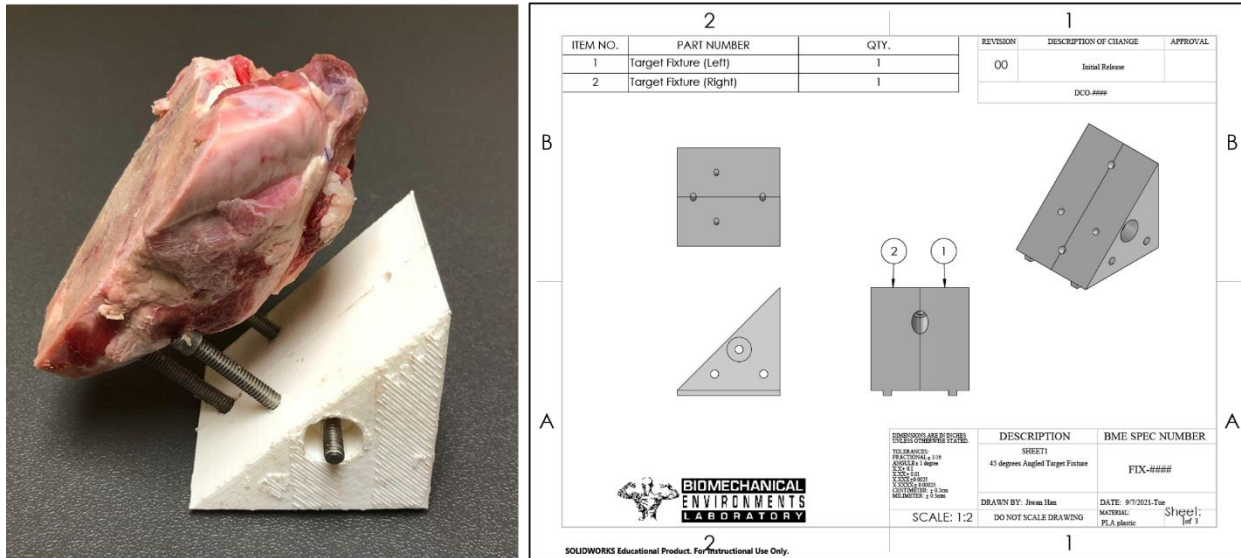
Figure 72 - Bovine humerus bone fixed on 3D printed fixture (left), drawings of the sample fixture (right)

4.3.3.3. Presence of soft tissue

According to 'Eren, M. I. et al. (2021)' [44] and 'Huckell et al. (1979)' [45], the average hide

thickness of contemporary megafauna (i.e., Indian elephant) was 25~28 mm. Furthermore, as

mentioned in 'Waters et al. (2011),' The thickness of the epaxial muscle of ancient megafauna

was estimated to be 250–300 mm[12]. As a consequence, the thickness of soft tissue (muscle,

ligament, hide, and skin) of mastodon is predicted to be between 275 and 328 mm.

Ballistic gelatin blocks (a combination of 80% tap water and 20% ballistic gelatin powder,

or 250 BL Type A Ordnance Gelatine, manufactured by GELITA© Gelatine) were constructed

and utilized for projectile impact testing to mimic the characteristics of living soft tissues estimated in prehistoric megafauna.[46][47]

4.4. Test Execution

4.4.1. Test protocol

A deliberate test method is necessary to prevent accidents and to ensure that critical resources are prepared for inclusion in actual testing. To ensure the validity of the plans for performing projectile impact testing, a comprehensive description of the test methods was written. Due to the fact that the test procedure includes even small details, the document's volume exceeds the limits of this section. In response, the appendix contains the test procedures with accompanying explanations.

4.4.2. Specimen information

Nine projectile points (Bovine tibia and femur, Clovis type, hafted) and 18 ballistic gelatin blocks (9 blocks with gelatin only and nine blocks containing bovine humerus bone target and fixture) are utilized for the projectile impact testing.

The measured total mass for each specimen is as follows.

Sample Group by weight	Projectile	Mass (g)		
		Projectile	Added scale mass	Final mass
Group 1	Projectile A	268.0	0.0	**268.0**
	Projectile B	269.0	0.0	**269.0**
	Projectile D	272.0	0.0	**272.0**
	Projectile E	268.5	0.0	**268.5**
	Projectile G	270.5	0.0	**270.5**
	Projectile H	272.0	0.0	**272.0**
				270(±1%)g
Group 2	Projectile C	270.0	135.0	**405.0**
	Projectile F	270.0	135.0	**405.0**
	Projectile I	267.5	131.5	**399.0**
				403(±1%)g

Table 8 - Measured projectile mass

4.4.3. Test parameters

According to Table 4, the maximum kinetic energy that humans can generate to propel spearlike projectiles is between 44.09 and 92.75 joules, with an average of 64.27 joules. With this kinetic energy range in consideration, three distinct experimental groups with 65 joules, 90 joules, and 45-joule kinetic energy were established, as it is shown in the following table.

Projectile	Total mass (g)	Target maximum K.E. (joule)	Estimated air chamber pressure (psi)
Projectile A	268.0	65 (Medium)	**32.6**
Projectile B	269.0		**32.5**

Projectile C	405.0		28.4
Projectile D	272.0	90 (High)	41.8
Projectile E	268.5		41.9
Projectile F	405.0		37.8
Projectile G	270.5	45 (Low)	25.0
Projectile H	272.0		25.0
Projectile I	399.0		21.1

Table 9 - Estimated air chamber pressure based on multiple regression

As previously indicated in Section 4.3.2.4, a multiple regression model was developed using data collected during experiments with various mass groups and air chamber pressures. Table 6 illustrates how the model generated the 'Estimated air chamber pressure' by employing three distinct kinetic energy groups and a range of projectiles of variable mass.

Using the 'Estimated air chamber pressure,' the next sections will conduct and analyze actual osseous projectile impact tests onto a 45 degree inclined bony target.

4.5. Test Results

The Ultrahigh-speed video footage was analyzed to evaluate the maximum velocity, kinetic energy, and linear momentum of the projectiles specified in Tables 8 and 9, as it is shown in the table below.

Sample	Measured Projectile total mass (g)	Maximum		
		Velocity (m/s)	K.E. (joules)	Linear Momentum (kg m/s)
Projectile A	268.0	**23.428**	**73.549**	**6.279**
Projectile B	269.0	**22.968**	**70.953**	**6.178**
Projectile C	405.0	**18.448**	**68.915**	**7.471**
Projectile D	272.0	**28.272**	**108.705**	**7.690**
Projectile E	268.5	**28.171**	**106.542**	**7.564**
Projectile F	405.0	**23.042**	**107.510**	**9.332**
Projectile G	270.5	**18.452**	**46.050**	**4.991**
Projectile H	272.0	**18.374**	**45.915**	**4.998**
Projectile I	399.0	**14.366**	**41.173**	**5.732**

Table 10 - Projectile impact test results
(Maximum velocity, kinetic energy, and linear momentum)

Additionally, the penetration depth was determined by calculating the mean value of the longest (l_A) and shortest (l_B) depths, as seen in Figure 73. Because the bone projectile hit the target at an angle of around 45 degrees, an average was evaluated.
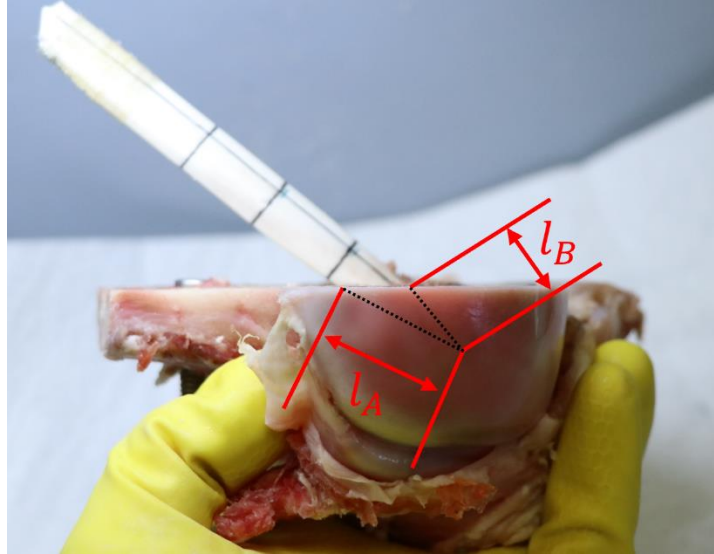
Figure 73 - Penetration depth measurement

As a consequence of the investigation, the following penetration depth value was determined. Penetrations did not occur for the set of targets with the low average kinetic energy (i.e., 44.379 joules).

Sample	Average of measured K.E.	**Gelatin penetration length**	Target bone		
			Longest measured depth (l_A)	Shorted measured depth (l_B)	**Evaluated penetration depth $(l_A + l_B)/2$**
Projectile A		**190.6 mm**	6 mm	3 mm	**4.5 mm**
Projectile B	71.139 J	**185.0 mm**	7 mm	3 mm	**5 mm**
Projectile C		**187.2 mm**	3 mm	2 mm	**2.5 mm**
Projectile D	107.585 J	**192.2 mm**	24 mm	15 mm	**19.5 mm**
Projectile E		**183.8 mm**	26 mm	17 mm	**21.5 mm**

Projectile F		**184.2 mm**	19 mm	11 mm	**15 mm**
Projectile G		**132.2 mm**			
Projectile H	44.379 J	**131.0 mm**		No penetration occurred	
Projectile I		**127.87 mm**			

In addition, the impact angle was measured for each projectile impact test. The measured values are indicated in the table below.

Sample	Impact angle (degree)
Projectile A	47.52˚
Projectile B	43.94˚
Projectile C	56.27˚
Projectile D	38.52˚
Projectile E	45.26˚
Projectile F	45.51˚
Projectile G	
Projectile H	No impact occurred
Projectile I	

Table 11 - Projectile impact angle

According to the early stages of this study's research design, the projectiles were predicted to be shattered. However, none of the projectiles developed fractures and were completely undamaged.

126

Medium K.E. group	Sample	Measured Projectile mass (g)	Measured K.E. (joules)	Penetration depth (mm)	Impact angle (degree)
	Projectile A	268.0	**73.5**	4.5	47.52˚
	Projectile B	269.0	**71.0**	5.0	43.94˚

High K.E. group	Sample	Measured Projectile mass (g)	Measured K.E. (joules)	Penetration depth (mm)	Impact angle (degree)
	Projectile D	272.0	**108.705**	19.5	38.52˚
	Projectile E	268.5	**106.542**	21.5	45.26˚

Low K.E. group	Sample	Measured Projectile mass (g)	Measured K.E. (joules)	Penetration depth (mm)	Impact angle (degree)
	Projectile G	270.5	**46.050**	No impact occurred	
	Projectile H	272.0	**45.915**		

Heavy projectile group	Sample	Measured Projectile mass (g)	Measured K.E. (joules)	Penetration depth (mm)	Impact angle (degree)
Medium K.E.	Projectile C	**405.0**	68.915	2.5	56.27˚
High K.E.	Projectile F	**405.0**	107.510	15.0	45.51˚
Low K.E.	Projectile I	**399.0**	41.173	No impact occurred	

Table 12 - Overal test results

4.6. Discussion

In Section 4.3.3.2, the CT image of the Manis mastodon model was examined, revealing a penetration angle and depth of 44.80 degrees and 19.43 mm, respectively. To simulate an impact event, the impact testing apparatus was used to conduct osseous projectile impact tests on a bony target. As a result of the testing, the average impact angle was determined to be 46.17 degrees with a standard variation of 5.81 degrees. In terms of penetration depth, a test group with

127

an average projectile mass of 270.25 grams and average kinetic energy of 107.62 joules demonstrated an average penetration depth of 20.5 mm.

By comparison to the human-thrown atlatl dart data in Table 7, 107.62 joules is somewhat more than the maximum kinetic energy (= 92.75 joules) generated by an experimenter (i.e., 'Ryan Gill'). The penetrating depth, however, was 20.5 mm, marginally greater than the Manis mastodon model (i.e., 19.43 mm).

4.7. Conclusion

As a consequence, the research question posed at the beginning of this study:

• *Do osseous projectiles accelerated by human-generated kinetic energy and colliding with bone and/or bone simulants match the fracture and penetration patterns seen in the Manis mastodon rib model?*

was addressed, as bone penetration patterns found in Manis mastodon rib bone may be formed using human-generated kinetic energy.

REFERENCES

[1] Olszta, M. J., Cheng, X., Jee, S. S., Kumar, R., Kim, Y. Y., Kaufman, M. J., ... & Gower, L. B. (2007). Bone structure and formation: A new perspective. Materials Science and Engineering: R: Reports, 58(3-5), 77-116.

[2] Wang, X., Xu, S., Zhou, S., Xu, W., Leary, M., Choong, P., ... & Xie, Y. M. (2016). Topological design and additive manufacturing of porous metals for bone scaffolds and orthopaedic implants: A review. Biomaterials, 83, 127-141.

[3] Fishero, B., Kohli, N., Das, A., Christophel, J., & Cui, Q. (2015). Current concepts of bone tissue engineering for craniofacial bone defect repair. Craniomaxillofacial trauma & reconstruction, 8(1), 23-30.

[4] van de Vijfeijken, S. E., Münker, T. J., Spijker, R., Karssemakers, L. H., Vandertop, W. P., Becking, A. G., ... & Zaat, S. A. J. (2018). Autologous bone is inferior to alloplastic cranioplasties: safety of autograft and allograft materials for cranioplasties, a systematic review. World neurosurgery, 117, 443-452.

[5] De Nardo, L., De Cicco, S., Jovenitti, M., Tanzi, M. C., & Fare, S. (2006, January). Shape memory polymer porous structures for mini-invasive surgical procedures. In Engineering Systems Design and Analysis (Vol. 42495, pp. 539-544).

[6] Taljanovic, M. S., Jones, M. D., Ruth, J. T., Benjamin, J. B., Sheppard, J. E., & Hunter, T. B. (2003). Fracture fixation. Radiographics, 23(6), 1569-1590.

[7] Einhorn, T. A., & Gerstenfeld, L. C. (2015). Fracture healing: mechanisms and interventions. Nature Reviews Rheumatology, 11(1), 45-54.

[8] Chang, K. P., Lai, C. H., Chang, C. H., Lin, C. L., Lai, C. S., & Lin, S. D. (2010). Free flap options for reconstruction of complicated scalp and calvarial defects: report of a series of cases and literature review. Microsurgery: Official Journal of the International Microsurgical Society and the European Federation of Societies for Microsurgery, 30(1), 13-18.

[9] Kretlow, J. D.; Young, S.; Klouda, L.; Wong, M.; Mikos, A. G., Injectable biomaterials for regenerating complex craniofacial tissues. Adv. Mater. 2009, 21, 3368- 3393.

[10] J.D. Erndt-Marino, D. J. M.-P., S. Samavedi, A.C. Jimenez-Vergara, P. DiazRodriguez, L.Woodard, D. Zhang, M.A. Grunlan, M.S. Hahn, Evaluation of the osteoinductive capacity of polydopamine-coated poly(ε-caprolactone) diacrylate shape memory foams. ACS Biomater. Sci. & Eng. 2015, 1, 1220-1230.

[11] Pfau, M. R., Beltran, F. O., Woodard, L. N., Dobson, L. K., Gasson, S. B., Robbins, A. B., ... & Grunlan, M. A. (2021). Evaluation of a self-fitting, shape memory polymer scaffold in a rabbit calvarial defect model. Acta biomaterialia, 136, 233-242.

[12] Waters, M. R., Stafford, T. W., McDonald, H. G., Gustafson, C., Rasmussen, M., Cappellini, E., ... & Willerslev, E. (2011). Pre-Clovis mastodon hunting 13,800 years ago at the Manis site, Washington. Science, 334(6054), 351-353.

[13] https://www.universalgripco.com/utm-introduction

[14] Davis, J. R. (Ed.). (2004). Tensile testing. ASM international.

[15] Swartz, E. E., Floyd, R. T., & Cendoma, M. (2005). Cervical spine functional anatomy and the biomechanics of injury due to compressive loading. Journal of athletic training, 40(3), 155.

[16] Betina, B. (2018). Intervertebral movement analysis of the cervical spine.

[17] Stankovic, J. A., & Rajkumar, R. (2004). Real-time operating systems. Real-Time Systems, 28(2-3), 237-253.

[18] Forstner, P. (1999). FIFO architecture, functions, and applications. Texas Instruments Incorporated, Tech. Rep.

[19] NI LabView Forum: Using Formula Nodes in LabVIEW: (https://knowledge.ni.com/KnowledgeArticleDetails?id=kA03q000000x30HCAQ&l=en-US)

[20] McKinley, S., & Levine, M. (1998). Cubic spline interpolation. College of the Redwoods, 45(1), 1049-1060.

[21] Zimmermann, G., & Moghaddam, A. (2011). Allograft bone matrix versus synthetic bone graft substitutes. Injury, 42, S16-S21.

[22] Wang, W., & Yeung, K. W. (2017). Bone grafts and biomaterials substitutes for bone defect repair: A review. Bioactive materials, 2(4), 224-247.

[23] Grant, G. A., Jolley, M., Ellenbogen, R. G., Roberts, T. S., Gruss, J. R., & Loeser, J. D. (2004). Failure of autologous bone—assisted cranioplasty following decompressive craniectomy in children and adolescents. Journal of Neurosurgery: Pediatrics, 100(2), 163-168.

[24] Lawson, W., & Biller, H. F. (1982). Bone Graft Techniques. Otolaryngology--Head and Neck Surgery, 90(5), 589-594.

[25] Pfau, M. R., Beltran, F. O., Woodard, L. N., Dobson, L. K., Gasson, S. B., Robbins, A. B.,
    ... & Grunlan, M. A. (2021). Evaluation of a self-fitting, shape memory polymer scaffold
    in a rabbit calvarial defect model. Acta biomaterialia, 136, 233-242.

[26] Zhang, D., George, O. J., Petersen, K. M., Jimenez-Vergara, A. C., Hahn, M. S., & Grunlan,
    M. A. (2014). A bioactive "self-fitting" shape memory polymer scaffold with potential to
    treat cranio-maxillo facial bone defects. Acta biomaterialia, 10(11), 4597-4605.

[27] Zhang, D., Petersen, K. M., & Grunlan, M. A. (2013). Inorganic–organic shape memory
    polymer (SMP) foams with highly tunable properties. ACS applied materials &
    interfaces, 5(1), 186-191.

[28] Ryu, J., Ku, S. H., Lee, H., & Park, C. B. (2010). Mussel-inspired polydopamine coating as
    a universal route to hydroxyapatite crystallization. Advanced Functional Materials,
    20(13), 2132-2139.

[29] Ku, S. H., Ryu, J., Hong, S. K., Lee, H., & Park, C. B. (2010). General functionalization
    route for cell adhesion on non-wetting surfaces. Biomaterials, 31(9), 2535-2541.

[30] Whang, K., Thomas, C. H., Healy, K. E., & Nuber, G. (1995). A novel method to fabricate
    bioabsorbable scaffolds. Polymer, 36(4), 837-842.

[31] Pfau, M. R., McKinzey, K. G., Roth, A. A., Graul, L. M., Maitland, D. J., & Grunlan, M. A.
    (2021). Shape memory polymer (SMP) scaffolds with improved self-fitting properties.
    Journal of Materials Chemistry B, 9(18), 3826-3837.

[32] Lohmann, P., Willuweit, A., Neffe, A. T., Geisler, S., Gebauer, T. P., Beer, S., ... & Langen,
    K. J. (2017). Bone regeneration induced by a 3D architectured hydrogel in a rat critical-
    size calvarial defect. Biomaterials, 113, 158-169.

132

[33] Kwon, J., Lee, D. J., Kocher, M., Kim, Y. I., Wu, T. J., Whitley, J., & Ko, C. C. (2019). The inhibition of radial and axial micromovement of bone scaffold with gelfoam® and titanium mesh fixation and its effects on osteointegration. Methods and Protocols, 2(1), 20.

[34] Dhert, W. J. A., Verheyen, C. C. P. M., Braak, L. H., De Wijn, J. R., Klein, C. P. A. T., De Groot, K., & Rozing, P. M. (1992). A finite element analysis of the push-out test: Influence of test conditions. Journal of biomedical materials research, 26(1), 119-130.

[35] Lawson, Z. T., Han, J., Saunders, W. B., Grunlan, M. A., Moreno, M. R., & Robbins, A. B. (2021). Methodology for performing biomechanical push-out tests for evaluating the osseointegration of calvarial defect repair in small animal models. MethodsX, 8, 101541.

[36] Gustafson, C. E., Gilbow, D. W., & Daugherty, R. D. (1979). The Manis mastodon site: early man on the Olympic Peninsula. Canadian Journal of Archaeology/Journal Canadien d'Archéologie, 157-164.

[37] Petersen, K. L., Mehringer, P. J., & Gustafson, C. E. (1983). Late-glacial vegetation and climate at the Manis mastodon site, Olympic Peninsula, Washington. Quaternary Research, 20(2), 215-231.f

[38] Waters, M. R. (1985). Early Man in the New World: An evaluation of the radiocarbon dated Pre-Clovis sites in the Americas. Environments and extinctions: man in late glacial North America, 125-43.

[39] Waters, M. R. (2019). Late Pleistocene exploration and settlement of the Americas by modern humans. Science, 365(6449), eaat5447.

133

[40] Waters, M. R. (2021). 13,900 year-old osseous projectile point from the Manis site, Washington—Pre-Clovis mastodon hunting in the Pacific Northwest. Science Advanced, abo0531

[41] Buchanan, B., & Collard, M. (2010). A geometric morphometrics-based assessment of blade shape differences among Paleoindian projectile point types from western North America. Journal of Archaeological Science, 37(2), 350-359.

[42] Buchanan, B., O'Brien, M. J., & Collard, M. (2014). Continent-wide or region-specific? A geometric morphometrics-based assessment of variation in Clovis point shape. Archaeological and Anthropological Sciences, 6(2), 145-162.

[43] Pérez-Crespo, V. A., Prado, J. L., Alberdi, M. T., Arroyo-Cabrales, J., & Johnson, E. (2016). Diet and habitat for six American Pleistocene proboscidean species using carbon and oxygen stable isotopes. Ameghiniana, 53(1), 39-51.

[44] Eren, M. I., Meltzer, D. J., Story, B., Buchanan, B., Yeager, D., & Bebber, M. R. (2021). On the efficacy of Clovis fluted points for hunting proboscideans. Journal of Archaeological Science: Reports, 39, 103166.

[45] Huckell, B. B. (1979). Of chipped stone tools, elephants, and the Clovis hunters: an experiment. Plains Anthropologist, 24(85), 177-190.

[46] Prather, R. N., Swann, C. L., & Hawkins, C. E. (1977). Backface Signatures of Soft Body Armors and the Associated Trauma Effects. ARMY ARMAMENT RESEARCH AND DEVELOPMENT COMMAND ABERDEEN PROVING GROUND MD CHEMICAL SYSTEMS LAB.

[47] Goode, T. W. (2017). Soft Body Armor Back Face Deformation with Ballistics Gel
Backing.

APPENDIX A

PROJECTILE IMPACT TESTING PROTOCOL:

SPEAR-LIKE BONE PROJECTILE TO 45 DEGREES ANGLED BOVINE HUMERAL HEAD

TARGET

1. Test method

1.1. Purpose – This document describes the specific procedure for spear-like projectile

impact testing to 45 degrees angled bone target. It defines study-specific

parameters for this testing.

1.2. General Information

1.2.1. <u>Safety Requirements</u> – Ensure the use of personal protective equipment (PPE)

upon testing preparation. The equipment includes the following items.

- Safety glasses (eye protection)

- Lab coats (skin and clothing protection)

- Long sleeve pants (leg protection)

- Closed-toe shoes (foot protection)

1.2.2. <u>Estimated Time To Complete (ETC)</u> –

- Total estimated work duration: (Approx.) 10 hr + (# of test) x (15 min/test)

i. Target specimen prep: 6 hr 30 min

ii. Test apparatus set-up: 1 hr 30 min

iii. Specimen installation: 30 min

iv. Test execution: 15 min/test

v. Data acquisition (data saving, photography): 1 hr

vi. Specimen storage: 30 min

1.2.3. <u>Definitions</u> – None

1.2.4. <u>Related Documents/References</u>

 i) SOP-0008: Digital Raw Data Procedures

 ii) FIX-0073 Air Cannon

 iii) FIX-0074 Safety Cabinet of Air Cannon

 iv) FIX-0075 Projectile Tip Mount of Air Cannon

 v) FIX-0076 45 degrees Angled Target fixture

1.2.5. <u>Equipment and Materials</u>

 i) Test apparatus

- Air Cannon (FIX-0073)
- Safety Cabinet (FIX-0074)
- Solenoid valve push-button switch

 ii) Projectile Tip Mount

- Projectile Tip Mount (FIX-0075)
- 2ea of ¼''-20 set screw (½'' long)

 iii) Target Specimen

- FIX-0076 45 degrees Angled Target fixture
- Mold (water-tight, made of polycarbonate plates, 5.5in x 5.5in x 5.5in cube-shaped container)
- ¼-20 bolt (6 in long)
- Silicone glue gun or tape (plastic, masking, etc.)

iv) Lighting devices

- 2x Halogen lamp (key light, 250 watts, 4,000 lumens)

- 1x LED light (fill light, 4,000 lumens)

- 1x LED stand light (back light)

v) Video recording device

- Phantom Ultrahigh-speed Camera v5.2 (capable of 2200 fps, 45 us exposure time specification)

vi) Impact force data acquisition system

- Piezoelectric impact force sensor: PCB 200C20 SN 7069

  o Measurement range: 20000 lb (compression)

  o Upper Frequency Limit: 40000 Hz

- Signal conditioner: PCB 483C05

- NI DAQ USB X series

- Phantom Camera Control (PCC) software

- Coaxial cable (BNC plug to BNC plug)

- Coaxial cable (10-32 plug to BNC plug)

- USB cable (type A-male to type B-male)

< Coaxial cable, BNC plug (left) and BNC plug (right)>

< Coaxial cable, 10-32 plug (left) and BNC plug (right)>

vii) Miscellaneous equipment

- Weight scale

  - Recommended equipment:

    ○ Cole-Parmer Bench Scale

    ○ 3kg capacity and 0.1g readability

- Forensic scale (recommended)

< Forensic scale>

- Ruler (required, inch or metric)

- 4ea of 80/20 inc L-shaped bracket

- 4ea of ¼-20 bolts (¼''~ ⅜'' long)

139

1.3.   Target Specimen Prep

1.3.1.   <u>Target Specimen Prep</u>

i)   Fabricate ballistic gelatin target block one day prior to the date of testing

- Required equipment:

    o   5.5in x 5.5in x 5.5in mold,

    o   'FIX-0076 45 degrees Angled Target fixture'

    o   Bone target sample

- Recommended material amounts:

    o   1000 mL tap water in double boiler

    o   2500 mL tap water in beaker

    o   500 g ballistics gelatin powder

- Prepare 'FIX-0076 45 degrees Angled Target fixture' and a bone target sample

- Connect target sample with the 'FIX-0076 45 degrees Angled Target fixture' using ¼-20 bolt (6 in long)

< Example of connected bone target and target fixture (FIX-0076)>

- Fix the target and target fixture on the bottom surface of the mold using a silicone glue gun (recommended) or tape (plastic, masking, etc.)
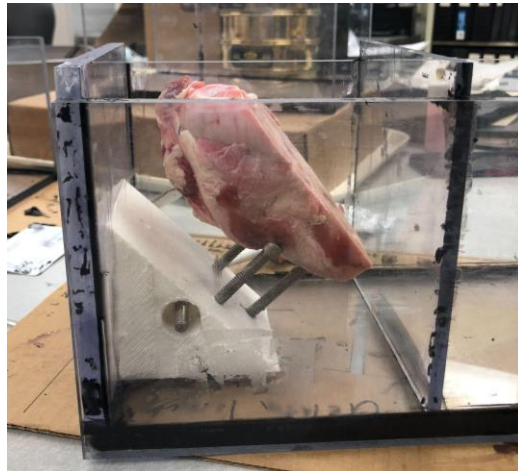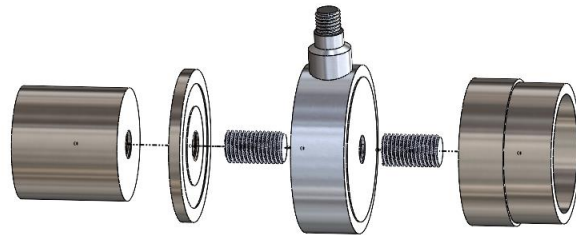

< Fixed target and target fixture in the mold (silicone glue used)>

- Molds should need about 4 hours in the refrigerator before specimens are fully cured.

- Record action on Target Sample Handling Record.

1.4.　　　Projectile Specimen Prep

i)　　Assemble 'FIX-0075 Projectile Tip Mount of Air Cannon' using 2ea of ¼''-20 set screw (½'' long)

< Exploded view of 'FIX-0075 Projectile Tip Mount of Air Cannon'>

ii)　　Install desired projectile specimen by fastening target into the front of 'FIX-0075 Projectile Tip Mount of Air Cannon.'

< Example of 'FIX-0075 Projectile Tip Mount of Air Cannon' assembly>

1.5.   Equipment Set-up

   1.5.1.   Safety Check-up Before Testing

   i)   Ensure that you disarm the air cannon by opening the valve located at the back

        of the air chamber at all time except when actively firing the cannon.

        ● (WARNING) High-pressured air release from the air cannon might

           propel surrounding debris and/or items, and could injur and damage

           people and facilities nearby the test apparatus

< Depressurizing air chamber turning knob (red)>

1.6.   <u>Sensor & Signal Conditioner Prep (optional)</u>

i)   Assemble piezoelectric force sensor system devices as it is seen in Figure 07.

ii)   Connect the signal conditioner with NI DAQ USB-X using a coaxial BNC-to-BNC cable

<BNC coaxial cable plug connected to Analog Input 0 of NI DAQ>
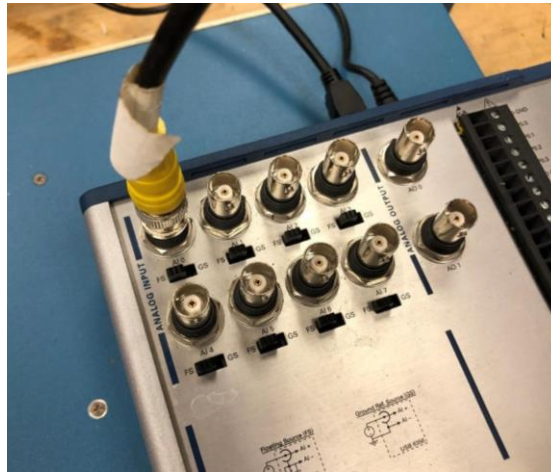
iii)   Run data acquisition software (NI LabView) in Host Computer (PC, laptop, etc.)

- Refer to the following official tutorial videos provided from National Instruments
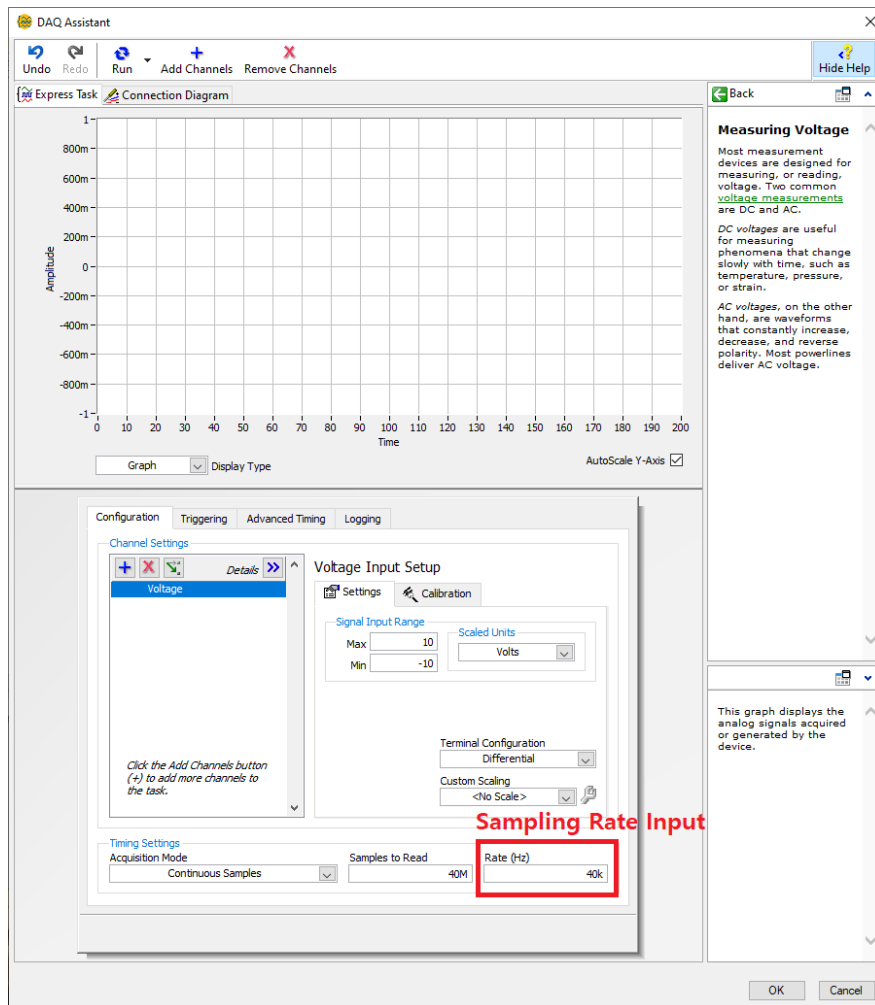 - o 'Acquire and Generate Digital I/O with NI USB X Series' (https://youtu.be/oJ6obDD-InA?t=62)

144

- o 'Data Acquisition with NI myDAQ: DAQ Assistant'

  (https://youtu.be/72157fx31vw)

- Input Sampling rate (40,000 Hz) in DAQ Assist function in Labview VI

<NI DAQ Assistant front panel, Sampling rate setting>

1.7.   <u>Set-up Lighting Devices</u>

i) Set-up lighting devices referring to the following figure and instructions.

<Lighting devices positioning>
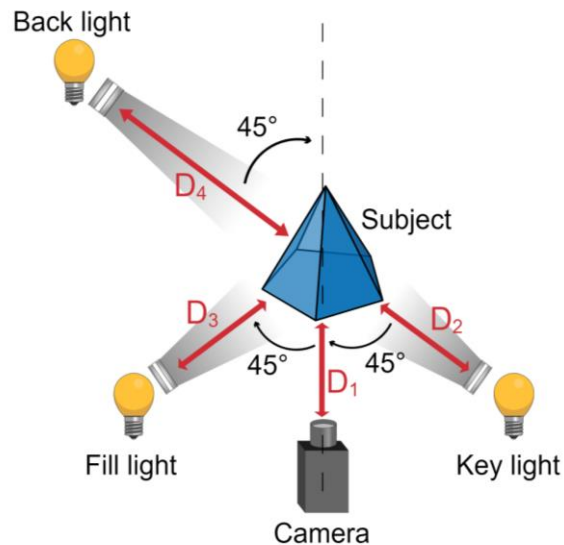
- Halogen lamp (key light) comes at 45 degrees in front of and 3ft ($=D_2$) away from the Safety Chamber (FIX-0074)

- LED light (fill light, 5000 lumens) comes on the opposite side of the halogen lamp in front of and 1ft ($=D_3$) away from the Safety Chamber (FIX-0074)

- LED stand light (backlight) comes 1ft ($=D_4$) away from the top of the

  Safety Chamber (FIX-0074)

<Halogen lamp (right bottom, black), and led lights>

ii) Turn on the lighting devices

1.8.   <u>Set-up Video Recording Devices</u>

i)   Set-up Video recording device

- Position Phantom Camera approximately 7ft away from the Safety

  Chamber (FIX-0074), in line with key light and fill light.

<Example of camera set-up>

ii) Desired subjects to be captured by camera include:

a) Projectile (Bone spear, projectile mount, impact sensor)

b) Projectile trajectory (from the initial position to the back surface of the

target fixture)

c) Target (Ballistic gel block, target, target fixture)

d) Labels with sample number and date of the testing

e) Scales

<Example of camera image capturing set-up>
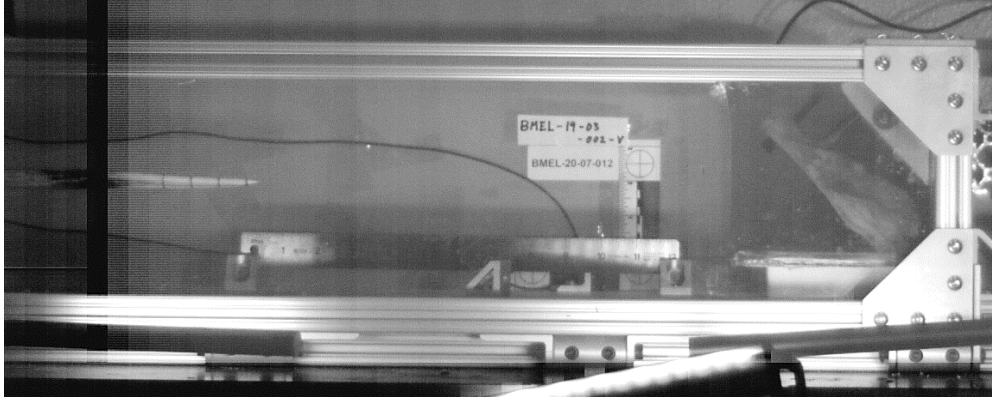
iii) Camera Setting Parameters

- Based on camera setting practices, the optimal parameters for sample rate,

  exposure time, and video resolution are as follows.

  a) Sample rate: 2200 fps

  b) Exposure time: 45 usec

  c) Video resolution: 1152 x 720

```
Format                RGB Cine
Saved Range           [-730, -328]
Recorded Range        [-1154, 1357]
Color                 No
Shutter Mode          Global
Signals               Not Recorded
Audio                 Not Recorded
Image Time            Available
Image Exposure        Available
Camera Version        52 (Phantom v5.2)
Serial                8085
Resolution            1152 x 720
Acq Resolution        1152 x 720
Post Trigger          1358
Bits per pixel        12
Acquisition bpc       12
Sample Rate(fps)      2200 fps
                      Real: 2200.220022 fps
                      Period: 454.50 µs
Exposure (µs)         45.000
EDR (µs)              0.000
Frame Delay (µs)      0.000
Sync                  Internal
AutoExposure          Off
Lens Description      -
Lens Aperture         -
Lens Focal Length     -
Trigger Time          Tue Dec 15 2020
                      14:11:17.506 725 X X
Time Zone             -06.00
No Frame Rate Profile
```

<Camera Setting Parameters>

1.9. Testing System & Fixture Prep

i) Connect the Solenoid valve push-button switch with the air cannon using 24

volts power supply

150

<Connected Push button switch (red) with solenoid valve of Air cannon (FIX-0073)>

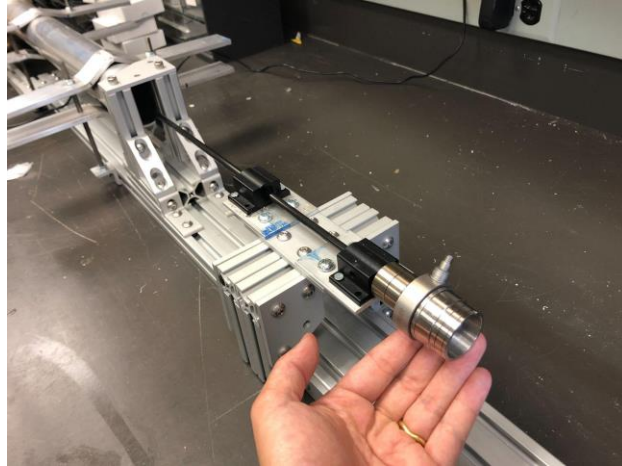ii) Insert the carbon rod of 'Projectile (FIX-0075)' into the air cannon barrel front outlet

<Inserted carbon rod into the air cannon barrel front outlet>

iii) Assemble Piezoelectric impact force sensor and 'FIX-0075 Projectile Tip

Mount of Air Cannon', and mount the assembly to the carbon rod

<Projectile Assembly Installed to the Air Cannon>

1.10.   Specimen Set-up

1.10.1.   Test Labels & Scale Installation

i)   Remove pre-installed test labels if necessary

ii)   Attach desired test labels including the following information onto the inner

back surface of the 'FIX-0074 Safety Cabinet of Air Cannon' using tape

(plastic, masking, etc.) or glue.

- Target sample accession number

- Projectile point sample accession number

- Date of testing

Target sample accession #	BMEL-YY-MM-###
Projectile point sample accession #	BMEL-YY-MM-###
Date of testing	MM-DD-YY

<Recommended test labels and the area for attaching labels>

iii) Attach a forensic scale next to the labels

iv) Put a ruler in the middle of the 'FIX-0074 Safety Cabinet of Air Cannon' platform top surface and fix the ruler firmly using four 80/20 brackets and ¼-20 bolts

<Example of Forensic Scale & Ruler Installation>
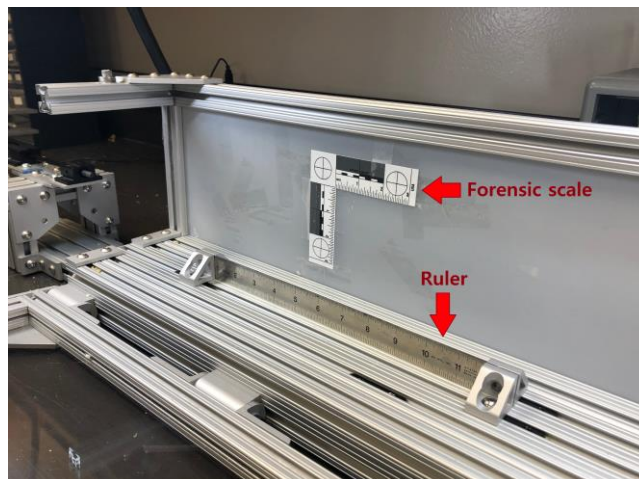
1.10.2.   Projectile Weight Measurement

   i)   Assemble Piezoelectric impact force sensor, 'FIX-0075 Projectile Tip Mount of Air Cannon', and desired projectile specimen using 2ea ¼''-20 set screw (½'' long)

   ii) Prepare weight scale

   iii) Measure the assembly with the weight scale

<Example of Measuring Projectile Mount Assembly Weight'>

1.10.3.   Ballistic Target Specimen Set-up

   i)   Release two bolts at the front top of 'Safety Cabinet of Air Cannon (FIX-0074)' to open the front door

   ii) Position the ballistic gelatin block on the cabinet platform

iii) Ensure to push gelatin block firmly towards back support of the Safety
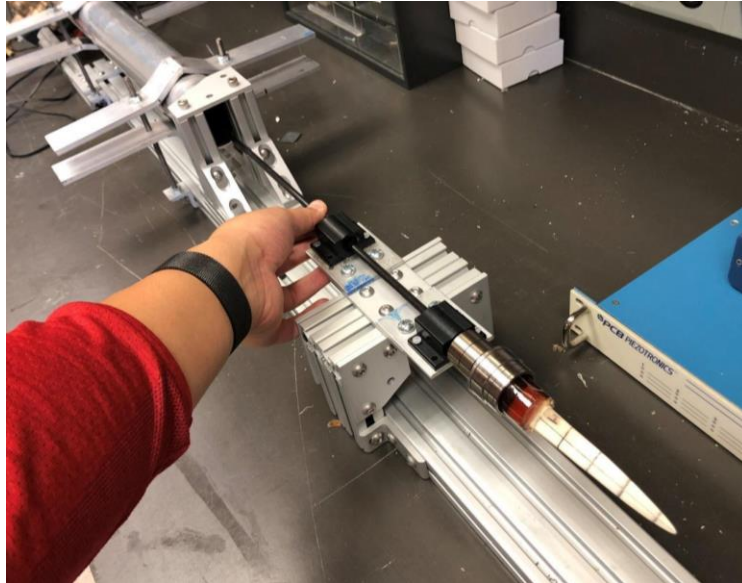
Cabinet (FIX-0074)

<Positioning target sample in the 'Safety Cabinet (FIX-0074)'>

iv) Close the safety cabinet front door

v) Ensure to lock the front door by fastening the bolts on the cabinet top

1.10.4.　　Projectile Specimen Set-up

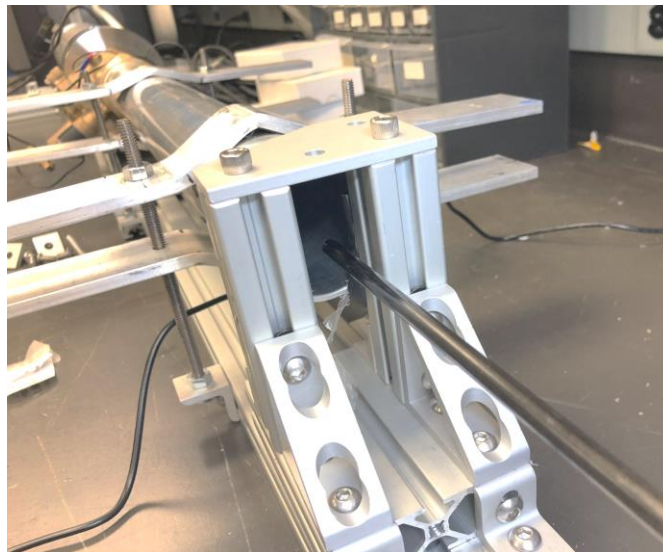i) Mount the projectile specimen at the front of 'FIX-0075 Projectile Tip Mount

of Air Cannon' (refer to section 4.5.iii)

<Connected projectile mount and projectile tip to the carbon rod>
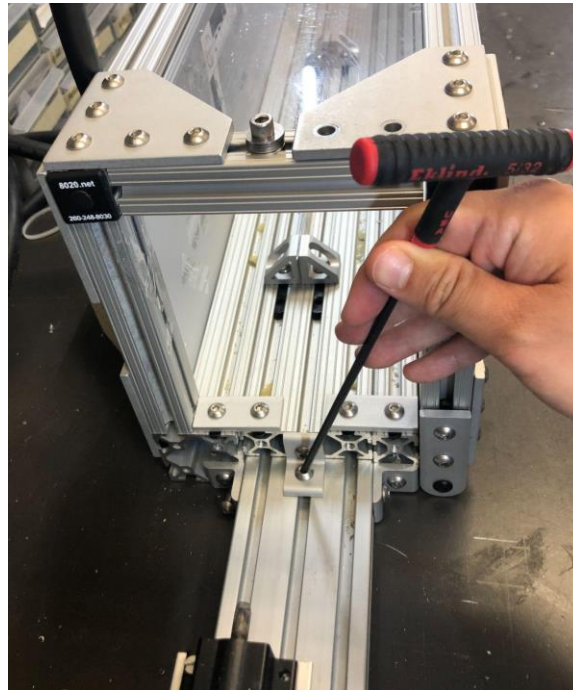
1.10.5.   Projectile Gliding Distance Set-up

i)   Pull the carbon rod out of the 'FIX-0073 Air Cannon' barrel until the end tip

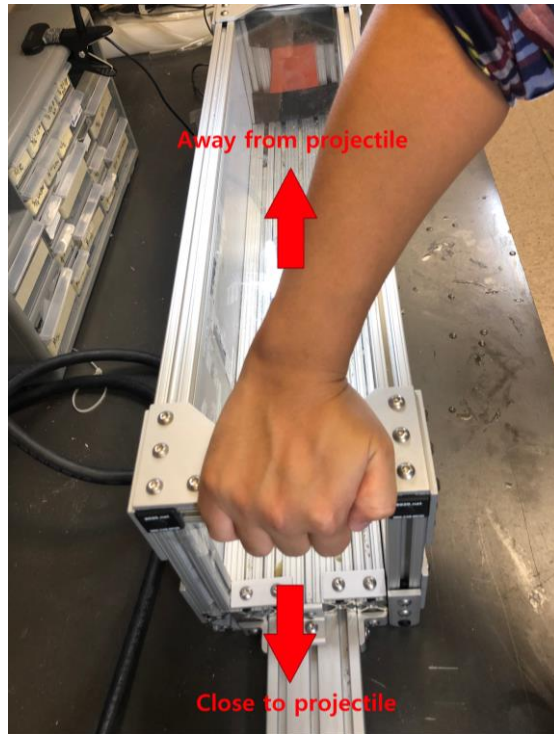of the rod is placed on the same line of the front outlet of the cannon barrel.

<Carbon rod fully ejected from the air cannon barrel>

156

ii) Adjust gliding distance of the projectile

● Release L-shaped bracket at the side of the platform

<Releasing L-shaped bracket connecting safety cabinet with air cannon>

● Adjust the distance to be less than 1cm between the tip of the projectile

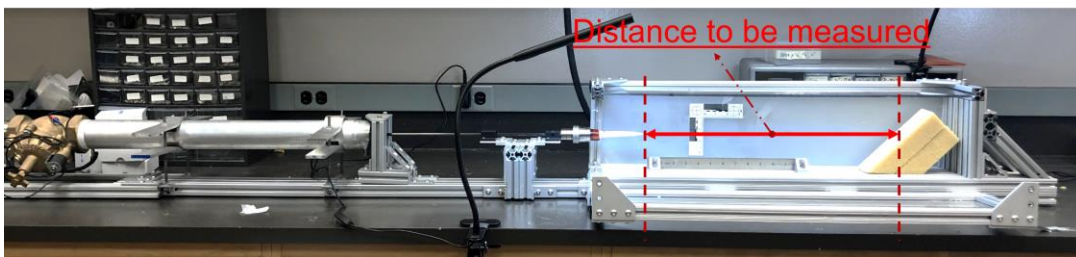point and the nearest surface of the target from the projectile point tip.

<Adjustment direction of projectile gliding distance>

● Fasten L-shaped bracket to connect the 'FIX-0073 Air Cannon' and the
'FIX-0074 Safety Cabinet' firmly

<Example of adjusting projectile gliding distance>

iii) Push the projectile back all the way into the 'FIX-0073 Air Cannon' barrel

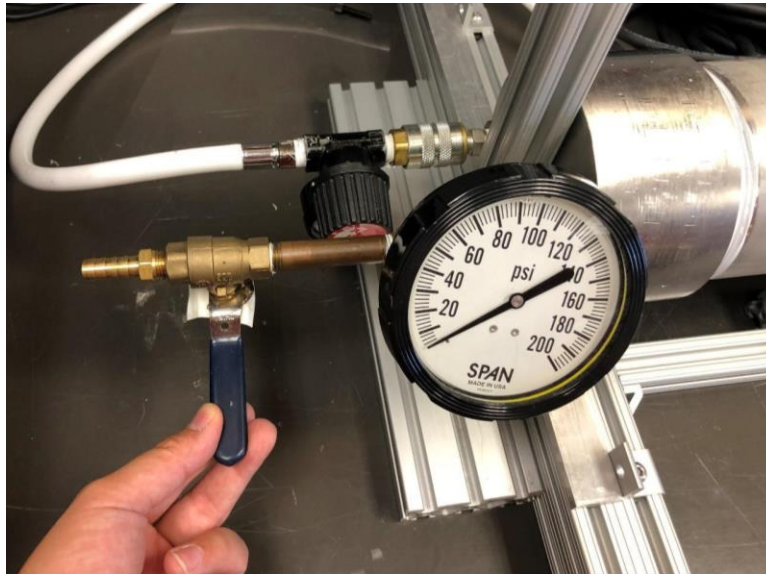iv) Measure the distance between the projectile tip and the nearest surface of the target in units of 'CM'.

<Example of distance to be measured>

1.11.   Testing Execution

1.11.1.   Test Apparatus Initialization

i)   Close air release valve located at the back of the air cannon

<Closed position of air release valve, tightening by is hand sufficient>

ii)   Charge air chamber to 30psi by turning the air charging knob gently until the

pressure gauge reaches the desired air pressure

160

<Air chamber charged with 30 psi air by turning air pressurizing knob (red)>

  iii) Initialize video capturing software in the Host computer (PC, laptop, etc.) and begin recording video.

  iv) Initialize data acquisition software (Phantom Camera Control) in Host Computer (PC, laptop, etc.) and commence sensory data record

  v) Push solenoid valve on switch button to release pressurized air to propel the installed projectile

1.11.2. <u>Data Acquisition</u>

NOTE: All file names should be in compliance with SOP-0008.

 i) Video Records

  - Data Type: Ultrahigh-speed camera video footage

- Format: Phantom Cine-File (.cine)

- Ensure to save the recorded video footage from Phantom Camera Control (PCC)

ii) Impact sensor readings

- Data Type: Voltage readings from the impact sensor

- Format: TMDS file (.tdms)

- Ensure to save the recorded sensory data from LabView VI

iii) Photograph of Test Results

- Open the Safety Chamber (FIX-0074) front door

- Photograph target and projectile in the chamber with scales in a frame

<Example of test result photography>
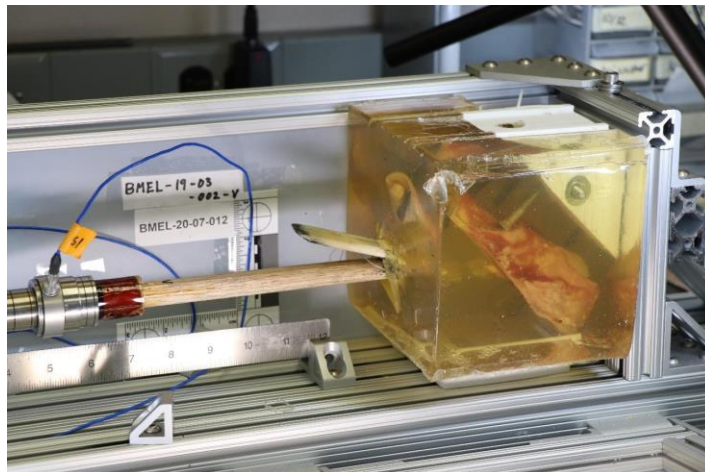
iv) Tested Samples

- Put on gloves

- Remove the bone spear projectile from ballistic gelatin block target and
  dry it with Kim wipes

<Removing spear-like bone projectile tip from the target using hand>

- Collect all fragments and debris of the projectile following fracture
  failure

- Collect ballistic gelatin block and remove gelatin from bone with hands.

- Place restored projectile, fragments, and bone target on black or white-
  colored paper, mat, or fabrics as a background for photography

- Be sure to position the BMEL accession number label and proper scale in the camera frame

- Photograph the projectile, fragments, and sample label

<Example of test result photography>

1.12.   Sample Storage and Test Reset

1.12.1.   Spear tip projectile:

- Keep the bone spear projectile and fragments in a plastic bag

- Ensure to write the following information on the bag

  o BMEL sample accession number

  o Date of storage (MM-DD-YYYY)

  o Initial of personnel who produce the bag

- Store the bag in the sample cabinet (closed, dark container at room

  temperature) at the JCAIN lab

164

1.12.2.   <u>Bone target:</u>

- Cover the bone target sample with a wet paper towel

- Keep the sample in a plastic bag

- Ensure to write the following information on the bag

   o BMEL sample accession number

   o Date of storage (MM-DD-YYYY)

   o Initial of personnel who produce the bag

- Store the plastic bag in the freezer

1.12.3.   <u>Reset Testing Apparatus</u>

i)   Clean up debris in the safety cabinet and its surroundings

ii) With the next target and projectile samples, repeat **sections 4.10 through 4.12.2.** until study completion.

<Initial position of projectile assembly>
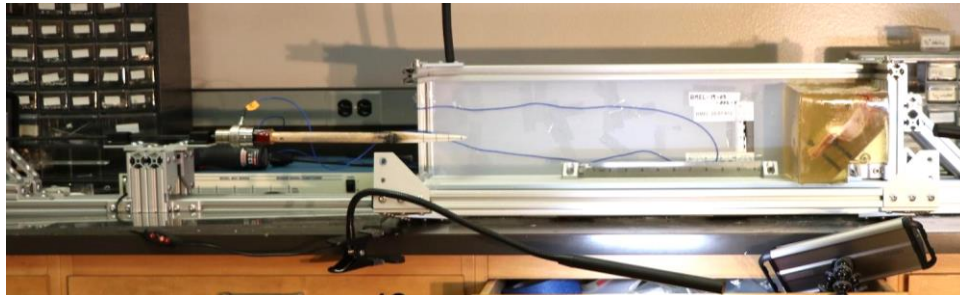
1.13.   Data upload

 1.13.1.   Upload the data, video, and pictures in the 'Google Drive – BMEL Quality – Quality System Inbox'

 1.13.2.   Scan and upload testing records.

 1.13.3.   Create entries in the sample history files to reflect that each sample has undergone testing according to this document.

1.14.   Clean up

 1.14.1.   Testing equipment

  i)   Wipe off the liquid from the testing equipment surface

  ii)   Sanitize testing surfaces with sanitizer (Wipes, 70% ethanol, Clorox, et al.)

2.   Test Results To Be Acquired

2.1.   <u>List of Required Measurements</u>

 i)   Dependent variables to be measured:

- Projectile instantaneous velocity (before impact)

- Instantaneous linear momentum

- Fracture type

- Shape of major fragments

- Number of major fragments

- Depth of penetration
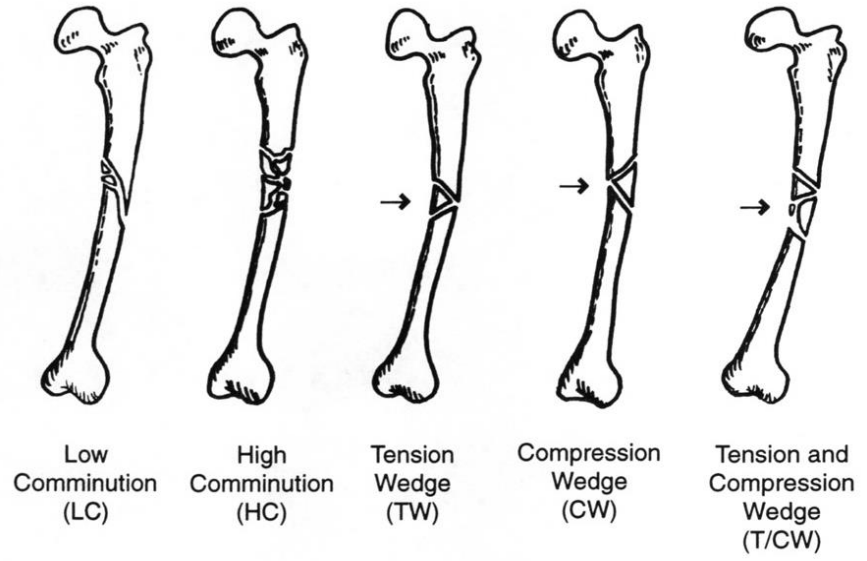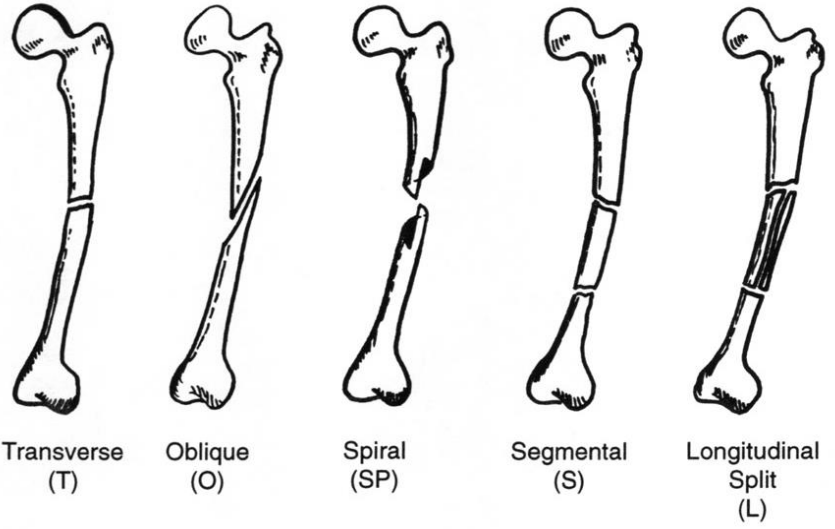
- Damage shape of target

 ii)   Possible extraneous and confounding variables:

- Geometric variation in shape among individual osseous point projectiles

- Mechanical properties variation in target bone (cancellous bone density, thickness of cortical bone layer)

iii) Data to be collected

  i. Recorded projectile trajectory video

    a. Data type:

      - Ultrahigh-speed camera video footage

    b. Purpose:

      - The objective of acquiring ultrahigh-speed video footage is to measure the **projectile's velocity** between two consequent images and calculate **linear momentum**. In particular, by analyzing linear momentum data, we are able to obtain data of energies propelling projectile and impact forces delivered to a target. The energy and forces will be correlated to fracture patterns (e.g., length and angle of fracture).

    c. Method Description:

      - Projectile impact tests will be performed with a sampling rate of 2200 fps (0.45 msec/ frame). By measuring the travel distance of the projectile between an image and the succeeding image, we are able to calculate the average velocity between the images. To measure the travel distance, a particular software, or ImageJ, that is capable of measuring length based on a unit pixel within an image will be used.

167

ii. Osseous point projectile and fragments (if a fracture has occurred)

    a. Data type:

- Fractured projectile shaft body and fragments

- Photography of fractured projectile shaft body and fragments

    b. Purpose:

- The objective of acquiring fractured projectile and fragments and their photography are to analyze '**Fracture type**', '**Shape of major fragments**', and '**Number of major fragments**'

    c. Method Description:

- After each impact test, each point and fragment will be removed from the ballistic gelatin, kept and sealed in a plastic bag, and stored in a freezer

- After each impact test, the type of fracture will be analyzed and recorded along with the length and size of the point's broken body and the fragments

- We will use the following categories of damage to evaluate the fracture type:

  - Tip crushing (LC; Low Comminution)

  - Microscopic (HC; High Comminution)

  - Transverse/snap (T)

- Oblique (O)

- Spiral (SP)

- Segmental (S)

- Longitudinal Split (L)

- **Tension Wedge (TW) -** *Butterfly fracture*

- Compression Wedge (CW)

- Tension and Compression Wedge (T/CW)

Transverse
(T)

Oblique
(O)

Spiral
(SP)

Segmental
(S)

Longitudinal
Split
(L)

Low
Comminution
(LC)

High
Comminution
(HC)

Tension
Wedge
(TW)

Compression
Wedge
(CW)

Tension and
Compression
Wedge
(T/CW)

<Fracture Patterns>

<Loading Mode and Fracture Type>
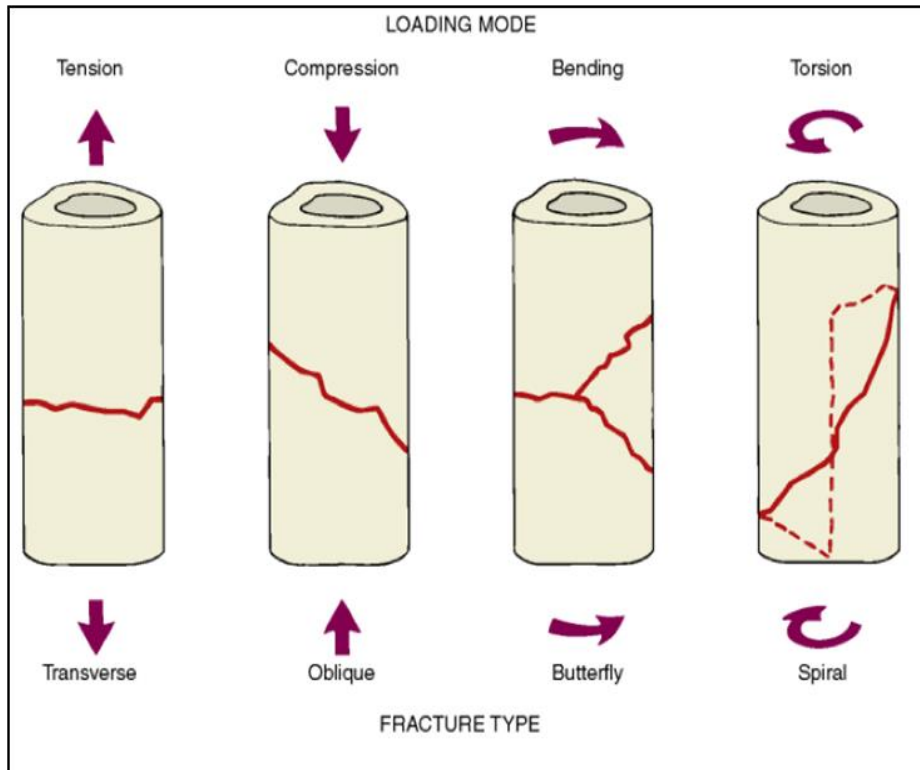
iii. Bony target

 a. Data type:

  ● Penetrated and damaged bone target

  ● Photography of the damaged target

 b. Purpose:

  ● The objective of acquiring the damaged target and their

  photography is to compare the '**Depth of penetration**' and the

'**Shape of target damages'** to the configuration of Manis Mastodon

model

c. Method Description:

- After each impact test, each target and debris will be removed from the ballistic gelatin, kept and sealed in a plastic bag, and stored in a freezer

3. Limitations

i) Despite controlling experimental variables (e.g., launching system set-up parameters), there is a possibility of changes in variables such as projectile tip shape, projectile thickness, edge angle, point angle, spinning of the projectile while propelled by air cannon, etc. For this reason, the factors may influence the type and size of the fracture (length, shape of fracture lines). In this study, we will present three tests carried out in the most controlled fashion. In particular, we will control the projectile's tip and shaft shape, raw material, and weight while measuring projectile velocity, linear momentum, and impact forces.